

**UNIVERSIDADE DE SOROCABA
PÓS-GRADUAÇÃO, PESQUISA, EXTENSÃO E INOVAÇÃO
PROGRAMA DE PROCESSOS TECNOLÓGICOS E AMBIENTAIS**

Raphael Basilio Pires Nonato

**DESIGN, POWDER METALLURGY, SINTERING, AND SOFTWARES FOR
EXTREMELY HARD MULTICOMPONENT METAL ALLOYS**

**Sorocaba/SP
2023**

Raphael Basilio Pires Nonato

**DESIGN, POWDER METALLURGY, SINTERING, AND SOFTWARES FOR
EXTREMELY HARD MULTICOMPONENT METAL ALLOYS**

Thesis presented to the Examination Board of Post-Graduation Program in Technological and Environmental Processes of University of Sorocaba (Universidade de Sorocaba, UNISO) as partial fulfillment to the obtainment of Doctor's title in Technological and Environmental Processes.

Advisor: Prof. PhD. Thomaz Augusto Guisard Restivo.

**Sorocaba/SP
2023**

Ficha Catalográfica

Nonato, Raphael Basilio Pires
N737d Design, powder metallurgy, sintering, and softwares for
extremely hard multicomponent metal alloys / Raphael Basilio Pires
Nonato. – 2023.
165 f. : il.

Orientador: Prof. Dr. Thomaz Augusto Guisard Restivo
Tese (Doutorado em Processos Tecnológicos e Ambientais) –
Universidade de Sorocaba, Sorocaba, SP, 2023.

1. Ligas (Metalurgia). 2. Metalurgia do pó. 3. Sinterização. 4.
Programas de computador. I. Restivo, Thomaz Augusto Guisard,
orient. II. Universidade de Sorocaba. III. Título.


Raphael Basilio Pires Nonato

**DESIGN, POWDER METALLURGY, SINTERING, AND SOFTWARES FOR
EXTREMELY HARD MULTICOMPONENT METAL ALLOYS**


Thesis approved as partial fulfillment to the
obtainment of Doctor's degree in the Post-
Graduation Program in Technological and
Environmental Processes of University of
Sorocaba (Universidade de Sorocaba,
UNISO)

Approved in: May 19th, 2023

EXAMINATION BOARD:

Documento assinado digitalmente
 **THOMAZ AUGUSTO GUIARD RESTIVO**
Data: 23/05/2023 09:26:45-0300
Verifique em <https://validar.iti.gov.br>


Prof. PhD. Thomaz Augusto Guisard Restivo
Universidade de Sorocaba

Documento assinado digitalmente
 **DIEGO APARECIDO CARVALHO ALBUQUERQUE**
Data: 23/05/2023 16:50:45-0300
Verifique em <https://validar.iti.gov.br>


Prof. PhD. Diego Aparecido Carvalho Albuquerque
Universidade de Sorocaba, FACENS, FATEC



Prof. PhD. Michel Chaves
Universidade de Sorocaba

Documento assinado digitalmente
 **ROSSANA CRISTINA ROSSONI FIGUEIRA**
Data: 24/05/2023 19:51:00-0300
Verifique em <https://validar.iti.gov.br>

Prof. PhD. Rossana Cristina Rossoni Figueira
Universidade de Sorocaba

Documento assinado digitalmente
 **DANIEL LEAL BAYERLEIN**
Data: 25/05/2023 11:52:48-0300
Verifique em <https://validar.iti.gov.br>

Prof. PhD. Daniel Leal Bayerlein
Combustol Metalpó Pesquisa, Desenvolvimento e Inovação

I dedicate it to God, without Whom all this
would not be possible.

DEDICATION

First, I dedicate this work to God, Who, in my humble opinion, is the only explanation for all this to be done. I thank Him for everything. Absolutely everything.

I also dedicate it to my grandfather (*in memoriam*) for having taught me everything that was on the menu of life and for having provided me the conditions to be here today, climbing one more step on the long ladder of knowledge. My grandmother (also *in memoriam*), his wife, complemented his contribution by giving me the first education, the one that comes before the provided in the formal school. I simply thank them for having had the pleasure of being with them.

I dedicate this work to my godmother and aunt, who believed in me when most no longer believed and gave me the possibility of reaching a horizon never imagined before. I thank her for all the situations and circumstances that brought unlimited learning to me.

I dedicate it to my godfather and uncle, who, even with very little time, helped me precisely when I needed the most, whether through wise advice derived from his enormous emotional intelligence or by a simple handshake in suitable moments. I extend my thanks to the godmother of my daughter, with whom I learned to have more attitude in life.

I offer this work to my parents, who, despite all the adversities that life presented to them, still knew how to lead their children along a good path, making them able to become citizens and good people. That has always been, is and will be something of great value to society.

I affectionately dedicate this work to my grandmother (*in memoriam*), who, in addition to regretting our few conversations, taught me the intensity of pure and full feeling. I make an honorable mention of my friend Miguel who, in a certain way and within his possibilities, helped me to conquer the woman I dreamed of so much through his unrestricted acceptance of my person.

And what about my wife and eternal girlfriend? Words are certainly lacking to describe how representative she is in my life. Our paths have crossed each other and will forever walk together. Thank you so much for being my teacher of feelings, because, above all, you taught me the task that most demands from students who dare to learn it: to love unconditionally. I thank you for being my companion at all times and for putting up with me, especially in the entire doctoral path. I love you.

This thesis would not make sense if our two children were not here to bring more light to our lives. Since their birth, our journey has been more meaningful and softer. I then learned one of the most valuable types of love. To my son and my daughter: sorry for the time absent from your lives. I also love you.

This work could not be complete without dedicating it to my sister (*in memoriam*), to my grandmother (*in memoriam*), and to my brother (*in memoriam*). The first, despite having left us very early, offered us her simple and sweet soul. My grandmother lived with me when I was still a “small child” and taught me the power of love, dedication and perseverance.

I also would like to thank my brother who taught me how to enjoy our passage more throughout this world. Thank you for that. Our experiences together will always be on my mind. What’s up, brother?

I dedicate this thesis to Professor PhD. Thomaz Augusto Guisard Restivo, who, besides being my advisor, is now a friend of mine. Thank you for the valuable lessons learned, partnership, and friendship.

It is also dedicated to my friends Jean (*in memoriam*) and Luiz, with whom I started my path at CEFET/RJ. Our friendship will last forever wherever we are. Thanks for all the moments together.

To all those who participated directly and indirectly in my hitherto brief existence, thank you very much. I thank you for contributing effectively to building my character. Thank you so much for being the rocks on which I could build my boyhood dreams.

ACKNOWLEDGEMENTS

I would like to thank the University of Sorocaba (Universidade de Sorocaba, UNISO) for providing the Doctoral course in Technological and Environmental Processes. This opportunity really changed my life.

I would like to say a big thank you to my advisor and now friend, Professor PhD. Thomaz Augusto Guisard Restivo, who knew all the time to tell me which way to go so that we could reach the objective set from the beginning. In the advisory, there were many face-to-face conversations and experiments performed, which were complemented by phone calls, e-mails, and messages, moments in which I was able to learn valuable lessons. In addition, he and Professor PhD. Norberto Aranha were my teachers of the subject “Material Processing and Development”, whose content was taught with the mastery peculiar to them.

I also thank the coordinator of the program, Professor PhD. Daniel Bertoli Gonçalves, who, besides conducting the program with so much dedication, is an excellent professor. He was my teacher in the subject of “Projects in Research and Development”. I also thank to the program secretary, which, led by Ms. Cláudia Neres de Meira Andrade, and Daniela Rosa de Oliveira, made my academic life easier and more pleasant. These people provided an extraordinary service with great sympathy, such as I had never seen anywhere else. Thanks for the questions answered and problems solved.

I must congratulate Professors PhDs. Angela Jozala and Denise Grotto. They taught me the subject “Integrated Practices in Technological and Environmental Processes”, in which I was able to not only learn about this subject, but also develop part of my thesis. In addition, worthy of thanks is Professor PhD. José Martins de Oliveira Junior, who taught me the subject “Non Destructive Testing”.

I would like to thank the examination board (Prof. PhD. Thomaz Augusto Guisard Restivo, Prof. PhD. Diego Aparecido Carvalho Albuquerque, Prof. PhD. Michel Chaves, Prof. PhD. Rossana Cristina Rossoni Figueira, and Prof. PhD. Daniel Leal Bayerlein.

The author acknowledges the research councils CNPq (proj. 408406/2021-6), Catalisa ICT Sebrae (proj. 29083*128), and FAPESP (proj. 2020/09736-3) for the financial support. Finally, I would like to thank all those who participated directly and/or indirectly in this project.

“The key to the engine of success begins to turn when one assumes full responsibility for all events that occur”.

Raphael Basilio

ABSTRACT

Extremely hard multi-component metal alloys (EHMMAs) are required mainly when wear resistance is the most important requirement in a product. In view of this, researchers established some technical parameters to predict the stability of the resulting EHMMMA and facilitate the design process of this alloy. Among the existing parameters, twenty-two were selected in this research to theoretically intend to ensure that EHMMMA forms a stable solid solution. Associated with some of these parameters, there are five criteria from which the stability of the alloy is evaluated. Aiming to predict, streamline and facilitate the EHMMMA design process, concomitantly with the calculation of the parameters involved and the availability of the status of the associated criteria, three softwares (PComp, DIAMOY 2.0, and SINT) were coded in Microsoft Visual Basic 6.0[®] and transformed into Windows[®] applications. The first one developed, the PComp, provides the minimum load necessary to compact the alloy powder, outlining, streamlining and trying to guarantee less porosity in the compacted for later sintering. The second software, DIAMOY 2.0, addresses the mass of each chemical element to compose the required EHMMMA mass, in addition to calculating the values of twenty parameters and five associated criteria, and whether each established criterion is met. Depending on the results, this software can avoid laboratory experiments with alloys that would not present the possibility of constituting stable solid solutions associated to high hardnesses. The scheme of the experimental part of this thesis is translated into a flowchart of the process, in which nine different alloys are studied in terms of their obtainment, hardness, chemical composition, densification, and microstructure. As part of the results, the alloys are subjected to scanning electron microscopy (SEM), backscattered electron (BSE), and differential scanning calorimetry (DSC). Hardnesses up to 1054.96 Vickers were obtained. The maximum densification reached 98.54% of the theoretical. The results from DIAMOY 2.0 were validated by comparing two EHMMAs with a maximum relative error of 1.923% for one EHMMMA and 3.183% for the other EHMMMA. The third software, SINT, was developed to evaluate the densification of metal alloys and was applied to L4 alloy. Therefore, the main contributions of this research to the design of EHMMAs refer to: (a) gathering of parameters and criteria not yet used for the design of EHMMAs in a single computational tool, facilitating the evaluation of the design process; (b)

establishing an EHMMA design framework; (c) creation of computational tools for powder compaction, EHMMA design and sintering for Windows® platform; (d) creation of metallic alloys not yet reported; (e) carrying out experiments with some alloys that have a predicted potential to form stable solid solutions with high hardness; (f) establishing a baseline for future improvements.

Keywords: metal alloy design; metal alloy design; metal alloy; extremely hard multicomponent metal alloys (EHMMA); metal powder compaction; powder metallurgy; sintering; alloy design; software.

RESUMO

Ligas metálicas multicomponentes extremamente duras (do inglês, *extremely hard multi-component metal alloys*, EHMMAs) são exigidas principalmente quando a resistência ao desgaste é o requisito mais importante em um produto. Diante disso, pesquisadores estabeleceram alguns parâmetros técnicos para prever a estabilidade da EHMMa resultante e facilitar o processo de projeto da referida liga. Dos parâmetros existentes, vinte e dois foram selecionados nesta pesquisa para teoricamente pretender assegurar que a EHMMa forme uma solução sólida estável. Associados a alguns desses parâmetros, existem cinco critérios a partir dos quais a estabilidade da liga é avaliada. Visando prever, agilizar e facilitar o processo de projeto da EHMMa concomitantemente ao cálculo dos parâmetros envolvidos e disponibilização do status dos critérios associados, três programas de computador (PComp, DIAMOY 2.0, and SINT) foram codificados em Microsoft Visual Basic 6.0® e transformados em aplicativos de Windows®. O primeiro desenvolvido, o PComp, fornece a carga mínima necessária para compactar o pó de liga, delineando, agilizando e tentando garantir menor porosidade do compactado para posterior sinterização. O segundo *software*, DIAMOY 2.0, emite a massa de cada elemento químico para compor a massa da EHMMa necessária, além de calcular os valores de vinte parâmetros e cinco critérios associados, e se cada critério estabelecido é atendido. A depender dos resultados, este programa de computador pode evitar experimentos laboratoriais com ligas que não apresentariam possibilidade de constituírem soluções sólidas estáveis associadas à elevada dureza. O esquema da parte experimental desta tese traduz-se num fluxograma do processo, no qual são estudadas nove ligas diferentes em termos de sua obtenção, dureza, composição química, densificação e microestrutura. Como parte dos resultados, as ligas são submetidas a microscopia eletrônica de varredura (SEM), elétron retroespalhado (BSE) e calorimetria de varredura diferencial (DSC). Obteve-se durezas de até 1054,96 Vickers. A densificação máxima atingiu 98,54% da teórica. Os resultados provenientes do programa DIAMOY 2.0 foram validados pela comparação com duas EHMMAs, apresentando erro relativo máximo de 1,923% para uma EHMMa e 3,183% para a outra EHMMa. O terceiro *software*, SINT, foi desenvolvido para avaliar a densificação de ligas metálicas e foi aplicado à liga L4. Portanto, as principais contribuições desta pesquisa para o projeto de EHMMAs

referem-se: (a) união de parâmetros e critérios ainda não utilizados para o projeto de EHMMAs numa única ferramenta computacional, facilitando a avaliação do processo de projeto; (b) estabelecimento de uma estrutura de projeto de EHMMAs; (c) criação de ferramentas computacionais para compactação de pó, projeto de EHMMAs e sinterização para a plataforma Windows®; (d) criação de ligas metálicas ainda não reportadas; (e) realização de experimentos com algumas ligas que apresentam uma predição de potencial para formar soluções sólidas estáveis com elevadas durezas; (f) estabelecimento de uma linha de base para melhorias futuras.

Palavras-chave: projeto de liga metálica; ligas metálicas; ligas metálicas multicomponentes extremamente duras; compactação de pó metálico; metalurgia do pó; sinterização; projeto de liga; programa de computador.

LIST OF ILLUSTRATIONS

Figure 1 - Number of publications with “hard metal” in the title or subject.	26
Figure 2 - Number of publications with “powder metallurgy” in the title or subject.	26
Figure 3 - Number of publications with “sintering” in the title or subject.	27
Figure 4 - Number of publications with “post-sintering” in the title or subject.	27
Figure 5 - Number of publications with “metal alloy” in the title or subject.	28
Figure 6 - Number of publications with “hard metal and sintering” in the title or subject.	28
Figure 7 - Number of publications with “alloy design” in the title or subject.	29
Figure 8 - Schematic lattice occupation of Diamoy alloys.	33
Figure 9 - Relation between wear-rate constant and hardness for different classes of materials.	35
Figure 10 - Sponge iron production from raw materials in Höganäs.	46
Figure 11 - Processes to obtain metal powder.	49
Figure 12 - (a) Planetary ball milling machine; (b) ball milling schematic of vessel from top-view.	50
Figure 13 - (a) batch attritor for wet grinding; (b) continuous attritor for wet grinding.	51
Figure 14 - (a) Infinitesimal element of a hollow sphere under external hydrostatic pressure representing a powder particle; (b) Mohr’s circle of the stress state of (a).	53
Figure 15 - A droplet standing on a surface presenting a pictorial definition of the contact angle.	63
Figure 16 - Two solid particles interfacing to form the dihedral angle.	63
Figure 17 - Two-sphere sintering model, from initial contact to full coalescence.	65
Figure 18 - Vickers measurement.	69
Figure 19 - Vickers measurement.	70
Figure 20 - Electromagnetic spectrum of light, TEM, and SEM.	71
Figure 21 - SEM equipment.	71
Figure 22 - Flowchart of the experimental part of this thesis.	73
Figure 23 - Empty interface of “DIAMOY 2.0”.	75
Figure 24 - DIAMOY 2.0 workflow.	76
Figure 25 - Input field of product mass (in grams) in DIAMOY 2.0.	78
Figure 26 - Molar fraction input in “DIAMOY 2.0”.	79
Figure 27 - Pots of iron, manganese, nickel, chrome, and aluminum powder.	80
Figure 28 - (a) weighing process of the niobium pieces; (b) weighing process of the titanium bar.	81
Figure 29 - Powder mixing with a spoon in the beaker.	82
Figure 30 - (a) pressing equipment; (b) pressing equipment forcing down the pin of the matrix against the hole of the matrix; (c) compacted powder cylinder in the beaker.	84
Figure 31 - Main output field of “PComp” software.	84
Figure 32 - Plasma furnace Rematitan autocast (Dentarium®).	85
Figure 33 - (a) plasma furnace chamber with tungsten electrode; (b) gas cylinder; (c) electrical discharge from the tungsten electrode to the cylinder in the furnace chamber.	85
Figure 34 - (a) flat cylinder ingot mold; (b) slim cylinder ingot mold.	86
Figure 35 - Ingot mold of rectangular cross-section prism.	86
Figure 36 - (a) solidified alloy in a flat cylinder ingot mold; (b) solidified alloy in a slim cylinder ingot mold.	87

Figure 37 - Resin and solidified alloy sanded to be tested.	88
Figure 38 - (a) alloy inside matrix before pressing; (b) alloy being weighted; (c) balls being weighted.	88
Figure 39 - Cylinder sealed with the alloy particles and the balls inside it.	89
Figure 40 - (a) sieving process to separate the acceptable particles from the non-acceptable ones; (b) 500 micrometers sieve (intermediate sieve to reach up to 200 micrometers).	90
Figure 41 - Pycnometer Quantachrome model Ultrapyc 1200e.....	90
Figure 42 - Pressing of the alloy powder to form a compacted cylinder right before sintering.....	91
Figure 43 - Empty interface of “PComp” software.	93
Figure 44 - Computer program “PComp” workflow.	94
Figure 45 - Sintering furnace composed of three modules.....	96
Figure 46 - (a) compacted flat cylinders before going into the sintering furnace; (b) ceramic plate over the sintering chamber base.	97
Figure 47 - (a) cover and insulation placed over the plate in order to form the sintering chamber; (b) flowmeter of the sintering furnace.....	97
Figure 48 - One of the programs created for sintering the compacted cylinders.	98
Figure 49 - Control screen showing: a) ascending ramp being executed in the experiment; b) highest horizontal level in the experiment.....	98
Figure 50 - Hydrostatic weighting.	99
Figure 51 - Empty interface of “SINT” software.	101
Figure 52 - Computer program “SINT” workflow.....	102
Figure 53 - Hardness testing equipment.	103
Figure 54 - Alloy sample wrapped by resin to be scanned.	104
Figure 55 - “PComp” software and its results to compact a flat cylinder.....	105
Figure 56 - Interface of “DIAMOY 2.0” with the results related to L6 alloy.....	107
Figure 57 - Interface of “DIAMOY 2.0” with the results related to L4 alloy.....	108
Figure 58 - Densification per alloy.	113
Figure 59 - Dilatometric profiles up to 1500 °C under Ar-10%H ₂ ; pellets form powdered L4 and L5 alloys with and without 3% Cu additive; retraction rate is also shown for L5Cu; below: Differential Scanning Calorimetry (DSC) curves for L4 and L5 powders.	116
Figure 60 - Window of “SINT” with the results for the proposed problem.	117
Figure 61 - As-cast L4 alloy SEM-BSE full-area: 200x magnification (trace scale 100 μ m).	119
Figure 62 - As-cast L4 alloy SEM-BSE full-area: 500x magnification (trace scale 50 μ m).	119
Figure 63 - (a) As-cast L4 alloy SEM-BSE full-area: 1000x magnification (trace scale 10 μ m).	120
Figure 64 - As-cast L4 alloy SEM-BSE, 400x magnific. (trace scale 50 μ m): (a) 1st; (b) 2nd indentation.	121
Figure 65 - As-cast L4 alloy SEM-BSE: Energy Dispersive Spectroscopy (EDS) map.	122
Figure 66 - As-cast L4 alloy SEM-BSE: EDS element maps of carbon and oxygen.	123
Figure 67 - As-cast L4 alloy SEM-BSE: EDS element maps of titanium and vanadium.....	123
Figure 68 - As-cast L4 alloy SEM-BSE: EDS element maps of chrome and iron. ...	124

Figure 69 - As-cast L4 alloy SEM-BSE: EDS element maps of niobium and molybdenum.....	124
Figure 70 - As-cast L4 alloy SEM-BSE: EDS element map of tantalum.	125
Figure 71 - As-cast L4 alloy SEM-BSE: Chemical composition of one of the white points.....	125
Figure 72 - As-cast L4 alloy SEM-BSE: Chemical composition of one of the gray points.....	126
Figure 73 - As-cast L4 alloy SEM-BSE: Chemical composition of one of the black points.....	127
Figure 74 - As-cast L5 alloy SEM-BSE: 200x magnification (trace scale 100 μm). .	130
Figure 75 - As-cast L5 alloy SEM-BSE: 500x magnification (trace scale 50 μm). ...	130
Figure 76 - As-cast L5 alloy SEM-BSE: 1000x magnification (trace scale 10 μm). .	131
Figure 77 - As-cast L5 alloy SEM-BSE indentations: (a) 1st: 150x magnification (trace scale 100 μm); (b) 2nd: 350x (trace scale 50 μm).	132
Figure 78 - As-cast L5 alloy SEM-BSE: Energy Dispersive Spectroscopy (EDS) map.	133
Figure 79 - As-cast L5 alloy SEM-BSE: EDS element maps for carbon and oxygen.	134
Figure 80 - As-cast L5 alloy SEM-BSE: EDS element maps for titanium and vanadium.....	134
Figure 81 - As-cast L5 alloy SEM-BSE: EDS element maps for chrome and iron...	135
Figure 82 - As-cast L5 alloy SEM-BSE: EDS element maps for niobium and molybdenum.....	135
Figure 83 - As-cast L5 alloy SEM-BSE: EDS element map for tantalum.....	136
Figure 84 - As-cast L5 alloy SEM-BSE: Chemical composition of one of the white points.....	136
Figure 85 - As-cast L5 alloy SEM-BSE: Chemical composition of one of the gray points.....	137
Figure 86 - As-cast L5 alloy SEM-BSE: Chemical composition of one of the black points.....	138
Figure 87 - As-cast L5.1 alloy 1st SEM-BSE: 200x magnification (trace scale 100 μm).	141
Figure 88 - As-cast L5.1 alloy 2nd SEM-BSE: 200x magnification (trace scale 100 μm).	142
Figure 89 - As-cast L5.1 alloy SEM-BSE: 500x magnification (trace scale 50 μm).	142
Figure 90 - As-cast L5.1 alloy SEM-BSE: 1000x magnification (trace scale 10 μm).	143
Figure 91 - As-cast L5.1 alloy SEM-BSE: 3500x magnification (trace scale 5 μm).	143
Figure 92 - As-cast L5.1 alloy SEM-BSE indentations (trace scale 50 μm): (a) 1st. 400x magnification; 2nd 430x magnification.....	145
Figure 93 - As-cast L5.1 alloy SEM-BSE: Energy Dispersive Spectroscopy (EDS) map.	145
Figure 94 - As-cast L5.1 alloy SEM-BSE: EDS element maps for carbon and oxygen.	146
Figure 95 - As-cast L5.1 alloy SEM-BSE: EDS element maps for aluminum and titanium.....	146
Figure 96 - As-cast L5.1 alloy SEM-BSE: EDS element maps for vanadium and chrome.	147
Figure 97 - As-cast L5.1 alloy SEM-BSE: EDS element maps for iron and niobium.	147

Figure 98 - As-cast L5.1 alloy SEM-BSE: EDS element map for molybdenum.	148
Figure 99 - As-cast L5.1 alloy SEM-BSE: Chemical composition of one of the white points (1000x magnification).....	148
Figure 100 - As-cast L5.1 alloy SEM-BSE: Chemical composition of an aluminum oxide points.	149
Figure 101 - As-cast L5.1 alloy SEM-BSE: Chemical composition of one of the white points (3500x magnification).	150
Figure 102 - As-cast L5.1 alloy SEM-BSE: Chemical composition of one of the gray points.....	151
Figure 103 - As-cast L5.1 alloy SEM-BSE: Chemical composition of one of the black points.....	151
Figure 104 - Sintered L4 alloy SEM-BSE: (a) 500x magnification (trace scale 50 μm); (b) 1000x magnification (trace scale 10 μm).	154
Figure 105 - Sintered L5 alloy SEM-BSE: (a) 500x magnification (trace scale 50 μm); (b) 1000x (trace scale 10 μm).	154
Figure 106 - Sintered L5.1 alloy SEM-BSE: (a) 500x magnification (trace scale 50 μm); (b) 1000x (trace scale 10 μm).	155

LIST OF TABLES

Table 1 - Nomenclature of the alloys addressed in this thesis.....	77
Table 2 - Masses of the samples of the alloys obtained in this thesis.	78
Table 3 - Chemical elements, their available forms, and purity.	80
Table 4 - Input data in “PComp”, corresponding data and equations.	92
Table 5 - Sintering parameters for the alloys.....	95
Table 6 - Output data in “SINT”, corresponding data, and equations.	101
Table 7 - Input data in “SINT”, corresponding variables, and values.	102
Table 8 - Comparison of parameter values between (RESTIVO, T. A. G. and RESTIVO, G. M. G., 2021) and the software developed (DIAMOY 2.0) for L6 alloy.	109
Table 9 - Comparison of the available parameter values between (RESTIVO, T. A. G. and RESTIVO, G. M. G., 2021) and DIAMOY 2.0 in what refers to L4 alloy.	109
Table 10 - Hardness values measurements.	110
Table 11 - Densification data for the samples subjected to sintering.....	112
Table 12 - Densification data for the samples subjected to sintering.....	114
Table 13 - Range of the ratio final-theoretical densities $[(\rho_f / \rho_{th}) 100]$ % from minimum to maximum.	115
Table 14 - Minimum, maximum, and average grain sizes for L4 (1000x).	121
Table 15 - Composition before and after carbon and oxygen normalization for L4 alloy.	127
Table 16 - Comparison between theoretical and experimental chemical composition for L4 alloy before carbon and oxygen normalization in the three distinct regions.....	128
Table 17 - Comparison between theoretical and experimental chemical composition for L4 alloy after carbon and oxygen normalization in the three distinct regions.....	129
Table 18 - Minimum, maximum, and average grain sizes for L5 (1000x).	132
Table 19 - Composition before and after carbon and oxygen normalization for L5 alloy.	138
Table 20 - Comparison between theoretical and experimental chemical composition for L5 alloy before carbon and oxygen normalization in the three phases.	139
Table 21 - Comparison between theoretical and experimental chemical compositions for L5 alloy after carbon and oxygen normalization in the three phases.	140
Table 22 - Shape, minimum, maximum, and average grain size by region (3500x).	144
Table 23 - Composition before and after carbon and oxygen normalization for L5.1 alloy.	152
Table 24 - Comparison between theoretical and experimental chemical composition for L5.1 alloy before carbon and oxygen normalization in the three distinct regions.....	152
Table 25 - Comparison between theoretical and experimental chemical composition for L5.1 alloy after carbon and oxygen normalization in the three distinct regions.....	153

LIST OF ACRONYMS AND ABBREVIATIONS

AD	<i>Anno Domini</i>
ASTM	American Society for Testing Materials
BC	Before Christ
BCC	Body-Centered Cubic
CAPES	Coordenação de Aperfeiçoamento de Pessoal de Nível Superior
DOE	Design of Experiments
DSC	Differential Scanning Calorimetry
EDS	Energy Dispersive Spectroscopy
EHMMA	Extremely Hard Multicomponent Metal Alloy
EIGA	Electrode Induction Gas Atomization
EPMA	European Powder Metallurgy Association
FCC	Face-Centered Cubic
HEA	High-Entropy Alloy
HIP	Hot Isostatic Pressure
HSS	High-Speed Steel
HV	Vickers Hardness
ISO	International Standardization Organization
IUPAC	International Union of Pure and Applied Chemistry
NOK	Not OK
PCBN	Polycrystalline Cubic Boron Nitride
PIGA	Plasma-Induced Gas Atomization
PM	Powder Metallurgy
SEM	Scanning Electron Microscopy
TEM	Transmission Electron Microscopy
VEC	Valence Electron Concentration
WC	Tungsten Carbide

SUMMARY

1	INTRODUCTION	23
1.1	Contextualization and Motivation.....	23
1.2	Bibliographic Research.....	24
1.2.1	General Approach.....	24
1.2.2	Bibliometric Research	25
1.3	Objects of Study and Objectives	29
2	EXTREMELY HARD MULTICOMPONENT METAL ALLOY DESIGN.....	31
2.1	Background in Alloy Design.....	31
2.2	Extremely Hard Multicomponent Metal Alloys (EHMMAs).....	32
2.3	Conventional Metal Alloys and High-entropy Alloys (HEAs) vs. Diamoy.	32
2.4	Available Approaches to Design a Metal Alloy.....	36
2.5	Descriptive Parameters to Form a Solid Solution (parametric approach)	366
2.5.1	Atomic Radii Difference, $\Delta r\%$	37
2.5.2	Mean atomic radius, r	37
2.5.3	Polydispersion of atomic radii, δ	377
2.5.4	Chromium equivalent coefficient, C_{req}	38
2.5.5	Topological discrepancy, γ	38
2.5.6	Mean Valence Electron Concentration, V	39
2.5.7	Standard deviation of Valence Electron Concentration, VSD	39
2.5.8	Mean electronegativity, χ	39
2.5.9	Electronegativity difference, $\Delta\chi$	39
2.5.10	Molar-averaged melting point, T	40
2.5.11	Standard deviation of melting points, TSD	40
2.5.12	Mean density, ρ	40
2.5.13	Standard deviation of densities, ρSD	41
2.5.14	Mean bulk modulus, K	411
2.5.15	Standard deviation of bulk modulus, KSD	41
2.5.16	Entropy of mixing, ΔS_{MIX}	41
2.5.17	Average mixing enthalpy, ΔH_{MIX}	42
2.5.18	Standard deviation of mixing enthalpy, HSD	42
2.5.19	Lowered Gibbs' free energy, ΔG_{MIX}	43
2.5.20	Entropy-enthalpy relation, Ω	43
2.5.21	Chemical affinity, A	43
2.5.22	Structure	44

3	POWDER METALLURGY (PM).....	45
3.1	Overall Process	45
3.2	Processes for Obtaining Metal Powder (Highlighting the Mechanical)	48
3.3	Mathematical Modeling of Powder Compact	51
3.3.1	Compaction Pressure, Density, and Porosity.....	52
3.3.2	Loadings and Stresses	52
4	SINTERING.....	59
4.1	Definitions, Phenomena, and Characteristics	59
4.2	Liquid Phase Sintering.....	61
4.3	Mathematical Modeling of Sintering	64
5	TESTING.....	67
5.1	Hardness testing	67
5.1.1	General concepts of hardness	67
5.1.2	Vickers hardness	69
5.2	Scanning electron microscopy (SEM)	70
6	MATERIAL AND METHODS	73
6.1	Software Developed for EHMMAs Design (DIAMOY 1.0 updated to DIAMOY 2.0)	73
6.2	Obtainment of Powder Mix	76
6.2.1	Definition of the parameters to select the elements to compose the alloy	76
6.2.2	Determination of the mass enough to manufacture the product or sample.....	77
6.2.3	Calculation of the mass of each alloy element.....	79
6.2.4	Obtainment of the powder referred to each alloy element	79
6.2.5	Weighing of each powder mass (metallic powder of each alloy element)	80
6.2.6	Mixing of the powders in the most homogeneous manner.....	81
6.3	Obtainment of Compacted Powder Blend.....	82
6.3.1	Pressing (compaction) of the powder mass.....	82
6.3.2	Melting of the compacted powder	84
6.3.3	Solidification of the molten alloy.....	87
6.3.4	Separation of a sample for verification of hardness and chemical composition	87
6.3.5	Transformation of the remaining part of the solidified alloy into powder (blend) and sieving to use granulation powder of up to 200 micrometers.....	88
6.3.6	Powder density obtainment.....	90
6.3.7	Compaction of the blend in almost final dimensions of the product	91
6.4	Software Developed for Powder Compaction	91
6.5	Sintering	94
6.5.1	Furnace employed	96

6.5.2	Sintered part density obtainment	99
6.5.3	Dilatometry.....	99
6.6	Software Developed for Sintering	100
6.7	Alloy Testing	102
6.7.1	Hardness testing.....	102
6.7.2	Scanning electron microscopy (SEM) testing and dilatometry	103
7	RESULTS AND DISCUSSION.....	105
7.1	Powder Compaction	105
7.2	Prediction of the Designed Alloys Using the Software “DIAMOY 2.0” ..	106
7.3	Hardness Values.....	110
7.4	Sintering Results	111
7.4.1	Sintering results from experiments	111
7.4.2	Dilatometry Results.....	115
7.4.3	Sintering results from SINT software	117
7.5	Scanning Electron Microscopy, Backscattered Electrons (SEM-BSE), and Energy-dispersive X-rays Spectrometer (DSC) Results	118
7.5.1	As-cast L4 alloy SEM-BSC results.....	118
7.5.2	As-cast L5 alloy SEM-BSC results.....	129
7.5.3	As-cast L5.1 alloy SEM-BSC results.....	141
7.5.4	Sintered L4, L5, and L5.1 alloys SEM-BSC results.....	153
7.6	Intellectual Production Within This Thesis	155
8	CONCLUSIONS	157
8.1	Main Conclusions, Contributions, and Final Considerations	157
8.2	Suggestion for Future Works	158
	REFERENCES.....	159

1 INTRODUCTION

This chapter presents an introduction to extremely hard multicomponent metal alloys (EHMMAs), powder metallurgy, sintering, and alloy design, highlighting the objectives of this research, the work content, and a brief bibliometric research related to the main research keywords.

1.1 Contextualization and Motivation

A great variety of materials has been developed by researches conducted all over the world aiming at providing solutions to the most distinguished types of applications. Notoriously, when the requirement is to enhance the life span of a part, tougher and harder materials are then demanded. In view of these features, the most widely employed materials to solve this problem are generally the extremely hard metal alloys (e.g. superalloys and special steels) and the metallic-ceramic composites (viz. carburized carbides or hard metal).

In this context, the mechanical properties of pure metals can be highly improved by means of alloying each one with other metals or non-metallic elements ([RAZUAN et al., 2013](#)). These traditional alloys are conceived with a maximum of one or two main elements ([SHUN et al., 2012](#)). Another solution refers to the so-called multicomponent alloys, which contain three or more main elements. Although they may represent the solution required in many situations, they may form intermetallic compounds dotted with complex microstructures associated with mechanical properties of unwanted magnitudes.

In order to fulfill this gap, the so-called high-entropy alloys (HEAs) emerged, in which their design is based on at least five main elements (concentrations varying between 5 and 35% in molar terms). This denomination is due to their high entropic effects in solidification process, thus promoting simple solid solutions, in contrast with the formation of complex phases.

In what concerns hardness, the conventional metal alloys and steels may reach magnitudes around 1100 *HV* (Vickers' hardness, *kgf/mm²* for a load of 45 *N*), e.g. the M40-series high-speed steel (HSS) ([DENNIS, 1993](#)). Carburized, nitrided, and boronized alloys may achieve 1900 *HV* for a load of 500 *kgf* ([KLAUS, 1993](#)). However,

after heat-treated, the currently available alloys commonly present a considerable degree of ceramic phases, which gives them a brittleness character.

Given these limitations and, therefore, aiming at providing materials with a higher life span by means of wear resistance improvement, Diamoy alloys were just introduced ([RESTIVO, T. A. G.; RESTIVO, G. M. G., 2021](#)). These alloys, yet under development, have six to nine metallic elements. On both laboratory and industrial scale, the values of hardness are the highest ever recorded when compared to the other metallic materials, even overcoming those of ceramic oxides. For comparison purposes: (a) without heat treatment, Diamoy alloys may reach up to 1420 *HV* for a load of 2 *N* (value higher than that presented by the conventional metal alloys, achieving around 1100 *HV*); (b) when heat treated, Diamoy alloys reach the baseline of 2500 *HV* for a load of 2 *N* (higher than carburized, nitrided, and boronized alloys, in the order of 1900 *HV*).

Associated to the high hardness of Diamoy (relatively to the current metallic materials), the ductility greater than 20% and the fracture toughness ranging from 8 to 20 $\text{MPa}\cdot\text{m}^{1/2}$ ([RESTIVO, T. A. G.; RESTIVO, G. M. G., 2021](#)) may enable them to be manufactured by more economical processes. In addition, Diamoy alloys have a body-centered cubic (BCC) crystalline structure, with two or three indexed phases. This indicates a high potential for metallic applications in which it is required electrical/thermal conductivities, manufacturability, corrosion resistance, etc.

Behind all these discoveries, a lot of research work has been conducted in the direction of design of EHMMAs, which demands very intense research and experimentation. Therefore, EHMMAs must be tested upon many conditions in order to be feasible, and to be able to constitute a useful product.

1.2 Bibliographic Research

General approach and bibliometric research are presented in this subsection.

1.2.1 General Approach

With the aim of obtaining solutions for problems within the context presented herein, a methodology that combines alloy design parameters, powder metallurgy, and sintering is proposed to perform the manufacturing of extremely hard multicomponent

metal alloys. To manage this, a specific design framework (including the experiments) is also needed in order to provide an organized and detailed manner to deal with these particularities.

1.2.2 Bibliometric Research

In order to check the importance of the related scientific areas treated herein and capture research gaps, some bibliometric researches were conducted, which first round results are shown in the next seven figures (Figs. 1 to 7). All plots cover the ten-year period from 2012 to 2021 and indicate the number of works (peer reviewed papers) published in what relates to the search word in CAPES ([*Coordenação de Aperfeiçoamento de Pessoal de Nível Superior, 2022*](#)) information repository. “Hard metal”, “powder metallurgy”, “sintering”, “post-sintering”, “metal alloy”, “hard metal and sintering”, and “alloy design” were the searched words, which are presented in [Fig. 1](#), [Fig. 2](#), [Fig. 3](#), [Fig. 4](#), [Fig. 5](#), [Fig. 6](#), and [Fig. 7](#), respectively.

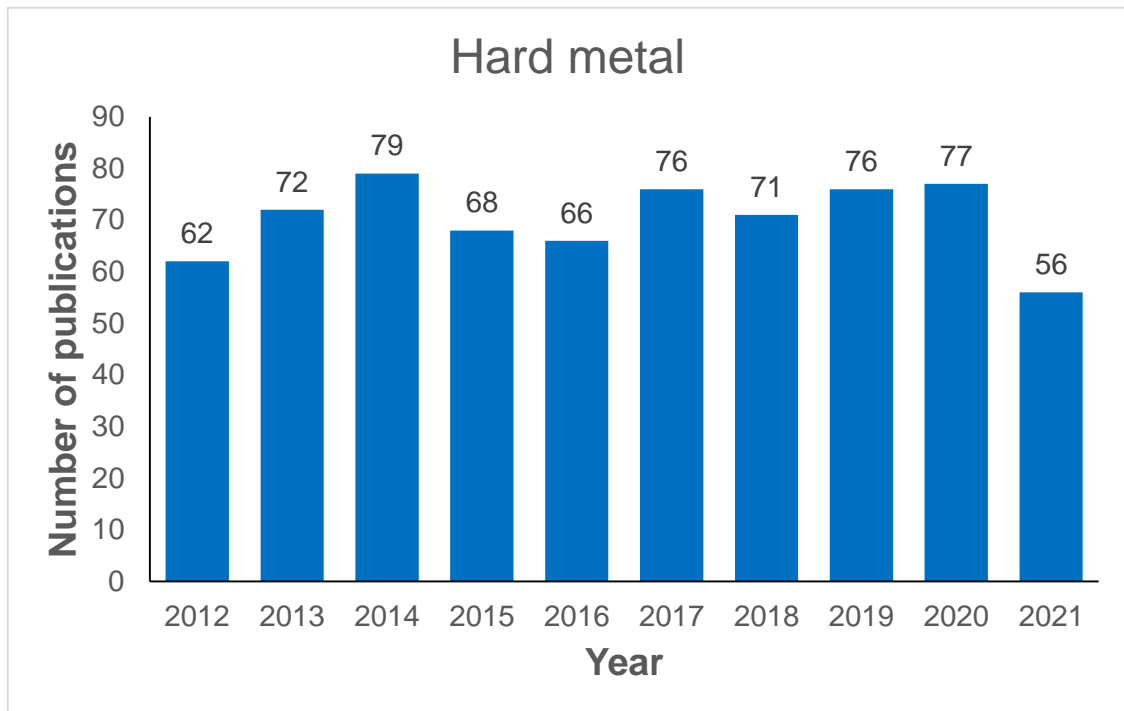
It is worth noting that when “hard metal” ([Fig. 1](#)), “post-sintering” ([Fig. 4](#)), “hard metal and sintering” ([Fig. 6](#)) are the research words, the results over the referred ten-year period tend to be stable. However, for the research words “powder metallurgy” ([Fig. 2](#)), “sintering” ([Fig. 3](#)), “metal alloy” ([Fig. 5](#)), and “alloy design” ([Fig. 7](#)), there is a trend to increase the number of publications, turning the research area yet more active.

A second round of research was conducted covering the same period of the first round research, but now with the following search words and results:

- (a) “hard metal” and “software” (it did not returned results);
- (b) “powder metallurgy” and “software” (it did not returned any result);
- (c) “sintering” and “software” (which returned two results);
- (d) “post-sintering” and “software” (no results);
- (e) “metal alloy” and “software” (no results);
- (f) “hard metal”, “sintering”, and “software” (no results);
- (g) “alloy”, “design”, and “software” (it returned two results).

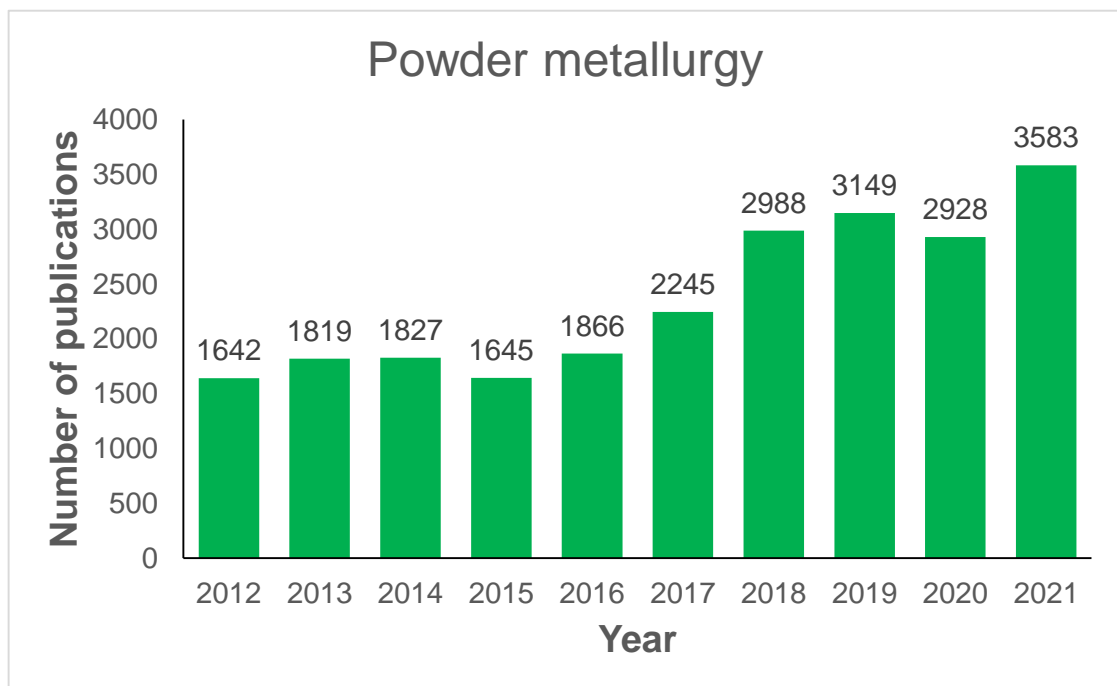
The obtained results for the second round of research, i.e. no works published or few of them published, indicate that there is a relatively good opportunity to original contributions in the referred areas when the word “software” is applied concomitantly with the other research words.

Figure 1 - Number of publications with “hard metal” in the title or subject.



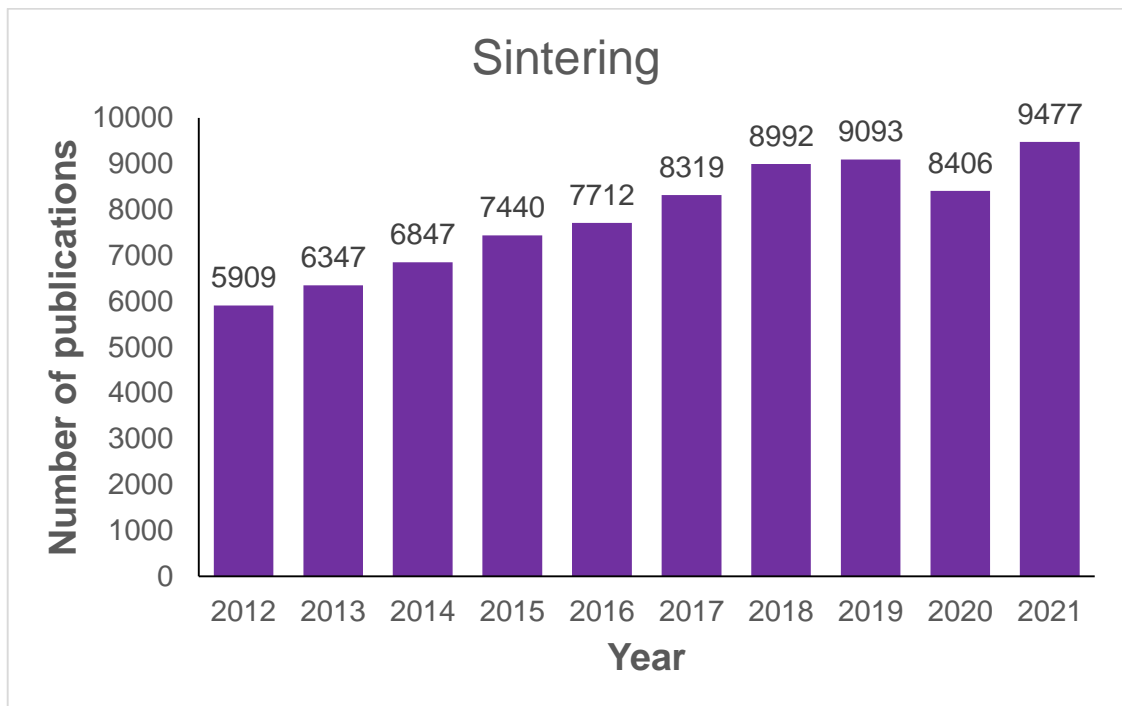
Source: [CAPES, 2022](#).

Figure 2 - Number of publications with “powder metallurgy” in the title or subject.



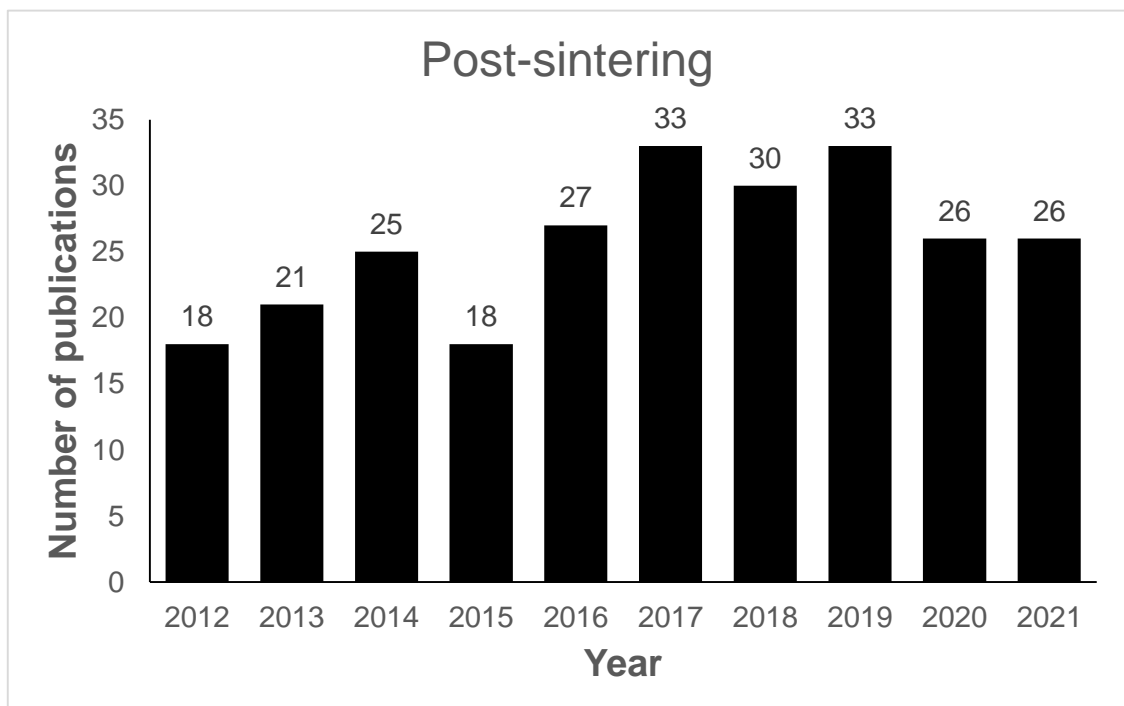
Source: [CAPES, 2022](#).

Figure 3 - Number of publications with “sintering” in the title or subject.



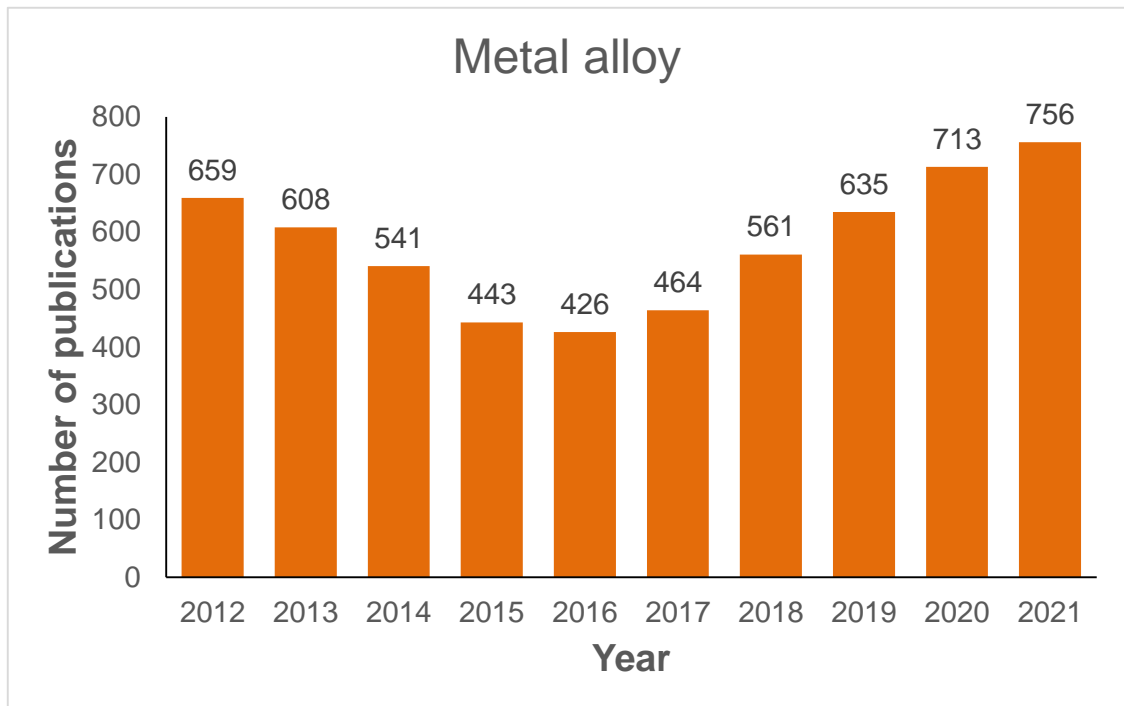
Source: [CAPES, 2022](#).

Figure 4 - Number of publications with “post-sintering” in the title or subject.



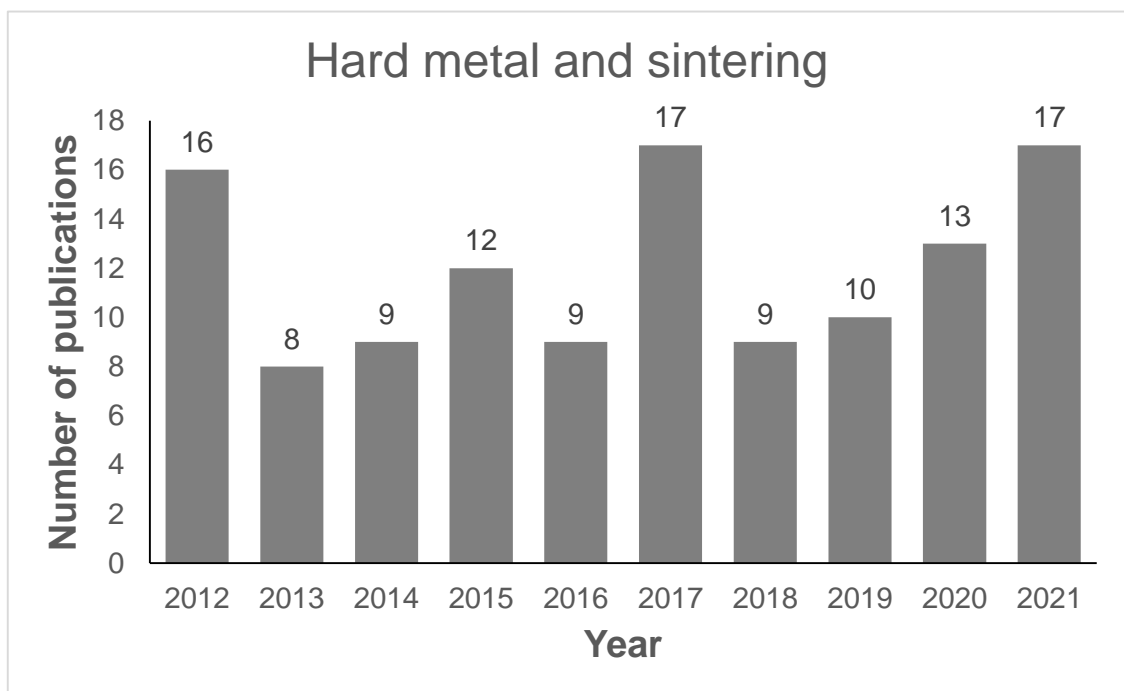
Source: [CAPES, 2022](#).

Figure 5 - Number of publications with “metal alloy” in the title or subject.



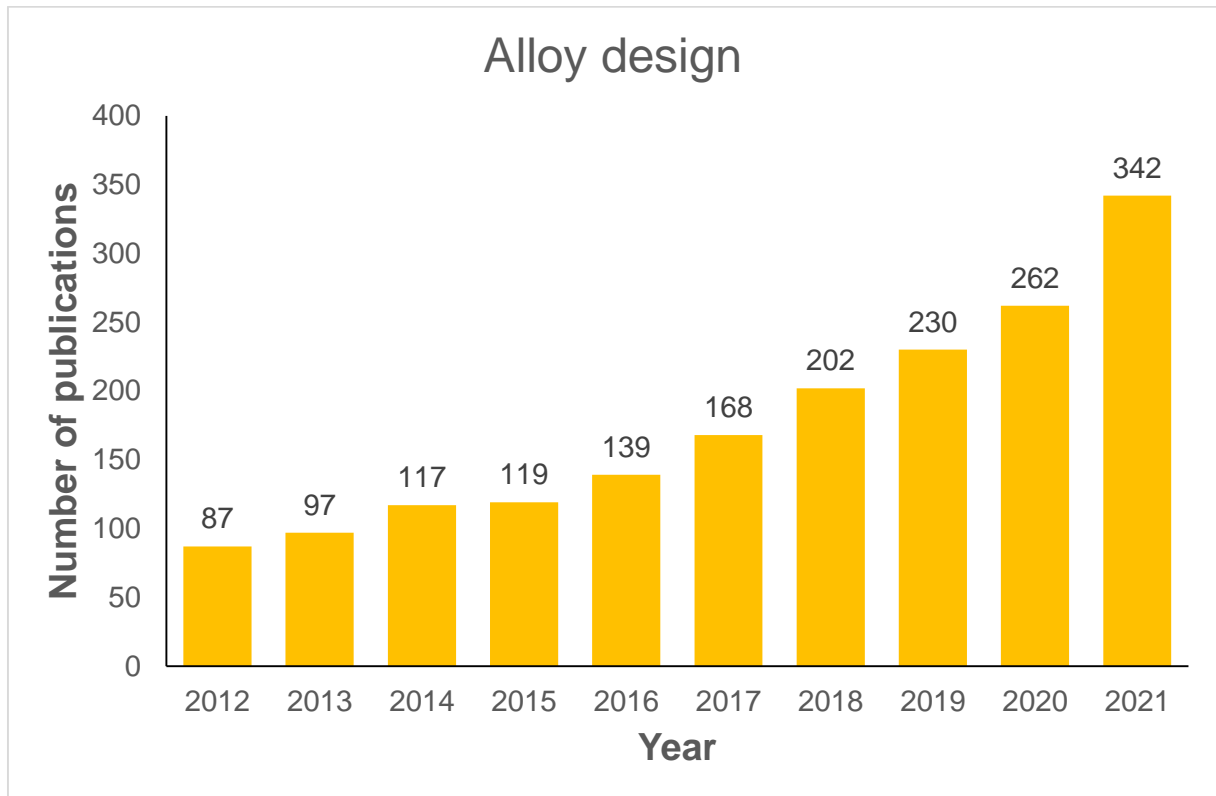
Source: [CAPES, 2022](#).

Figure 6 - Number of publications with “hard metal and sintering” in the title or subject.



Source: [CAPES, 2022](#).

Figure 7 - Number of publications with “alloy design” in the title or subject.



Source: [CAPES, 2022](#).

1.3 Objects of Study and Objectives

Extremely hard multicomponent metal alloys (EHMMAs) are studied in the context of powder metallurgy, sintering, and design by a theoretical-experimental approach. Therefore, the main objective of this thesis is to predict the feasibility of some EHMMAs yet in the design phase (by creating a design framework), and process them in order to characterize their structures. The deployment of the main objective yields the following specific objectives:

- a) To test the treated alloys by means of hardness tests, and Scanning Electron Microscopy (SEM).
- b) To specify the alloys arising from this thesis according to their composition, processing and treatment.
- c) To melt together all the alloying elements to form the most homogeneous ingot as possible.
- d) To obtain powders from cast alloys ingots.
- e) To study the compaction and sintering of alloys powders.

- f) To create computational tools to input an adequate compaction pressure to aggregate the alloy powder, to predict the feasibility of EHMMAs, and to calculate sintering parameters.
- g) To establish a design framework for EHMMAs.

2 EXTREMELY HARD MULTICOMPONENT METAL ALLOY DESIGN

This chapter includes background, fundamental principles to form an alloy, extremely hard multicomponent metal alloys, approaches in alloy design, and descriptive parameters to form a solid solution.

2.1 Background in Alloy Design

In an ever-growing demanding society, materials frequently become the critical barrier to technological advance. In metals, one of the branches deal with requirements defined and solved by an existing alloy, but with different composition; another branch is described by applications in which the properties of the existing alloys do not fulfill the problem requirements, thus requiring a new material.

The processes of strengthening metals can be found by means of cold working and alloying ([JAFEE; WILCOX, 1975](#)). The mixture of two or more chemical elements forms an alloy, since at least one of them is a metal ([PFEILER, 2007](#)). The mixture of one or more metals with nonmetallic elements forms an engineered material called alloy ([INAMUDDIN *et al.*, 2020](#)). In the case of forming a solid solution, the alloying element is distributed over the crystal lattice sites. However, in the case of forming different phases the alloying element can be found as particles in a matrix. The properties of a solid solution are governed by the chemical composition of the elements, whereas those of a multiphase alloy are regulated by the distribution of the particles of the other phases. The innumerable possibilities to form alloys are determined by the selection of alloying elements and their concentrations.

Among the characteristics planned to be obtained in an alloy design, the reduction of friction between parts implies in minimizing the energy loss during operation. Consequently, the efficiency is maximized. Another two desired characteristics are fatigue strength and wear rate, directly related to life span. It is somewhat difficult to fulfill these requirements with just pure or conventional materials. In view of this, there is an acute demand for alloys, as they can be designed for specific purposes. Therefore, alloys may be designed to blend the properties of its constituents. Consequently, a better-suited material can be obtained ([SARAVANAN; RANI, 2012](#)).

2.2 Extremely Hard Multicomponent Metal Alloys (EHMMAs)

It is not certain when the search for more resistant materials began, however it indeed started to intensify in the Age of Metals (3000 to 1000 BC). For centuries, the mineralogists have been applying hardness to characterize the most different types of materials ([GILMAN, 2009](#)). Another milestone was early in the twentieth century, when the three most widespread hardness scales were developed (Rockwell, Brinell, and Vickers) ([HERRMANN, 2011](#)). One of the most highlighted findings refers to the fact that carbon takes part in the formation of tungsten carbide (WC) crystals, extremely hard materials. In 1927, the German company Krupp® workers found that WC crystals could be carburized with cobalt, in order to serve as cutting tools of life span longer than those then available ([RIEDEL, 2000](#)). Aluminum oxide (Al_2O_3) and silicon carbide (SiC) are also intended for the same application, besides diamond and boron cubic nitride (BN).

Another important milestone to be highlighted refers to the aeronautical industry and its development throughout world wars. In order to turn this industry more competitive, copper and magnesium were added to aluminum aiming at hardening the alloy that constitutes primary and secondary structural members. Posteriorly, duralumin and super alloys were created ([KAZANTSEVA et al., 2019](#)).

However, the most important finding in the last years refers to high-entropy alloys (HEAs), considered a rupture with the conventional physical metallurgy ([WANG et al., 2015](#)). This can be verified by the volume of research conducted about this subject, aiming at improving the mechanical properties of the developed material. In terms of hardness, some of them are here reported: CrMnFeVTi (835 HV) ([SONG et al., 2018](#)), AlCoFeMoNiTi (1000 HV) ([BALDENEBO-LOPEZ et al., 2015](#)), and CrMoNbWTi (1211 HV) ([LV et al., 2020](#)).

2.3 Conventional Metal Alloys and High-entropy Alloys (HEAs) vs. Diamoy

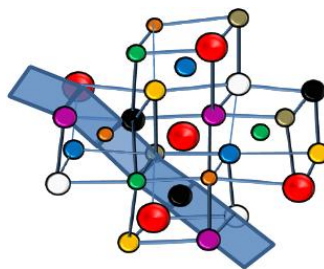
As far as this research could reach, conventional metal alloys of the most varied compositions may reach hardness magnitudes limited to approximately 1100 HV (HSS M40) ([KLAUS, 1993](#)). The following alloys also stand out in this scenery: Mg-Y-Sm-Zn-Zr alloys (148 HV) ([LYU et al., 2018](#)), Al_3Ni_2 (898 HV) ([KRASNOWSKI et al., 2013](#)), $\text{Mg}_{97}\text{Y}_2\text{Zn}_1$ (245 HV) ([YOUSSEF et al., 2011](#)), and AlCrMnMoNiZrB_{0.1} (1330 HV) ([REN](#)

[et al., 2011](#)), among others, which research mainly showed the increase of hardness (according to the obtaining mode and/or heat treatment applied). Nevertheless, the hardest alloys ever produced are the so-called metallic glasses, e.g. $W_{20}Re_{40}B_{20}$ (2400 HV) ([KLAUS, 1993](#)).

The need to lengthen the lifespan of a part by rising its hardness is increasingly prominent in research for many applications. For example, to reduce the wear from the components subjected to reciprocal movement, coatings may represent a possible solution, e.g. Ti-Ni-C ([DANIEL et al., 2017](#)), CrC ([HOUDKOVÁ et al., 2018](#)), and CrNbTaTiW ([FRITZE et al., 2018](#)). In what refers to cutting tools with insert, wear measurements of the most applied materials have been reported. Among them, C-Cr ([SHALABY et al., 2014](#)), WC ([AKMCIOGLU et al., 2016](#)), and polycrystalline cubic boron nitride, PCBN, ([SAKETI et al., 2015](#)). Additionally, for this last application, new heat treatments have been proposed aiming at improving life span of cutting tools under operation, e.g. cryogenic for HSS ([PRAKASH et al., 2016](#)), titanium carbide, TiC, ([GUTIERREZ-NODA et al., 2019](#)), and boride diffusion in AISI M2 steel. There are also techniques such as carburization, nitriding, carbonitriding, boronizing, thermal reactive deposition (boronchrometitanizing, boronchrome vanadization, among others).

Nonetheless, most of the alloys currently recognized as the hardest are amorphous and brittle, which reduces their scope of application. In contrast, Diamoy alloys, which design is based on lattice occupation, have a BCC structure, providing alloys up to nine distinct elements. The different atomic radii may provoke severe distortions, changing the symmetry of the unit cell, which may result in solid solution hardening, as per [Fig. 8](#).

Figure 8 - Schematic lattice occupation of Diamoy alloys.



Source: [RESTIVO, T. A. G.; RESTIVO, G. M. G., 2021](#).

This arrangement provides difficulty in the dislocation movements throughout the lattice of different elements, thus restricting deformation. The degree of the imposed difficulty implies the corresponding increase in hardness and wear resistance, a phenomenon that may be understood, for example, by the act of sliding a surface over another, inducing material removal of both surfaces. Against this situation, the wear rate, W , is defined in Eq. 1:

$$W = \frac{V_R}{D_S}, \quad (1)$$

where V_R is the volume of material removed, and D_S is the sliding distance. The concept of specific wear rate, Ω , is expressed by Eq. 2:

$$\Omega = \frac{W}{A_N}, \quad (2)$$

in which A_N is the nominal contact area. Combining the concept from Eq. 2 to the contact pressure, P , yields the wear-rate constant, k_a , (Eq. 3),

$$k_a = \frac{\Omega}{P}, \quad (3)$$

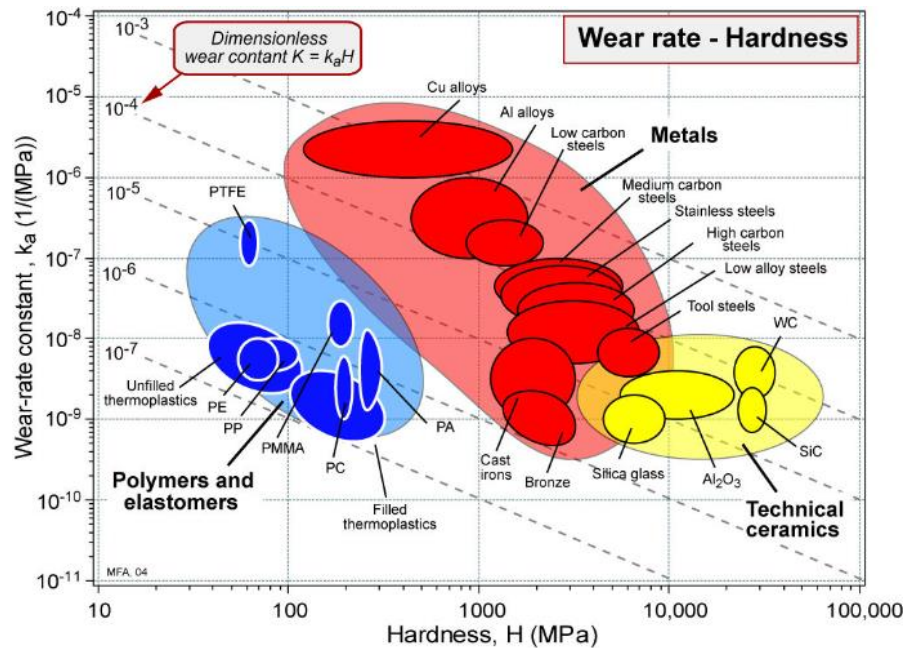
which represents the propensity of a sliding pair for wear, such that a low magnitude of this parameter indicates a low wear at a certain contact pressure P . Thus, P can be given by the ratio between the nominal contact force, F_N , and A_N , as can be seen in Eq. 4:

$$P = \frac{F_N}{A_N}. \quad (4)$$

Alternatively, it is possible to associate hardness to wear using materials charts, as per [Fig. 9](#). In this type of plot, the wear-rate constant is related to hardness for distinct material classes. It can be noted that, in general, metallic ones (in red) are less hard and wear resistant than ceramics (in yellow). However, Diamoy alloys, when

reaching the hardness magnitudes already mentioned here, put themselves as an alternative to both metal alloys and ceramic materials in terms of hardness and, therefore, life span.

Figure 9 - Relation between wear-rate constant and hardness for different classes of materials.



Source: [ASHBY et al., 2019](#).

In this context, even in a preliminary character, Diamoy alloys present significant results because they exhibit a hardness range of 850 to 1420 *HV* in the as-cast state. When subjected to carburization, they present hardness values between 1247 to 2507 *HV* ([RESTIVO, T. A. G.; RESTIVO, G. M. G., 2021](#)). Thus, through the comparison between Diamoy and those then denominated the hardest ever known, e.g. Fe_{49.7}Cr_{17.7}Mn_{1.9}Mo_{7.4}W_{1.6}B_{15.2}C_{3.8}Si_{2.4} (1660 *HV*) ([GUTIERREZ-NODA et al., 2019](#)), AlCrMnMoNiZrB_{0.1} (1330 *HV*) ([REN et al., 2011](#)), WC-5TiC-10Co (1484 *HV*) ([BURAVLEV et al., 2021](#)), and WB₄, ReB₂, YB₁₂, and ZrB₁₂ (2447 *HV*) ([DOVALE-FARELO et al., 2021](#)) it can be partially concluded that there is the possibility to design harder and tougher alloys than the currently available, also trying to aggregate adequate properties to their manufacturability.

2.4 Available Approaches to Design a Metal Alloy

Within the context of an ever-growing research field like EHMMA, as far as this research could reach, there are at least three approaches frequently applied to design an alloy: (a) molecular dynamic (MD) simulations ([GAO; ALMAN, 2013](#)) ([XIE *et al.*, 2013](#)); (b) calculation phase diagrams (CALPHAD) ([ZHANG *et al.*, 2012](#)) ([ZHANG *et al.*, 2014](#)); and (c) parametric approach, which is a method to design multi-component alloys by using a set of parameters and criteria ([TAZUDDIN *et al.*, 2016](#)) ([TAZUDDIN *et al.*, 2017](#)).

The last approach (selected as the applied approach in this thesis) consists in calculating a set of parameters and evaluating a collection of criteria that, theoretically, leads to stable solid solutions. In the field of HEAs, for example, a unique set of parameters and criteria is proposed in each work to obtain the specific results reported. Moreover, each combination of elements may behave in a unique manner, implying in a particular set of parameters and criteria to be fulfilled. Therefore, there may be relative difficulty in recognizing and adopting the most adequate set to produce the required solid solution stability. In view of the difficulty in determining the most adequate set of parameters and criteria, a potential solution may be the utilization of the most relevant and all those frequently reported. As far as this research could reach, there is not yet a solution that aggregates the most common parameters and criteria in a computational tool.

2.5 Descriptive Parameters to Form a Solid Solution (parametric approach)

When an EHMMA is intended to be designed, the prediction of its characteristics and properties can be obtained via the so-called parametric approach ([TAZUDDIN *et al.*, 2017](#)), which consists in the calculation of a set of descriptive parameters and in the fulfillment of several criteria associated with some of the calculated design parameters. Among all available parameters in the literature, twenty-two are available, however twenty (all except chemical affinity and structure) are considered in this work due to their frequency of appearance. In addition, five criteria were considered, each associated with a specific parameter, which provides statuses about the feasibility of solid solution formation. The results from the application of this approach may lead to the obtainment of a solid solution, intermetallic-containing alloy, or metallic glass, for

example. Therefore, the set of descriptive parameters and criteria are addressed here in order to predict the solid solution stability.

2.5.1 Atomic Radii Difference, $\Delta r(\%)$

Let r_s and r_L be, respectively, the smallest (substitutional) and the largest (matrix) atomic radii of the solid solution. Therefore, the atomic radii difference is defined by the difference between the largest and the smallest atomic radii of the chemical elements involved over the matrix atomic radius (Eq. 5). The criteria associated to this parameter is that if this difference is lower than 15%, the solid solution effectively occurs ([WANG et al., 2019](#)), i.e. the first rule of Hume-Rothery,

$$\Delta r(\%) = \frac{r_L - r_s}{r_L} 100. \quad (5)$$

2.5.2 Mean atomic radius, \tilde{r}

Eq. 6 indicates the weighted average of atomic radii of the chemical elements involved in the metal alloy ([SINGH et al., 2014](#)), in which n is the number of elements employed in the alloy design, and the pair f_i and r_i are, respectively, the molar fraction and the radius of the i -th element. Mean atomic radius is given by

$$\tilde{r} = \sum_{i=1}^n f_i r_i. \quad (6)$$

2.5.3 Polydispersion of atomic radii, δ

This parameter represents the mean square deviation of the atomic radii of the involved elements (Eq. 7), which influences the atomic packing. The criteria associated to this parameter states that, with some exceptions, if $1.1 \leq \delta \leq 6.6\%$ the solid solution tends to be stable ([YANG; ZHANG, 2012](#)). If the bonds are distorted, a certain degree of strain is present ([SINGH et al., 2014](#)). In other words, in a physical sense, it is a measure of distortion of the ideal lattice:

$$\delta = \sqrt{\sum_{i=1}^n f_i \left(\frac{1-r_i}{\tilde{r}} \right)^2} . \quad (7)$$

2.5.4 Chromium equivalent coefficient, Cr_{eq}

Its value is obtained from the calculation of the ferrite-forming elements in order to measure the formation of δ -ferrite, which, in turn, is known to reduce the notch toughness when fatigue overcomes the other involved phenomena ([RYU; YU, 1998](#)). Theoretically, the higher the chromium equivalent coefficient the more it approaches to a body-centered cubic (BCC) structure, which increases the hardness ([RESTIVO, T. A. G.; RESTIVO, G. M. G., 2021](#)). High Cr_{eq} sums expand BCC fields of stability and elements solid solution into this structure. Eq. 8 presents the expression to obtain Cr_{eq} , where each chemical symbol represents the respective weight percentage in the solid solution:

$$Cr_{eq} = Cr + 0.8 Si + 2 Mo + W + 4 V + 2 Nb + 1.7 Al + 60 B + 2 Ti + Ta + \\ - 2 Ni - 0.4 Mn - 0.6 Co - 0.6 Cu - 20 N - 20 C . \quad (8)$$

2.5.5 Topological discrepancy, γ

It measures the influence of smallest and largest atoms in a solid solution in a non-linear expression. The topological discrepancy is argued to be the result of the Fermi level being close to a van Hove singularity in the density of states ([BATT, 2008](#)). The associated criteria specify that the calculated γ , given by Eq. 9, should be smaller than 1.175:

$$\gamma = \frac{1 - \sqrt{\frac{(r_L + \tilde{r})^2 - \tilde{r}^2}{(r_L + \tilde{r})^2}}}{1 - \sqrt{\frac{(r_S + \tilde{r})^2 - \tilde{r}^2}{(r_S + \tilde{r})^2}}} . \quad (9)$$

2.5.6 Mean Valence Electron Concentration, \tilde{V}

The third rule of Hume-Rothery states that metals with the same type of crystalline structure may form extensive series of solid solution ([GUO, 2011](#)). The mean valence electron concentration parameter, representing the average periodic table group number, is given by Eq. 10, in which V_i is the value electron concentration of the i -th element involved in the solid solution. It depends on the conditions of each alloy configuration ([GUO, 2011](#)). The criteria related to this parameter is that BCC structure is stable for $\tilde{V} < 6.87$, and FCC structure is stable for $\tilde{V} \geq 8$; otherwise, FCC predominantly occurs, but BCC may occur in some circumstances:

$$\tilde{V} = \sum_{i=1}^n f_i V_i . \quad (10)$$

2.5.7 Standard deviation of Valence Electron Concentration, V_{SD}

As a statistical tool, the standard deviation of valence electron concentration represents the degree of dispersion of valence electron concentration of each element related to the mean and it is given by Eq. 11 ([SINGH et al., 2014](#)),

$$V_{SD} = \sqrt{\sum_{i=1}^n f_i (V_i - \tilde{V})^2} . \quad (11)$$

2.5.8 Mean electronegativity, $\tilde{\chi}$

It is given by Eq. 12 ([GUO, 2011](#)), where χ_i is the Pauling electronegativity of the i -th element of the solid solution,

$$\tilde{\chi} = \sum_{i=1}^n f_i \chi_i . \quad (12)$$

2.5.9 Electronegativity difference, $\Delta\chi$

Eq. 13 denotes the electronegativity difference, parameter that influences the phase separation and new phase formation ([FANG et al., 2013](#)). Although there is not a criterion to establish a range to obtain a single-phase solid solution, in general,

intermetallic compounds can be minimized or even avoided for relatively small values of electronegativity difference. In other words, this parameter represents the standard deviation of electronegativity, i.e. the fourth rule of Hume-Rothery,

$$\Delta\chi = \sqrt{\sum_{i=1}^n f_i (\chi_i - \tilde{\chi})^2} . \quad (13)$$

2.5.10 Molar-averaged melting point, \tilde{T}

Given by Eq. 14, the molar-averaged melting point is the weighted average of the melting points of the involved chemical elements ([SINGH et al., 2014](#)), where T_i is the melting point of the i -th element of the solution, i.e.

$$\tilde{T} = \sum_{i=1}^n f_i T_i . \quad (14)$$

2.5.11 Standard deviation of melting points, T_{SD}

This parameter represents the standard deviation of the melting points of the involved elements ([SINGH et al., 2014](#)), expressed by Eq. 15:

$$T_{SD} = \sqrt{\sum_{i=1}^n f_i (T_i - \tilde{T})^2} . \quad (15)$$

2.5.12 Mean density, $\tilde{\rho}$

This parameter corresponds to the molar-averaged density of the alloy, where ρ_i is the density of the i -th element of the solution, according to Eq. 16,

$$\tilde{\rho} = \sum_{i=1}^n f_i \rho_i . \quad (16)$$

2.5.13 Standard deviation of densities, ρ_{SD}

The referred parameter (Eq. 17) indicates the standard deviation of the densities of the involved elements:

$$\rho_{SD} = \sqrt{\sum_{i=1}^n f_i (\rho_i - \tilde{\rho})^2} . \quad (17)$$

2.5.14 Mean bulk modulus, \tilde{K}

The bulk modulus of a material indicates its resistance to volume compression under hydrostatic pressure. It is normally applied to assess the incompressibility of a material ([HUANG; VITOS, 2022](#)). Furthermore, as shown in ([WU et al., 2015](#)), the bulk modulus strongly depends on the atomic radius. In view of this, the mean bulk modulus represents the weighted average of the bulk moduli of the alloy elements (Eq. 18), where K_i , given by Eq. 19, represents the bulk modulus of the i -th element of the solid solution, in which $(V_0)_i$ denotes the initial volume of the i -th element, and P is the applied pressure:

$$\tilde{K} = \sum_{i=1}^n f_i K_i , \quad (18)$$

$$K_i = -(V_0)_i \frac{dP}{d(V_0)_i} . \quad (19)$$

2.5.15 Standard deviation of bulk modulus, K_{SD}

It is given by Eq. 20 ([SINGH et al., 2014](#)):

$$K_{SD} = \sqrt{\sum_{i=1}^n f_i (K_i - \tilde{K})^2} . \quad (20)$$

2.5.16 Entropy of mixing, ΔS_{MIX}

From Boltzmann's hypothesis, Eq. 21 ([LI; ZHANG, 2009](#)) expresses the entropy of mixing of an n -element solution alloy:

$$\Delta S_{MIX} = -R \sum_{i=1}^n f_i \ln(f_i), \quad (21)$$

where $R = 8.314 \text{ J / mol K}$ is the universal gas constant. When $\Delta S_{MIX} \geq 1.61 R$ ($13.38 \text{ J / mol / K}$), the solid solution is considered to be stabilized ([LI et al., 2009](#)). In addition, an increased value of ΔS_{MIX} tends to favor the solid solution formation. However, concomitantly with a higher value of δ , the opposite tendency is observed, leading to a compound formation ([YANG; ZHANG, 2012](#)).

2.5.17 Average mixing enthalpy, ΔH_{MIX}

It is given by the regular solution model ([TAKEUCHI; INOUE, 2001](#)), i.e. Eq. 22:

$$\Delta H_{ALLOY}^{MIX} = \sum_{i=1; i \neq j}^{nC_2} \Delta H_{c_i, c_j}^{MIX}, \quad (22)$$

in which c_i and c_j are the normalized fraction of the i -th and j -th constituents of the solid solution (as per Eq. 23 and 24, respectively), nC_2 is the number of atomic pairs, and $\Delta H_{c_i, c_j}^{MIX}$ is the mixing enthalpy of binary liquid alloys formed by the i -th and j -th elements of the solid solution (given by Eq. 25):

$$c_i = \frac{f_i}{f_i + f_j}, \quad (23)$$

$$c_j = \frac{f_j}{f_i + f_j}, \quad (24)$$

$$\Delta H_{c_i, c_j}^{MIX} = 4 c_i c_j \left(\sum_{k=0}^3 \Omega_k (c_i - c_j)^k \right), \quad (25)$$

where Ω_k is the k -th factor of third order approximation polynomial (calculated by Miedema's scheme). The values of these factors are found in tables for each atomic pair ([TAKEUCHI; INOUE, 2001](#)).

2.5.18 Standard deviation of mixing enthalpy, H_{SD}

It is expressed by Eq. 26 ([SINGH et al., 2014](#)):

$$H_{SD} = \sqrt{\sum_{i \neq j} f_i f_j \left(\Delta H_{c_i, c_j}^{MIX} - \Delta H_{ALLOY}^{MIX} \right)^2} . \quad (26)$$

2.5.19 Lowered Gibbs' free energy, ΔG_{MIX}

Responsible for stabilizing the resulting phases of a solid solution, lowered Gibbs' free energy depends on the enhanced entropy of mixing, ΔS_{MIX} , and enthalpy of mixing, ΔH_{MIX} , as per Eq. 27 ([CALLEN, 1985](#)):

$$\Delta G_{MIX} = \Delta H_{ALLOY}^{MIX} - \tilde{T} \Delta S_{MIX} . \quad (27)$$

2.5.20 Entropy-enthalpy relation, Ω

The relation between enthalpy and entropy is employed to predict the phase formation, especially for HEAs, which is expressed by Eq. 28 ([GUO et al., 2011](#)):

$$\Omega = \frac{\tilde{T} \Delta S_{MIX}}{\left| \Delta H_{ALLOY}^{MIX} \right|} . \quad (28)$$

2.5.21 Chemical affinity, A

It enunciates that when the chemical affinity between two metals is high enough, the formation of a solid solution is disadvantaged, thus supporting the formation of intermetallic compounds or phase segregation ([GUO et al., 2011](#)). International Union of Pure and Applied Chemistry (IUPAC) defines affinity A (Eq. 29) as the negative contribution of partial derivative of Gibbs free energy G related to the extent of reaction ξ (measurement of the extent in which the reaction goes on) when temperature and pressure are held constant. Mathematically, affinity is given by:

$$A = - \left(\frac{\partial G}{\partial \xi} \right) \bigg|_{T, P} . \quad (29)$$

2.5.22 Structure

Represented by the second rule of Hume-Rothery, it states that metals with the same type of crystalline structure may form extensive series of solid solution ([GUO et al., 2011](#)).

3 POWDER METALLURGY (PM)

This chapter presents the main definitions and fundamentals about PM, the processes for metal powder obtainment, and some aspects in the mathematical modeling of powder.

3.1 Overall Process

Powder metallurgy (PM) is a manufacturing process in which a solid metal, alloy or ceramic in a form of dry particles is transformed into a component or a product of defined shape and presenting mechanical properties which sometimes allow it to serve as it is obtained via this process ([THÜMMLER; OBERACKER, 1993](#)).

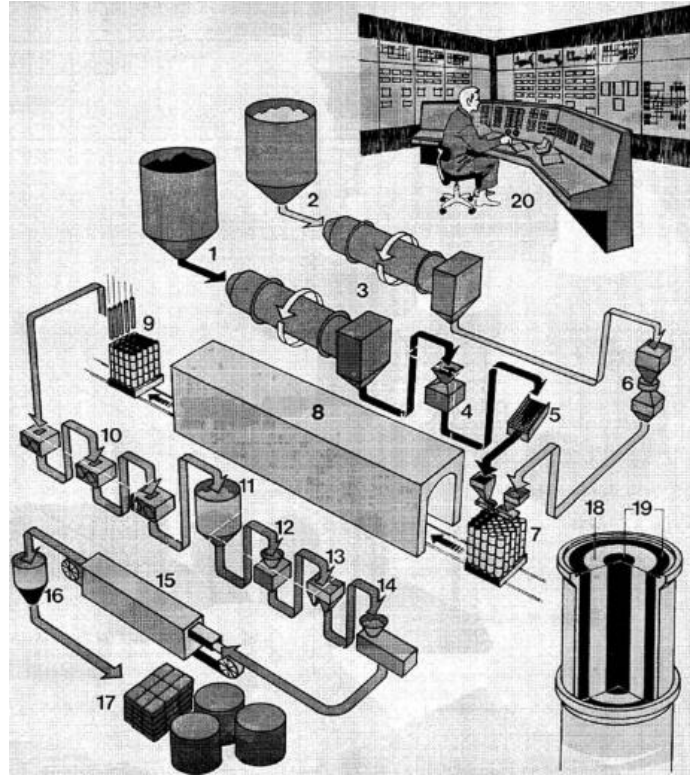
As an example of the entire process, [Fig. 10](#) shows the sponge iron process in ([HÖGANÄS, 2013](#)), starting from (1), which corresponds to a reduction mix of coke breeze and limestone put inside a storage tank. The reduction mix is dried (3), crushed (4), and screened (5), before being charged into ceramic tubes (7). In parallel (2), another tank is used to store the iron ore, which is dried (3), magnetically separated (6), and charged into the ceramic tubes (7), where details can be seen at regions (18) and (19) in [Fig. 10](#). Both mix reduction and iron ore pass through tunnel kilns (8) to be reduced at around 1200°C. The discharge (9) of the reduced semi-product is made and a coarse crushing (10) is conducted for posterior storage in silos (11). The particulate is subjected to a finer crushing (12) and a magnetic separation is performed (13), followed by grinding and screening (14), and annealing in a belting furnace at 900°C (15). The powder from the furnaces is homogenized (16) in lots, packed (17), and stored for shipment. The process can be monitored in a control room (20).

In order to be compared with similar ones, PM manufacturing process has the following advantages and limitations ([CHIAVERINI, 1992](#)):

- a) Elimination of almost all burrs.
- b) For pure materials, there is the possibility to implement a rigorous control in the product constitution.
- c) Possibility to obtain materials from the association of metals with non-metals.
- d) The design can provide a controlled porosity for self-lubricating purposes, for example.

- e) Opportunity to produce metals almost impossible to be obtained via conventional metallurgical processes, e.g. refractory metals.

Figure 10 - Sponge iron production from raw materials in Höganäs.



Source: [THÜMLER; OBERACKER, 1993.](#)

In order to be ready for further processing, additional treatments are commonly demanded. The scope of this post-processing is related to the geometrical parameters of the part, nature of the powder, metallurgical, and mechanical characteristics required. Powder conditioning is made possible by mixing additives to the powder mass. They possess the main functions of binding (enhancement of strength of the green compacts, which are defined as the compacted powder without sintering), plasticizing (provision of adequate conditions to promote the plasticization), and lubrication (ease of sliding between particles), predicting the subsequent manufacturing stages.

In the case of powder mixtures (the alloy is established when mixing powders from the different constituents, which is defined as a mixing), an insufficient homogenization may occur, and thus segregation during powder handling and

subsequent steps. Differently, the pre-alloyed powders, where every particle is constituted by the alloy (defined as a blending), establishes a homogeneous alloy. The last condition provides microstructural homogeneity and the avoidance of segregation.

One of the most important relations is that between surface forces and inertial forces, which increases with decreasing particle size. As ceramics and hard metals processing commonly use fine-grained powders, they present a high surface activity, which specific problems refer to: (a) possible uncontrolled agglomeration (less flowability); (b) adhesive wear between punch and die (may cause damage to tools).

After obtained, the mass of raw powders often presents a low compressibility (from e.g. atomization process, where particles are rapidly cooled), work hardening from mechanical comminution, residual interstitial impurities such as oxygen, carbon or nitrogen, and oxide layers formed during powder exposition. Therefore, the mass of powders often goes through heat treatments for size enlargement, annealing, degassing, chemical reduction, decarburization, etc.

The compaction stage aims at providing the necessary mechanical strength to the part, besides giving the final or almost final geometrical characteristics. In addition, the required contact between powder particles provides the appropriate density aiming at preparing for the next stages. There are two pressure assisted forming operations: cold and hot compaction methods. In cold pressing, there is the axial pressing (the punches axially load the mass powder), and the isostatic pressing (where the powder is sealed in an elastic mold and a hydrostatic pressure comes from a liquid). In hot pressing, the processing temperature is associated with the application of pressure. The main techniques are: (a) axial and isostatic hot pressing, (b) hot forging, and (c) hot extrusion ([THÜMMLER; OBERACKER, 1993](#)).

The initial stage of the compaction is the densification of the metal powder in a die considered as rigid compared to the mass to densify. This die has a certain cavity in which the powder is put under high pressure by two vertically moving punches, one from top and the other from bottom. This boundary condition implies the squeezing of the particles such that one of the main physical direct effects is the cold welding of their surfaces. Being successful, the ejection of the compacted mass takes place after the compaction. The green has to possess enough strength to be stable to posterior stages. A lubricant is often mixed to the powder before compaction to minimize the spent energy and lengthen the life span of the tooling.

The physical problem can be described in the following manner: as the densification increases, the particles are plastically deformed and increasingly strengthened by deformation (leveling up their yield strength). In microstructural terms, bigger powder particles establishes bridges around smaller ones. This causes an increase in their contact areas, which leads to decreasing shear stresses inside the particles. If the external pressure is held constant, as this process moves forward, if the rising yield strength reaches a level high enough to overcome the effect of the decreasing shearing stresses, then the densification ceases.

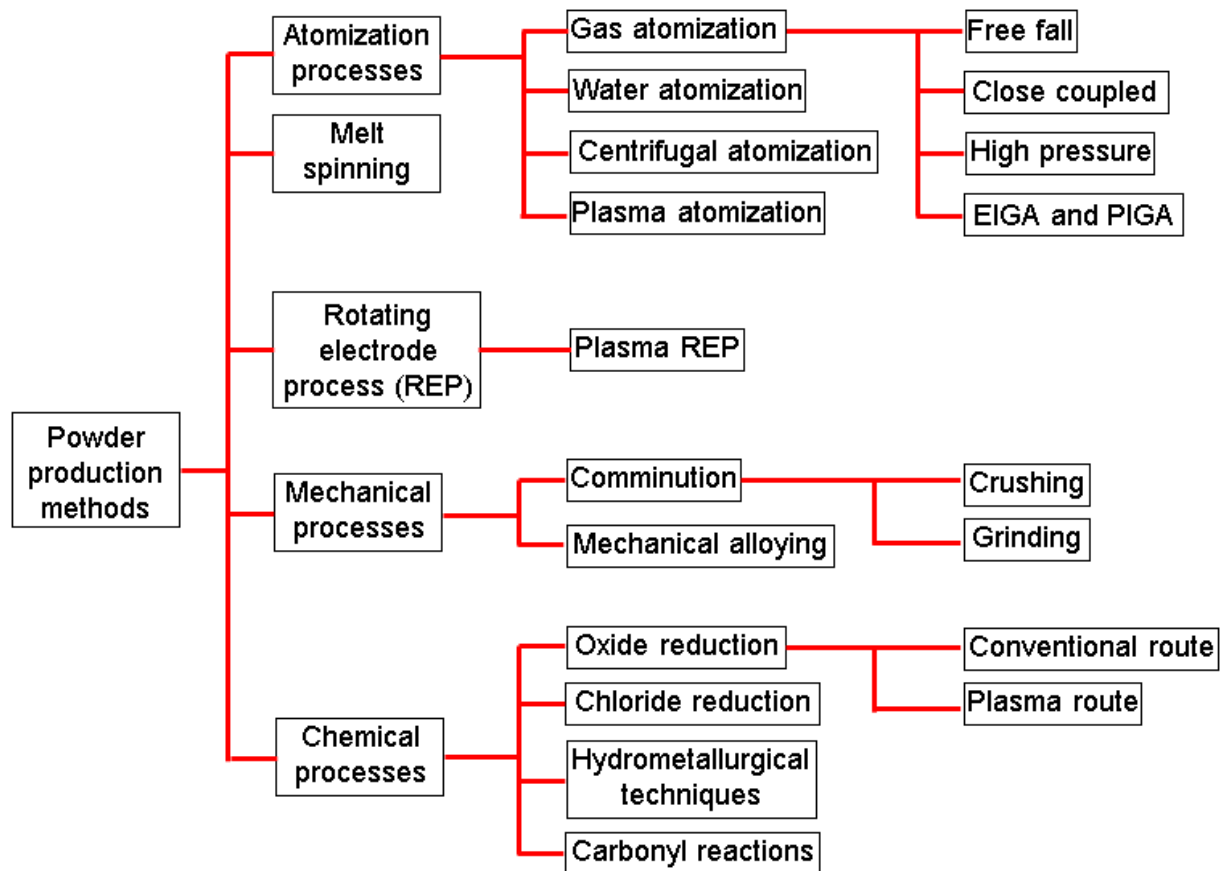
Densification process has the possibility to be effectively done by first rearranging the particles (commonly by vibrational methods) without change in their shapes aiming at obtaining a random dense packing. In this condition, the particles can be elastic-plastically deformed and work hardened or more fragmented in order to increase the compacting efficiency. This bridging process may be reached simply by load application and/or by lubrication of particles interfaces.

In order to describe the behavior of the powder mass quantitatively, there are several approaches, of which three are listed here. The first one considers the compacted powder mass as a homogeneous sample, extracting the relation between pressure and density, and radial pressure coefficient, for example. Another manner to deal with this physical situation is to apply the continuum mechanics and/or computer simulation, obtaining the response stresses, deformations, and density distribution. The last approach refers to the micromechanics of compaction, where the behavior of the individual particles under pressure is analyzed.

3.2 Processes for Obtaining Metal Powder (Highlighting the Mechanical)

The main categories of processes to obtain metal powder are described by the following three subsections. Theoretically, any material can be transformed into powder by one or more methods. The obtainment method mainly depends on the desired properties, raw material available, type of end application, and feasibility. [Fig. 11](#) shows the most common types of processes employed to obtain metal powder.

Figure 11 - Processes to obtain metal powder.



Source: adapted from [ANTONY; REDDY, 2003](#).

The remaining part of this subsection covers the mechanical processes to obtain metal powder. These types of size reduction of metal powder are performed in the solid state, in which the energy is partially converted from kinetic into elastic and plastic deformation, provoking mainly compression and shear stresses. For ductile metals, plastic deformation occurs before cracking and fracturing stages. The process effectiveness is dictated by the conversion of the kinetic energy into the fracture phenomenon. In addition to the elastic and plastic deformation energy types, the kinetic energy from the motion of the particles, and the generation of heat are the main causes of lost energy.

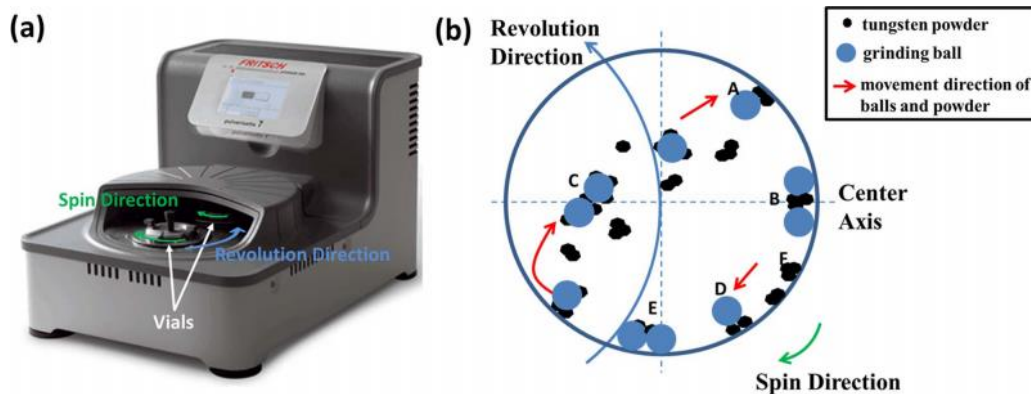
In the context of pure mechanical processes, the governing phenomena during size reduction of the solid masses are grounded on fracture mechanics principles: first, the nucleation of cracks; second, their propagation through the path of least energy spent; and the culmination of fracture, by which new surfaces are then formed. In terms of energy, the kinetic energy is turned into mechanical stresses in the material to be reduced in size. The predominant stresses (shear and compression) are mainly

caused by the system of impact and slow-acting multi-forces imposed to the masses. In general, the smaller the particle the higher the surface activity, thus corresponding to a higher probability of being re-welded. The efficiency of the so-called mechanical size-reduction processes is commonly low. It can be quantified by the energy needed to execute the process, which can be given by Eq. 30:

$$E = \gamma \Delta S, \quad (30)$$

where γ is the specific surface energy, and ΔS refers to the increase of specific surface. The planetary ball milling process applied to tungsten particles can be seen schematically in [Fig. 12a](#) and [Fig. 12b](#), where there are two vessels (each vessel shown schematically by part “b” of this figure).

Figure 12 - (a) Planetary ball milling machine; (b) ball milling schematic of vessel from top-view.

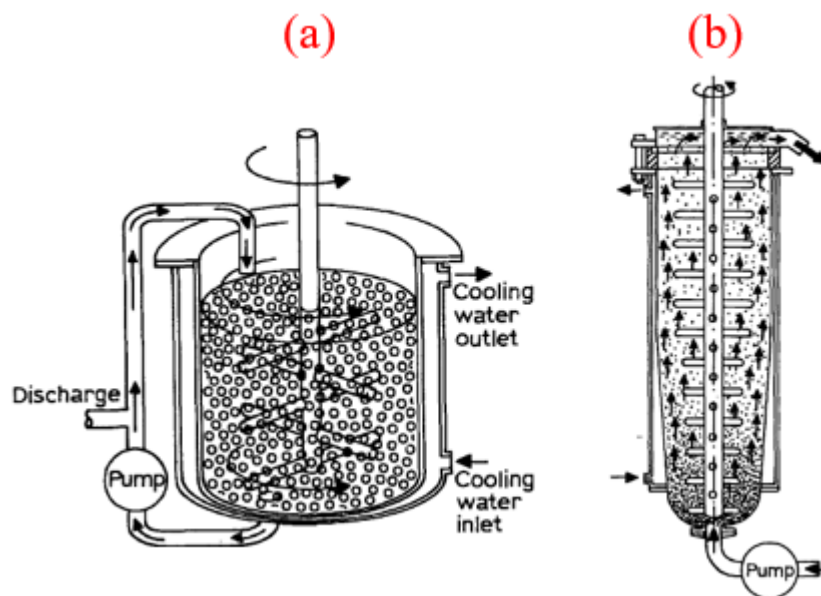


Source: [LIANG et al., 2017](#).

Blue and black balls represent grinding and powder objects, respectively. Blue and green arrows correspond to revolution and spin movements, respectively. The red arrows show the estimated path of the set of grind and powder balls, and describe the process of sliding along the vessel wall and the fall into the wall. Grinding balls should be in a condition of free fall over each other when the vessel rotates at a certain velocity, a situation that provides the optimum mode for the milling process to occur. In the case of the vibration milling process, the vessel is over springs, where frequency and amplitude are adjusted to induce the adequate vibration mode to the desired effect.

In the case of the attritor milling equipment, the set of balls and particles of the material to be reduced into powder is moved by a shaft with stirring arms inside a cylindrical vessel. This process can be conducted with some liquid aiming at providing the necessary conditions to run up and absorb part of the generated heat. The production can be handled in batches as in a batch attritor. However, in order to work on a continuous pace, periodic loading and unloading of the vessel are made in a continuous attritor. The loading is performed in the bottom of the vessel, and the unloading by the top of it. In addition, a cooling system is attached to the equipment because of the high degree of heating. [Fig. 13a](#), and [Fig. 13b](#) show (a) batch, and (b) continuous attritors, respectively, for wet grinding.

Figure 13 - (a) batch attritor for wet grinding; (b) continuous attritor for wet grinding.



Source: [THÜMLER; OBERACKER, 1993](#).

In terms of intensity, the conventional type is generally less intense than the attritor, which leads the former to take more time to accomplish the same service.

3.3 Mathematical Modeling of Powder Compact

In the context of PM, the mathematical modeling process is based on the analysis of a single particle surrounded by similar ones or by fluid (micro or nano level). The macro level is studied considering the powder compact as the body subjected to

the loading from the machinery involved in the compaction process. Based on this modeling, a software for compaction process was developed.

3.3.1 Compaction Pressure, Density, and Porosity

Defining the mass of the material as m , and its true volume as V_{tr} , its bulk volume as V_{bu} , and V_{th} as the theoretical volume, the true density, ρ_{tr} , bulk density, ρ_{bu} , and theoretical density, ρ_{th} , can be expressed respectively by Eq. 31, Eq. 32, and Eq. 33:

$$\rho_{tr} = \frac{m}{V_{tr}}, \quad (31)$$

$$\rho_{bu} = \frac{m}{V_{bu}}, \quad (32)$$

$$\rho_{th} = \frac{m}{V_{th}}. \quad (33)$$

Then, porosity is expressed by Eq. 34:

$$\phi = 1 - \frac{\rho_{bu}}{\rho_{th}}. \quad (34)$$

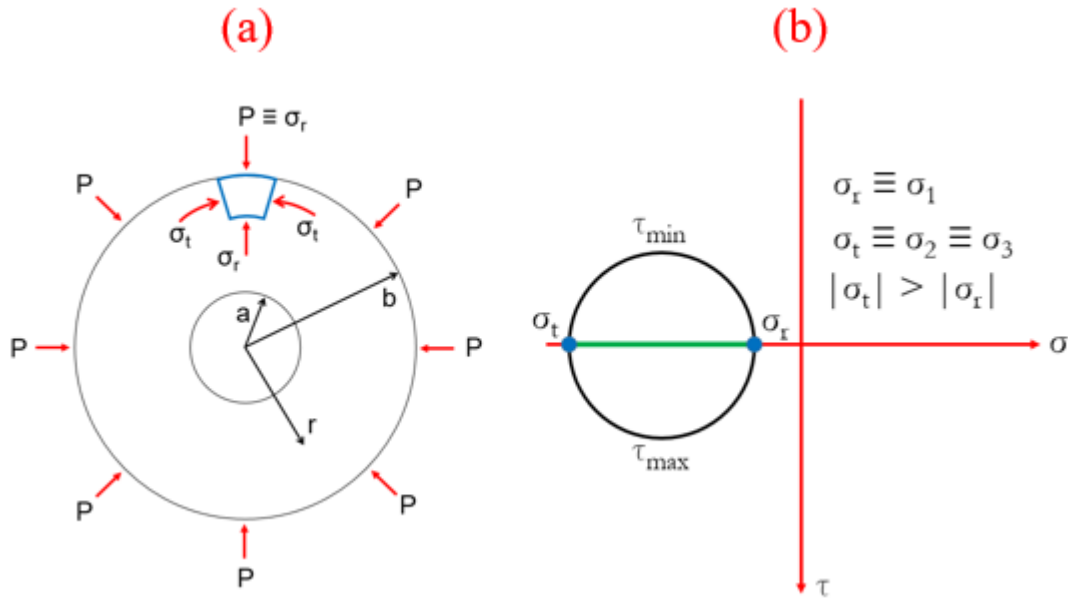
The mathematical expression for compaction pressure can be defined according to the method adopted. If the agent is a punch in a die compaction, the compaction pressure is the ratio between the force and the face area of compact while the force from an isostatic compression corresponds simply to the hydraulic medium pressure.

3.3.2 Loadings and Stresses

At the moment densification takes place, powder particles are squeezed together in an intensity such that interconnected pores turn into sparsely distributed smaller pores. This situation can be modeled for each pore and its adjacencies considering the approximation of a hollow sphere under hydrostatic outside pressure P (see [Fig. 14a](#)). In accordance with elasticity theory ([SADD, 2020](#)) and adopting

Tresca's failure criterion (in order to be conservative), plastic deformation occurs at the moment maximum shear stress at the external surface of the hollow sphere exceeds the shear yield strength, $\tau(b) = S_y / 2$. Here, S_y is the material yield strength; a, b , and r , are, respectively, the inner, outer, and a generic radius, such that $a \leq r \leq b$. Observing the stress state represented in [Fig. 14a](#), the radial and tangential pressures are compressing the infinitesimal element, which produce radial and tangential stresses, σ_r and σ_t , respectively. Alternatively, this element can be represented by its correspondent Mohr's circle, as is done in [Fig. 14b](#).

Figure 14 - (a) Infinitesimal element of a hollow sphere under external hydrostatic pressure representing a powder particle; (b) Mohr's circle of the stress state of (a).



Source: Own authorship, 2021.

Therefore, Eq. 35 expresses the yield function for the referred infinitesimal element under Tresca's failure criterion:

$$f(\sigma_t, \sigma_r) = \sigma_r(a, r, b, P) - \sigma_t(a, r, b, P) - S_y, \quad (35)$$

which implies that if the yield function results in a negative value, the entire hollow sphere domain is under elastic regime. This occurs because the outer surface is where the lowest radial and tangential stresses occur. Otherwise, the plastic flow

phenomenon starts and, depending on the mathematical model adopted for the material behavior under plastic flow, the material will harden or not.

Observing [Fig. 15](#) and calling on elasticity theory ([SADD, 2020](#)), one can analyze and extract the general governing expressions for the two types of involved stresses (Eq. 36, and Eq. 37):

$$\sigma_r(a, r, b, P) = \frac{Pa^3b^3}{(b^3 - a^3)r^3} - \frac{Pb^3}{(b^3 - a^3)}, \quad (36)$$

$$\sigma_t(a, r, b, P) = -\frac{Pb^3}{(b^3 - a^3)} - \frac{Pa^3b^3}{2(b^3 - a^3)r^3}. \quad (37)$$

The particularization to $r = b$ yields Eq. 38 and Eq. 39:

$$\sigma_r(a, r, b, P)|_{r=b} = -P, \quad (38)$$

$$\sigma_t(a, r, b, P)|_{r=b} = -P \frac{2b^3 + a^3}{2(b^3 - a^3)}. \quad (39)$$

The substitution of Eq. 38 and Eq. 39 into yield function (Eq. 35) results in Eq. 40, which is the minimum required load P to produce the plasticization of the outer surface of the particle. In other words, the external hydrostatic pressure to induce plastic deformation on the outer surface of the hollow sphere is higher the smaller the hole relative to the sphere volume.

$$P \geq \left(\frac{2}{3} \frac{b^3 - a^3}{a^3} \right) S_y. \quad (40)$$

Compared to that of the powder mass, the stiffness of the cylindrical die is much higher. This assumption simplifies the mathematical model a little when analyzing the situation of powder under compaction because it is not necessary to investigate die deformation. The axial pressure exerted upon the powder mass by the punch is not entirely transferred to radial pressure upon the die wall.

A mathematical model was suggested to interrelate the axial and radial pressures ([LONG, 1960](#)). This consists in a cylindrical plug of metal upon which an axial pressure is applied (upper and lower faces). In the elastic domain, under a triaxial

stress state, the following relation applies (Eq. 41), where ε_r is the radial strain; σ_r is the radial stress; σ_a is the axial stress; and E is the Young's modulus.

$$\varepsilon_r = \frac{(\sigma_r - \nu\sigma_r - \nu\sigma_a)}{E}. \quad (41)$$

Another assumption made at this point is that the friction is neglected because the lubrication is effective enough to cause considerable loss. As the die stiffness tends to infinite, the radial die expansion tends to zero ($\varepsilon_r = 0$). This implies in the following relation of the two stresses in the elastic domain (Eq. 42):

$$\sigma_r = \frac{\nu}{1-\nu} \sigma_a. \quad (42)$$

In view of this, the yield function is written in terms of the involved stresses and yield strength by means of Eq. 43. Therefore, in the plastic domain, the relation between axial and radial stresses is established as (Eq. 44).

$$f(\sigma_a, \sigma_r) = \sigma_a - \sigma_r - S_y, \quad (43)$$

$$\sigma_r = \sigma_a - S_y. \quad (44)$$

When the axial pressure from punches is released, the stresses do not return to zero, but to levels below the corresponding yield strength, as can be noted in last equation. Eq. 45 tries to model the elastic releasing by adding up a constant k :

$$\sigma_r = \frac{\nu}{1-\nu} \sigma_a + k. \quad (45)$$

In the process of releasing the axial pressure, the axial stress in the plug decreases and may, in some situations, become lower than the radial stress, the latter reaching the material's yield strength, in accordance with [LONG, 1960](#). In this situation, Eq. 46 describes the yield function, on which the relation between axial and radial stresses in plastic releasing can be based (Eq. 47):

$$f(\sigma_a, \sigma_r) = \sigma_r - \sigma_a - S_y, \quad (46)$$

$$\sigma_r = \sigma_a + S_y. \quad (47)$$

An enhancement from Long's model ([LONG, 1960](#)) was then proposed ([BOCKSTIEGEL, 1965](#)), which utilizes Long's model as the basis to include the frictional phenomenon. The upgrade added up the force at the die wall and stated that this force is approximately proportional to the radial pressure, P_r , caused by the axial pressure. Therefore, the axial stress is now a function of axial and radial pressures, in which the pressure increase is represented by the negative sign, and the pressure release by the positive one (Eq. 48):

$$\sigma_a = P_a \pm \mu P_r, \quad (48)$$

where μ is the frictional coefficient between the die wall and the powder mass, and P_r is the radial stress σ_r . Consequently, according to Bockstiegel's loading process model ([BOCKSTIEGEL, 1965](#)), elastic and plastic radial loadings are given, respectively, by Eq. 49 and Eq. 50:

$$(P_r)_e = \frac{P_a \nu}{1 - \nu - \mu \nu}, \quad (49)$$

$$(P_r)_p = \frac{P_a - S_y}{1 + \mu}. \quad (50)$$

In addition, the elastic and plastic radial loadings under releasing process are expressed by Eq. 51 and Eq. 52:

$$(P_r)_e = \frac{P_a \nu}{1 - \nu - \mu \nu} + k', \quad (51)$$

$$(P_r)_p = \frac{P_a + S_y}{1 - \mu}. \quad (52)$$

When dealing with a prismatic solid body under compressive axial loading, Saint Venant's principle can be verified in the axial stress distribution, where the highest magnitudes are found in the regions of direct load application. At a distance far enough

from these regions, the effect of load application decays and the stress assumes an almost homogeneous magnitude, the so-called mean stress. An analogous phenomenon occurs with powder mass. As the distance from the punch face increases, σ_a decreases. In contact with the punch faces, the powder mass experiences a higher axial pressure, resulting in an also higher densification. Consequently, the longer the body, the more heterogeneous the particles distribution. To model this phenomenon, a regular cylinder die with infinite stiffness is the boundary of a powder mass disc of radius r (die inner radius), with longitudinal axis denominated y , and infinitesimal length dy . On the upper face of this disc, the axial stress is $\sigma_a(y)$. Due to friction between the die wall and lateral surface of the disc, the axial stress on the bottom face of the disc is $\sigma_a(y + dy)$. Thus, Eq. 53 and Eq. 54, respectively, give the forces on the upper (F_u), and lower (F_l) surfaces of the disc:

$$F_u(r, y) = \pi r^2 \sigma_a(y), \quad (53)$$

$$F_l(r, y) = \pi r^2 \sigma_a(y + dy). \quad (54)$$

Thus, the frictional force, between the pair die-disc, F_f , is given by Eq. 55:

$$F_f(\mu, r, y) = \mu 2 \pi r dy \sigma_a(y). \quad (55)$$

From the equilibrium, Eq. 56 can be extracted, which results in Eq. 57.

$$F_u - F_l = F_f, \quad (56)$$

$$\pi r^2 [\sigma_a(y) - \sigma_a(y + dy)] = \mu 2 \pi r dy \sigma_a(y). \quad (57)$$

Rearranging Eq. 57, it yields Eq. 58, which is the axial stress distribution along the longitudinal axis of a powder mass cylinder:

$$\sigma_a(y) = \sigma_a(0) \exp\left(-2 \mu \frac{y}{r}\right). \quad (58)$$

As mentioned before, even after the loading is ceased, there is a remaining radial stress. Consequently, a significant magnitude of force is required to extract the

powder compact from the die. Thus, Eq. 59 expresses the force required to eject the compact mass from the die:

$$F_e(\mu, r, h, \sigma_{rr}) = \mu 2 \pi r h \sigma_{rr}(y), \quad (59)$$

where h is the compact powder height, $\sigma_{rr}(y)$ is the residual radial stress as a function of height y , such that $0 \leq y \leq h$.

After ejection from the die, the spring back effect comes from the natural elastic expansion of the compacted, which depends mainly on the powder properties, pressure, additives and lubricants used, and die characteristics. Its quantification observes the following formula (Eq. 60), which coincides with the definition of deformation, where L_i and L_f are, respectively, the initial and final transversal dimensions of the compacted powder:

$$S_b(\%) = \frac{L_f - L_i}{L_i}. \quad (60)$$

Therefore, the mathematical modeling presented herein covered the situations of loading, unloading, and ejection. It is based mainly on providing the load needed to provoke the plastic phenomenon in particles approximated by hollow spheres under external pressure.

4 SINTERING

This chapter explores the process that comes right after powder compaction, explaining the scope of sintering, the main phenomena involved, its stages, how its main variables behave throughout the process, the atmospheres involved, and the mathematical modeling of the phenomena.

4.1 Definitions, Phenomena, and Characteristics

The compacted powder is kept together mainly by adhesive forces, which magnitudes are smaller than those found when the green is sintered. The sintering process promotes bonding inside the crystal lattice. When the geometrical parameters involved allow the development of considerably large contact areas between the particles, green strength may reach high magnitudes. In terms of strength, the bonding established between atoms or ions are of the same order of magnitude as that of a regular lattice. Specifically for multicomponent alloys, although a liquid phase may exist, the solid solution itself has to assure a certain geometrical stability. During this process, fine powders tend to shrink, thus provoking densification. In the case of coarse powders, it is expected to have almost perfect dimensional stability.

Consequently, sintering can be defined as a thermally activated material transportation in a powder mass or a porous compact, implying a decrease in the specific surface by growing the contacts between the particles, shrinkage of void volumes (associated to the change of the pore geometry). Therefore, sintering is a heat treatment of a porous compact or a powder mass aiming at improving their desired properties. The process is often accompanied by chemical reactions and fluid-solid interaction. One of the key aspects of sintering is the shift from adhesive contacts or simply pure touching to solid-state bondings (at least two particles share surface atoms) ([THÜMMLER; OBERACKER, 1993](#)).

In what concerns temperature, it partially consists of heating of the already compacted powder mass at temperatures commonly in the range of 50 to 75% of the melting temperature of the material (if it is a pure component) or that of the lowest melting point constituent (if it is multicomponent). This temperature magnitude is held for a controlled and planned time, resulting in particle bonding, which implies an increase in density, hardness and mechanical strength ([CHIAVERINI, 1992](#)).

The decrease in system free energy is the leading macro phenomenon of the process, which results from the following circumstances: (a) reduction of specific surface area; (b) decrease in pore volume; (c) elimination of non-equilibrium lattice defect concentrations, and (d) non-equilibrium states (for multicomponent alloys). In this context, if the objective is to design products with high hardness and strength, the smaller the particle the better the result, as soon as particles with similar grain sizes and high density are achieved, and the oxidation is avoided.

Sintering is divided into three stages ([THÜMMLER; OBERACKER, 1993](#)):

- (a) The contacts between the particles are turned into sintered bridges (necks). Prior to sintering, micro planes are in contact. As soon as the process takes place, these contact planes are transformed into points of bonding.
- (b) After a certain evolution of neck growth, each particle starts to lose its identity. A new microstructure is then formed.
- (c) At high values of the theoretical density, most of the pore spaces are closed. The remaining pores become sphere-like. When gasses are trapped, additional densification becomes impossible (if the gasses are indifusible in the solid matrix).

In other words, in the beginning of the process, material is transported by diffusional process, influenced by the presence of crystalline defects at the lattice. The diffusional flow promotes the increase in the contact of the particles, verifying an initial bonding between them. The compact starts to present cohesion between particles, however without presenting significant dimensional changes. The higher the green density, the more efficient bonding is (mainly due to the higher contact area). Because of this initial bonding, a neck (which is commonly modeled based on the geometry of two connected spheres with a small volume enclosed by hyperboloidal surface tangent to the outer surface of the spheres) is then formed. A radius is formed at the ends of the neck (where a grain boundary arises between the two particles). The difference of curvatures between the section corresponding to the radius and the adjacent plane section implies a gradient of vacancies concentration between the neck surface of high curvature (which presents high vacancies concentration) and the adjacent plane surface (which has low vacancies concentration). In view of this, two types of diffusional flows may occur: surface and volume diffusions, which are responsible for rounding and spheroidization of irregular powders in a compact. When the atoms flow from the grain boundary to the neck, the vacancies flow in the opposite direction and

are thus eliminated at the grain boundary. This causes the approximation between the centers of the two particles, resulting in contraction.

The sintering of a multicomponent metal alloy may occur with or without a liquid phase. The process may also take place with or without solid solubility of the components. In the solid state, the potential to be sintered is affected by the responsive stresses, which result from: (a) phase inhomogeneities in the mixture; (b) short-range density range, caused by the compaction; (c) long-range density range, caused by agglomerates; (d) thermal expansion anisotropy (non-cubic phases); (e) thermal expansion mismatch between the existing phases.

The factors influencing the process are: (a) particle size, in which its reduction promotes a more effective sintering; (b) particle composition: impurities restrict the material transportation contrasting with disperse phases in matrix, which hampers the dislocation movements; (c) particle shape: if the shape favors the contact between the particles, the material transport has more interfaces to interact; (d) green density: an increase in the value of this parameter implies in a denser compacted; (e) time: the sintering degree depends on time mainly in the beginning of the process; (f) particle structure: a fine internal structure and crystalline imperfections imply in a more effective sintering due to facilitating diffusional process; (g) temperature: the temperature increase implies in a higher velocity in the process.

The atmospheres involved in sintering are planned to control the chemical reactions, eliminate impurities, provide convectional heat transfer, eliminate admixtures, impede evaporation of the elements, etc. This is even more relevant when dealing with mixes of powders because two main events simultaneously occur: the alloying and the bonding process itself. The relative proportions of the involved components control the nature of the atmosphere, e.g. if it is decarburizing, carburizing, neutral, oxidizing, or reducing.

4.2 Liquid Phase Sintering

In the branch of liquid phase sintering, the main objective is to maximize the density, implying a reduction of porosity. Sintering in the presence of a liquid commonly addresses three stages ([CHIAVERINI, 1992](#)): (a) rearrangement: large particle movement in the liquid phase, which promotes the dislocation of the particles to densify; (b) dissolution and precipitation: it takes place only if the solid is soluble in the

liquid; (c) coalescence: a fast growing of solid grains may occur in the regions where there is no liquid phases.

Therefore, the influencing factors are listed and described: (a) particle size, in which the lower its size the more effective is the sintering; (b) particle composition: material transportation is restricted by impurities, which contrasts with disperse phases in matrix (that hampers the dislocation movements); (c) particle shape: the material transported has more interfaces to interact if the shape favors the contact between the particles; (d) green density: a higher green density implies in a denser compacted; (e) time: this factor is most significant in the beginning of the process; (f) particle structure: diffusional process is facilitated by a fine internal structure and crystalline imperfections; (g) temperature: a higher velocity in the process can be achieved by a higher temperature.

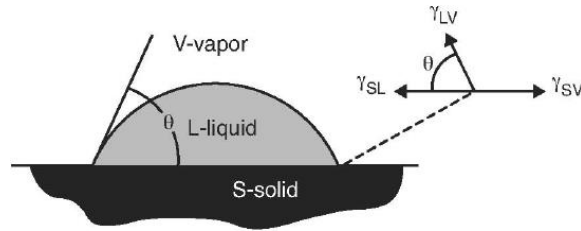
The atmospheres produced in sintering are intended to regulate the chemical reactions, remove impurities, supply convectional heat transfer, remove admixtures, block evaporation of the elements, etc. In the case of mixes of powders, two main events concomitantly occur: the bonding and the alloying processes. The molar fractions of the involved components regulate the atmosphere, i.e. if it is reducing, neutral, oxidizing, carburizing, or decarburizing.

The stress generation by wetting liquids induces the agglomeration of some regions of the powder because of the capillary stresses. This is mathematically modeled by using the wetting angle or contact angle, θ , which is originated at the intersection of vapor, liquid, and solid phases. The contact angle is defined by the horizontal equilibrium of surface energies (see Fig. 15). The contact angle is measured perpendicularly to the gravity vector. The resulting horizontal solution is expressed by Eq. 61:

$$\gamma_{SV} = \gamma_{SL} + \gamma_{LV} \cos(\theta), \quad (61)$$

where indices SV , SL , and LV correspond to solid-vapor, solid-liquid, and liquid-vapor surface energies, respectively.

Figure 15 - A droplet standing on a surface presenting a pictorial definition of the contact angle.

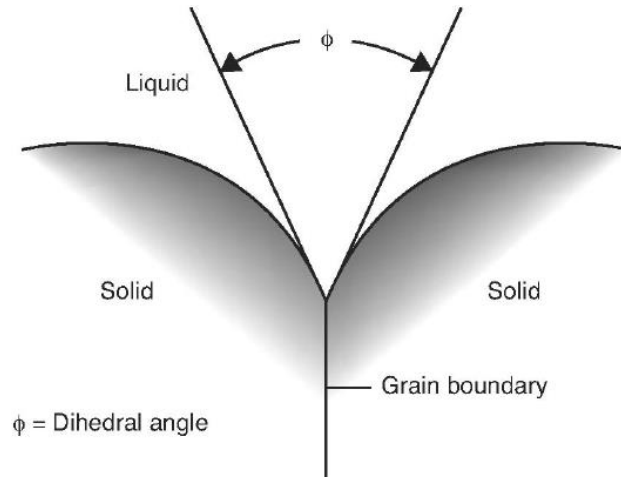


Source: [FANG, 2010](#).

By performing a thermodynamic balance, the dihedral angle (ϕ) (as per Fig. 16) is generated by a grain boundary where it intersects with another solid, pore, or liquid during sintering. Eq. 62 introduces the interrelation with solid-solid and solid-liquid surface energies, respectively, γ_{SS} , and γ_{SL} :

$$\phi = 2 \arccos \left(\frac{\gamma_{SS}}{2 \gamma_{SL}} \right). \quad (62)$$

Figure 16 - Two solid particles interfacing to form the dihedral angle.



Source: [FANG, 2010](#).

When the solid has enough solubility, a relevant non-equilibrium transient is built when the liquid expands and enters the solid interfaces. The liquid flow throughout the pores dictates the swelling phenomenon. The depth of liquid penetration, X , depends on the holding time, t , via Eq. 63:

$$X = \left(\frac{d_p \gamma_{LV} t \cos(\theta)}{4 \eta} \right)^{\frac{1}{2}}, \quad (63)$$

where η is the liquid viscosity, γ_{LV} is the liquid-vapor surface energy, and d_p is the pore size.

The surface stress is due to a non-equilibrium vacancy concentration. Therefore, Eq. 64 models the vacancy concentration under a curved surface as a function of the curvature:

$$C = C_0 \left[1 - \frac{\gamma \Omega}{K_B T} \left(\frac{1}{R_1} + \frac{1}{R_2} \right) \right], \quad (64)$$

where γ is the surface energy (solid-vapor or solid-liquid), K_B represents the Boltzmann's constant, C_0 is the vacancy concentration corresponding to a flat surface at the same absolute temperature T (equilibrium), and Ω is the atomic volume. Therefore, if the atomic flow is toward from convex to concave surfaces, then the atoms go from regions of low concentration to regions of high concentration of vacancies. Nevertheless, vacancy formation is necessary, but not sufficient to produce atomic motion by volume diffusion. The energy to break the atom bonding is also required. The relative number of active atoms N_A is obtained via Arrhenius equation by a comparison with the total number of atoms N_0 (Eq. 65):

$$N_A = N_0 \exp \left(-\frac{Q_B + Q_N}{R T} \right), \quad (65)$$

in which Q_B and Q_N are, respectively, the energies required to break the bonds, and responsible to vacancy formation. Thus, $Q_B + Q_N$ is denominated activation energy.

4.3 Mathematical Modeling of Sintering

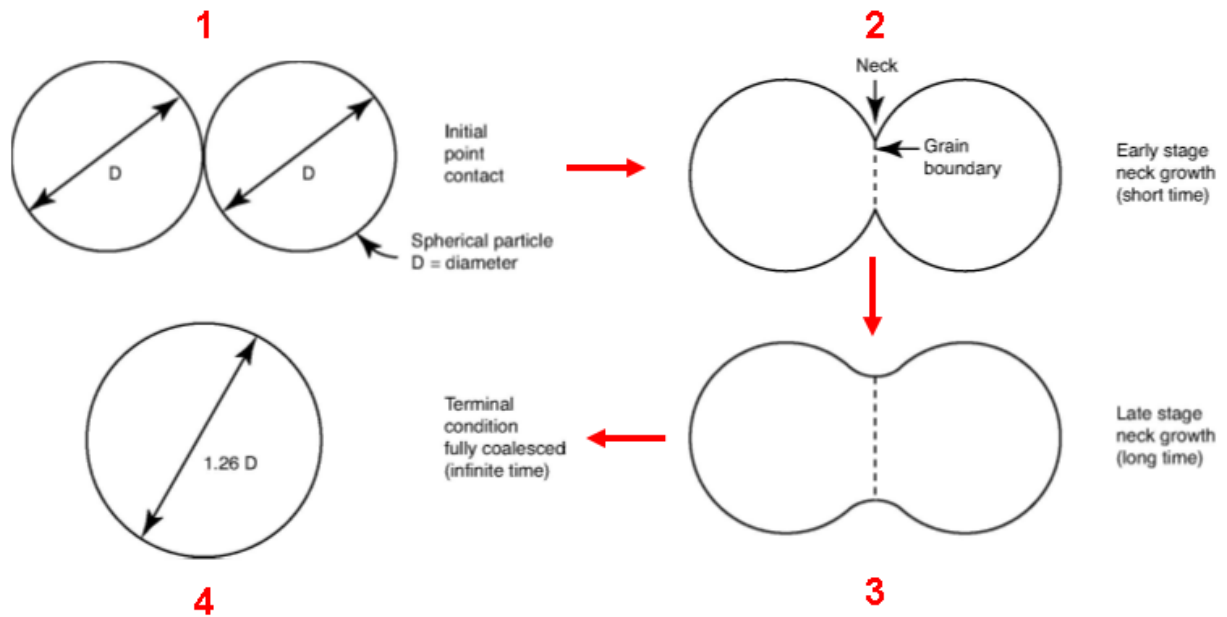
Sintering process is composed of the three already described stages (see [Section 4.1](#)), being the former referred to a localized bonding (when there is the neck formation), and the latter corresponding to the rounding and shrinkage of the pores

(see [Fig. 17](#)). The governing quantity of this process is the free surface energy of the particles agglomerate. In the bonding process, there is the transportation of material from the particle nucleus through its thickness until it reaches areas of contact with other particles. Rounding and shrinkage of existing pores demand mass flow from the densest volume to the pore surface, in addition to from softer to sharper corners of the pore surface. The preponderant mechanism of sintering is the volume diffusion ([HÖGÄNAS, 2013](#)).

A dimensionless parameter, k_s , expressed by Eq. 66 in terms of percentage, usually represents how the surface area quantitatively behaves related to the initial surface area, S_0 , where ΔS is the change in surface area:

$$k_s = \frac{\Delta S}{S_0} 100. \quad (66)$$

Figure 17 - Two-sphere sintering model, from initial contact to full coalescence.



Source: Adapted from [FANG, 2010](#).

The linear shrinkage phenomenon can be mathematically defined in a similar way as that introduced by the spring back effect, in the section dedicated to the mathematical modeling of powder metallurgy. Thus, linear shrinkage, S_k , is defined as the compact length change divided by the initial dimension ($\Delta L / L_0$), as per Eq. 67:

$$S_k = \frac{\Delta L}{L_0}. \quad (67)$$

This phenomenon causes the densification from the initial density, ρ_i , to the final density, ρ_f , obeying the following expression (Eq. 68):

$$\rho_f = \frac{\rho_i}{(1 - S_k)^3}, \quad (68)$$

where ρ_i , and ρ_f obeys the following expressions (Eq. 69, and Eq. 70):

$$\rho_f = \frac{m_f}{V_f}, \quad (69)$$

where ρ_i is obtained by the ratio of the green mass m_i and the green volume V_i (see Eq. 70):

$$\rho_i = \frac{m_i}{V_i}. \quad (70)$$

Densification can also be defined in terms of these densities (Eq. 71):

$$\Psi(\%) = \frac{\rho_f - \rho_i}{\rho_i} 100. \quad (71)$$

Since smaller grains tend to cluster, the grain structure obtained by sintering is not random. Pores tend to sit on grain faces during grain growth, while during shrinkage pores tend to be on the corners.

5 TESTING

This section includes the processes to quantify some required properties of the EHMMAs, which involves hardness testing, and scanning electron microscopy (SEM).

5.1 Hardness testing

The hardness testing comprises the general concepts and the static method Vickers.

5.1.1 General concepts of hardness

Hardness is sometimes referred to resistance or durability of a part, but the direct definition is the ability of a part to counter the penetration of a standardized body. Furthermore, the quantification of hardness depends also on the speed with which the object is penetrated ([HERRMANN, 2011](#)). Therefore, Eq. 72 gives the resistance to penetration deformation (hardness):

$$H = \frac{F}{A}, \quad (72)$$

where F is the testing load, and A is the area of the indentation measured on the upper surface of the sample. Thus, in order to define a hardness testing method, some specifications should be made: (a) the governing equation of the hardness value; (b) the form of the indenter; (c) the material of the indenter; (d) the force-time regime.

The chemical bonding forces play an important role because they are responsible for the crystal structure. In addition, in metals, there are relationships between their hardnesses and their electric and magnetic properties.

Commonly, the hardness of metal alloys are higher than the hardness of each constituent element. This is explained by the magnitude of bonding forces.

The hardness is also dependent on the grain size. The larger the grain size, the smaller the hardness, governed by a non-linear behavior.

In static hardness measurement methods, the hardness is a function of the contact pressure, p_m , which is proportional to the yield strength S_y of the material being

tested, and also depends on constant C (dependent on the material, type of indenter, and testing conditions) (Eq. 73):

$$H = p_m \approx C S_y. \quad (73)$$

In the case of metals presenting a large E / S_y ratio, C tends to the value of 2.8. The last equation has been divided into three domains ([TABOR, 1951](#)):

- (a) If $p_m < 1.1 S_y$, the behavior is elastic;
- (b) If $Y < p_m < C S_y$, the subsurface plastic deformation is delimited by adjacent elastic material;
- (c) If $p_m = C S_y$, the plastic region reaches the surface, and p_m does not increase with increasing testing load.

When in elastic phase, the phenomenon can be described by the Hertz contact relation, in which the contact radius is given by Eq. 74:

$$a = \sqrt[3]{\frac{3 F R}{4 E_R}}, \quad (74)$$

where R is the radius of the indenter, F is the testing load, and E_R is the reduced modulus. This last variable represents the interaction between the moduli of the part to be tested, E_p , and the one from the indenter, E_I , given by Eq. 75:

$$\frac{1}{E_R} = \frac{1 - \nu_p^2}{E_p} + \frac{1 - \nu_I^2}{E_I}, \quad (75)$$

where ν_p , and ν_I are Poisson's ratios of the part and of the indenter, respectively. In view of this, the mean contact pressure is expressed by Eq. 76:

$$p_m = \frac{F}{\pi a^2}, \quad (76)$$

and the stress-strain relation is given by Eq. 77:

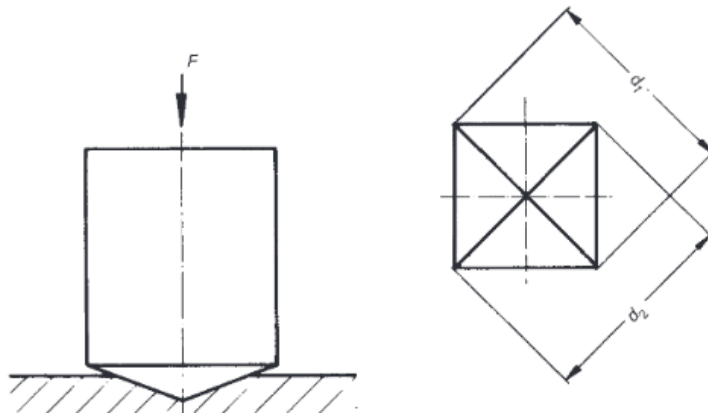
$$p_m = \left(\frac{4a}{3\pi R} \right) E_R, \quad (77)$$

where a/R ratio is the strain of penetration. Among the static methods already established, in this thesis all the hardness tests are conducted using Vickers procedure, which encompasses ASTM E384, ASTM E92, and ISO 6507.

5.1.2 Vickers hardness

Vickers hardness testing is indicated for testing almost all metals. This procedure applies a diamond pyramid as the one shown in [Fig. 18](#).

Figure 18 - Vickers measurement.



Source: [WOLFENDEN; WEILER, 1990](#).

The advantage of this indenter follows the law of proportional resistances, i.e. the testing load and indentation surface are proportional to each other (the hardness magnitude is independent of the applied load). The angle between each pair of opposite faces is 136° . Vickers hardness is calculated as in Eq. 78, where F is the testing load, A is the area of the indentation measured on the upper surface of the sample (calculated from the mean value d of its diagonals d_1 , and d_2).

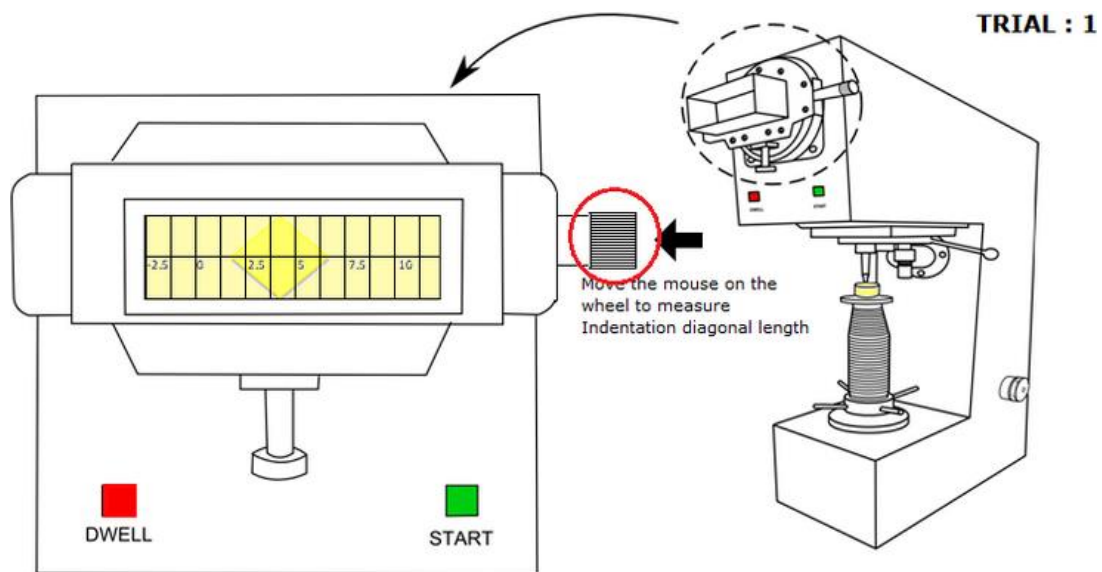
$$H_v = \frac{0.102 F}{A}, \quad (78)$$

which may be written as Eq. 79:

$$H_v = \frac{0.102F}{d^2} = \frac{0.1891F}{d^2 \cdot 2 \sin(68^\circ)} \quad (79)$$

[Fig. 19](#) shows the schematic of a Vickers hardness-testing machine, highlighting the visor from which it is possible to observe and measure the indentation.

Figure 19 - Vickers measurement.

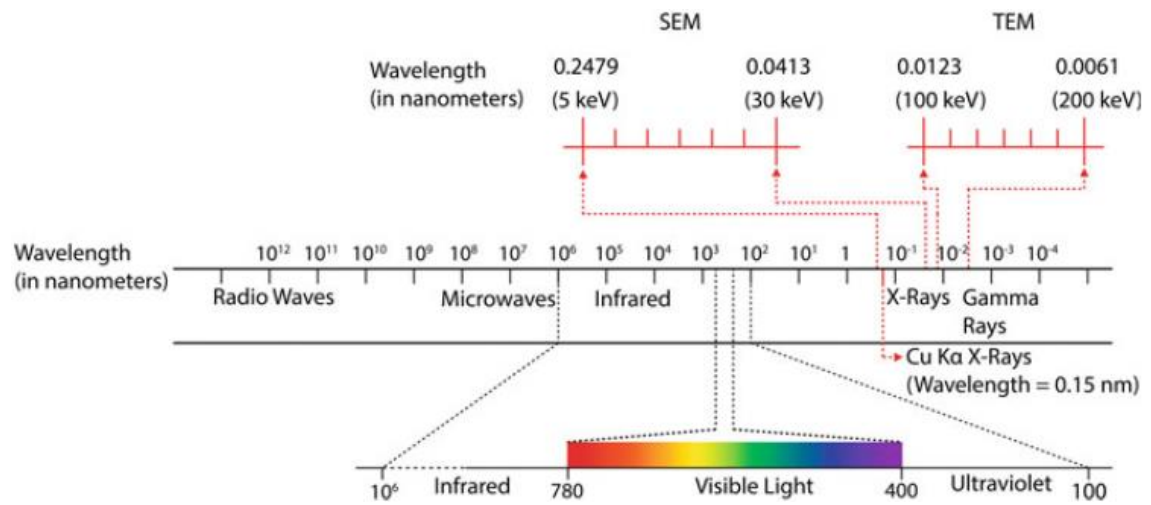


Source: [VIRTUAL LABS, 2022](#).

5.2 Scanning electron microscopy (SEM)

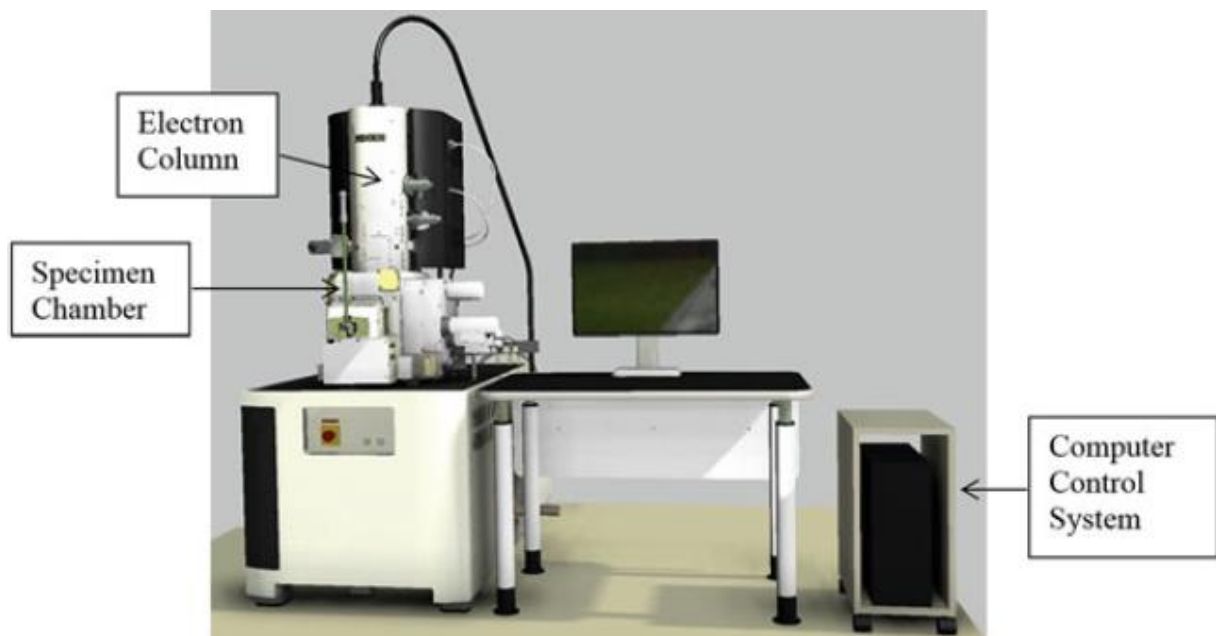
This technique enlarges small objects by an electron beam of high energy on the sample surface. Due to its smaller wavelength, electrons can resolve relatively fine details, up to less than one nanometer. Additionally, the incidence of electron beams on the sample emits x-rays with unique energy, which is the input to detect the material composition (material characterization of the surface composition). [Fig. 20](#) emphasizes the electromagnetic spectrum of the light, transmission electron microscopy (TEM), and SEM in terms of their wavelength and resolution. [Fig. 21](#) shows the macro subsystems of a common SEM: the computer control system, the specimen chamber, and the electron column.

Figure 20 - Electromagnetic spectrum of light, TEM, and SEM.



Source: [UL-HAMID, 2018](#).

Figure 21 - SEM equipment.



Source: [UL-HAMID, 2018](#).

The electron beam passes through electromagnetic lenses in the electron column (which is under vacuum) in order to focus into a small diameter (to penetrate into the surface of the sample, which is located in the specimen chamber). The

computer control system manages all the processes with the virtual interface of a program.

The instrumentation attached to SEM may include energy-dispersive x-ray spectrometer (EDS), backscattered electron (BSE) detector, secondary detectors, low vacuum detector, etc.

The EDS detector is responsible for providing qualitative and quantitative microchemical analysis. SEM with microchemical analysis by EDS technique is commonly used to identify phases in a material. Part of the generated x-rays are absorbed by the material or in the EDS detector window.

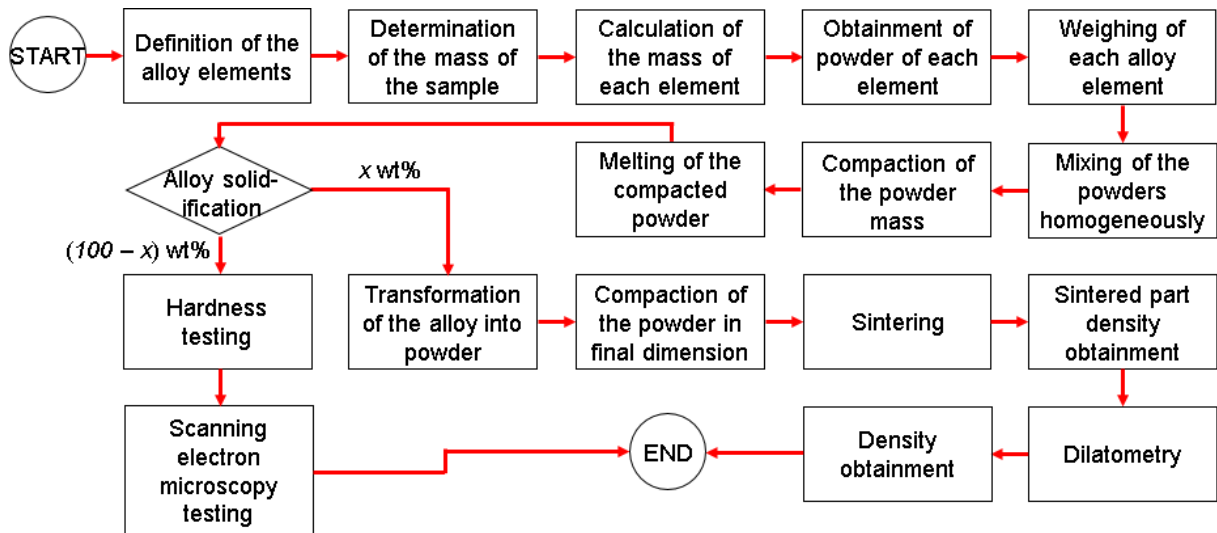
In what refers to surface contamination, in case of over exposure of the specimen to the scanning, the image can be less sharpened and dotted with a dark rectangular smudge. This is due to carbon deposition, which comes from the contact between the electron beam and residual gas molecules present in the sample surface. The referred gas is commonly a volatile hydrocarbon, in which molecules are ionized by the electron beam and transformed into a nonvolatile carbon. Although vacuum is intended to be produced in the chamber of the SEM, residual gas molecules are always present and induced by grease, back pressure from pump, organic material (preparing specimen), and outgassing.

6 MATERIAL AND METHODS

This chapter describes the material and methods applied in the work of this thesis. The chapter is divided into two branches: (a) computational: the softwares created and what they are capable of doing, which can be seen in [section 6.1](#), [section 6.4](#), and [section 6.6](#); (b) experimental: the description of the experiments performed and how they are sequenced, which is detailed in [section 6.2](#), [section 6.3](#), [section 6.5](#), and [section 6.7](#). The scheme of the experimental part of this thesis is shown in the following flowchart ([Fig. 22](#)), where x is the weight percentage of the alloy produced.

It is important to highlight that all the experiments were conducted from March 2021 to May 2022 at Thermophysical Laboratory (University of Sorocaba, UNISO). Besides that, all the softwares were developed on an Acer Aspire E15, with “Intel core i5” processor of the author’s property, using Microsoft Visual Basic 6.0®, emulated in Microsoft Visual Studio Ultimate 10.0®, from March 2021 to Dec 2022.

Figure 22 - Flowchart of the experimental part of this thesis.



Source: own authorship, 2023.

6.1 Software Developed for EHMMAs Design (DIAMOY 1.0 updated to DIAMOY 2.0)

A software denominated DIAMOY 1.0 was first developed in order to predict the feasibility of the EHMMAs with ten descriptive parameters and four statuses related to

some of these parameters. Posteriorly, it was updated to DIAMOY 2.0. The improved version is dotted with twenty parameters and five statuses related to some of the involved parameters (for further details related to the descriptive parameters and statuses, see [Section 2.5](#)).

As the research progresses, different parameters and statuses are being presented as relevant. This drives to a software enhancement to include the missing parameters. This enhancement was implemented to achieve a more accurate prediction of the alloy feasibility. Therefore, aiming at improving DIAMOY 1.0 accuracy, which has ten parameters and four criteria to design an EHMMA, DIAMOY 2.0 is cited here, with a set of twenty parameters and five criteria to foresee the alloys feasibility. In addition, both Diamoy 1.0 and Diamoy 2.0 output the individual mass of the chemical elements involved in the design of metal alloys. DIAMOY 2.0 was also coded in Microsoft Visual Studio 10.0® via emulation of Microsoft Visual Basic 6.0® ambient.

The purpose of the software is to evaluate the alloy design process to form a stable solid solution. In addition to function as an embedded checklist, it aims at accelerating the alloy design process. In spite of applying all these parameters and statuses, there is no guarantee to obtain a stable solid solution if all these items are fulfilled. This is explained by: (a) even applying the parametric approach, there are another group of parameters to be contemplated and others yet not discovered; and (b) there is a risk of not examining some aspects of evaluation because there are other approaches which are not part of the calculation scope.

[Fig. 23](#) presents the blank screen of DIAMOY 2.0, i.e. before filling in the fields to design the intended alloy. Brief instruction lines precede buttons, a drop-down box, and text boxes, all composing the software interface. The equivalent sequence of programming sentences produces the graphical user interface presented. The user interacts with the software by a unique screen, which intends to ease the input and the output processes. The input process includes the selection from a dropdown list, clicking on checkboxes, and typing in some data in the required fields.

Figure 23 - Empty interface of “DIAMOY 2.0”.

DIAMOY 2.0

INPUT:

Product mass: g

Alloy elements:

- ☐ Al
- ☐ B
- ☐ C
- ☐ Co
- ☐ Cr
- ☐ Cu
- ☐ Fe
- ☐ Hf
- ☐ Mn
- ☐ Mo
- ☐ N
- ☐ Nb
- ☐ Ni
- ☐ Sn
- ☐ Ta
- ☐ Ti
- ☐ V
- ☐ W
- ☐ Zr

Equimolar?

Fraction (if it is not equimolar):

Restart!

Calculate!

OUTPUT:

Atomic radii difference, Delta_r (%):	
Status of atomic radii difference:	
Mean atomic radius (pm):	
Polydispersion of atomic radii, delta:	
Status of polydispersion of atomic radii:	
Chromium Equivalent (%):	
Topological discrepancy, gamma:	
Status of topological discrepancy:	
Mean VEC:	
Status of mean VEC:	
Standard deviation of VEC:	
Mean Electronegativity (Pauling):	
Electronegativity difference (Pauling):	
Mean melting point (°C):	
Standard deviation of melting point (°C):	
Mean density (g / cm ³):	
Standard deviation of density (g / cm ³):	
Mean bulk modulus (GPa):	
Standard deviation of bulk modulus (GPa):	
Entropy of mixing (J / mol K):	
Status of entropy of mixing:	
Average mixing enthalpy (kJ / mol):	
Standard deviation of mixing enthalpy (kJ / mol):	
Lowered Gibbs' free energy (kJ / mol):	
Entropy-enthalpy relation:	

Source: own authorship, 2022.

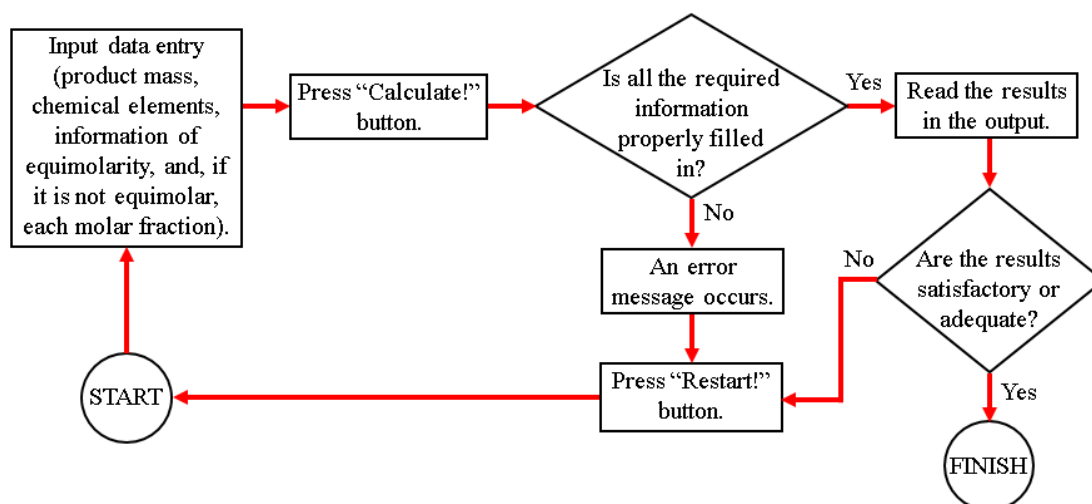
It is possible to highlight two main sections in the software interface: “input” (located at the left in the program window), and “output” (located at the right in the same window). There are four regions in the input section. The first region, “Product mass:”, is where the total mass (in grams) of the alloy should be filled in. The second one, “Alloy elements:”, the alloy elements should be selected through the checkboxes corresponding to the chemical elements involved. In the third, the field “Equimolar?” may be checked with “yes” or “no”. If “yes” option is chosen from the drop-down list, the fourth region “Fraction (if it is not equimolar)” should be blank; otherwise, the region “Fraction (if it is not equimolar)” should be filled in with the molar fraction corresponding to the alloy elements involved in the design.

After all the “input” data is filled in, the required action is to press the blue button “Calculate!”. Therefore, in the second section, denominated “output”, the following results are printed on the same window: (a) the individual mass (in grams) of the elements involved in the alloy; (b) the twenty parameters and the five criteria statuses described in [Section 2.5](#) of this thesis. If missing, exceeding, or incorrect detectable input data have been entered into the software after the blue button “Calculate!” was

pressed, it is necessary to press the red button “Restart!”. The software restarts with all the fields in the blank form.

A workflow with the main instructions to be followed throughout the filling in process is presented in [Fig. 24](#). In this flowchart, the user fills in only the required information and picks out the adequate options in the input data region. Thereafter, it is required to press the blue button “Calculate!”. An error message appears with some instructions to fix it if one or more of the required fields is not adequately selected or not filled in accordingly. Consequently, the “Restart!” red button should be pressed to refill the input fields properly. Contrarily, if the software is properly filled in, it will provide the corresponding output values. In the case these results are adequate to develop the required alloy, then the process comes to its end. If the values are not applicable to the objectives set, another prediction can be started by pressing the “Restart!” button.

Figure 24 - DIAMOY 2.0 workflow.



Source: own authorship, 2022.

6.2 Obtainment of Powder Mix

The process to obtain powder mix goes from defining the criteria to select the alloy elements to the mixing of those elements.

6.2.1 Definition of the parameters to select the elements to compose the alloy

The alloy design process is based on the theoretical characteristics of the pure metals involved, on the relation two by two, and in the context of the entire alloy. The multiparametric and multicriteria approach was the selected one to predict the behavior

of the metal alloy to be designed. Among the twenty-two parameters shown here, twenty of them were effectively available to be applied in the design. The molar fraction of the constituents and the total mass of the alloy are the input data to predict a solid solution. This stage is conducted by using the software DIAMOY 2.0. The program outputs the calculated parameters and the criteria with which the behavior of the proposed alloy can be evaluated. The information about the chemical elements involved in this thesis were extracted from ([DEAN, 1999](#)), and ([TAKEUCHI; INOUE, 2010](#)). [Tab. 1](#) presents the nomenclature corresponding to each alloy addressed herein.

Table 1 - Nomenclature of the alloys addressed in this thesis.

Alloy	Nomenclature
L4	$\text{Cr}_3\text{FeMoNbTaTiV}$
L4Cu	$\text{Cr}_3\text{FeMoNbTaTiV} + 3 \text{ wt.\% Cu}$
L4.1	$\text{AlCr}_3\text{FeMoNbTiV}$
L5	$\text{CrFe}_3\text{MoNbTaTiV}$
L5Cu	$\text{CrFe}_3\text{MoNbTaTiV} + 3 \text{ wt.\% Cu}$
L5.1	$\text{AlCrFe}_3\text{MoNbTiV}$
L5.1Cu	$\text{AlCrFe}_3\text{MoNbTiV} + 3 \text{ wt.\% Cu}$
L7	AlCrFeNbTiW
FN22	$\text{AlCrCuFe}_2\text{MoNb}_2\text{Ti}$

Source: own authorship, 2023.

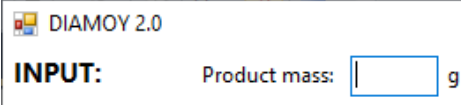
6.2.2 Determination of the mass enough to manufacture the product or sample

An input in the EHMMAs design (see [Fig. 25](#)), the mass to manufacture the product or sample is determined based on the resulting density (calculated in DIAMOY 1.0 or 2.0), on the volume that the product should occupy, or simply on an estimation. Another possibility is to work with a previously defined mass to provide significance to the product or sample to be analyzed, which was adopted in this thesis. Besides that, as there are losses throughout process stages, a slightly larger mass (5%

approximately) should be prepared. Among others, the lost amount depends on the following items:

- (a) type(s) of process(es) to obtain the powder;
- (b) elements involved in the alloy;
- (c) type(s) of process(es) to homogenize the alloy powder;
- (d) ambient moisture;
- (e) operator's ability;
- (f) powder granulation;

Figure 25 - Input field of product mass (in grams) in DIAMOY 2.0.



The screenshot shows a software window titled "DIAMOY 2.0". Inside, there is a section labeled "INPUT:". To the right of "INPUT:", the text "Product mass:" is followed by a rectangular input box and the unit "g".

Source: own authorship, 2022.

[Tab. 2](#) lists the masses of each alloy sample for this thesis. The main reason for masses of this magnitude relies on the limited capacity of the plasma furnace. For example, if more mass is needed, other samples should be prepared separately.

Table 2 - Masses of the samples of the alloys obtained in this thesis.

Alloy	Mass (g)
L4	20
L4Cu	30
L4.1	40
L5	20
L5Cu	30
L5.1	20
L5.1Cu	30
L7	40
FN22	30

Source: own authorship, 2023.

6.2.3 Calculation of the mass of each alloy element

In [Fig. 26](#), which refers to DIAMOY 2.0 input screen, the mass of each metal alloy element is inputted in molar fraction data (the metal alloy element mass also depends on the mass of the product or sample) and it is given in grams in the output. When adding up the mass contribution of each alloying element at the input or the output, the result should always be the total mass of the product or sample. Both DIAMOY 1.0 and DIAMOY 2.0 can perform this stage. If it is an equimolar alloy, then the software assumes an equal fraction for each element.

Figure 26 - Molar fraction input in “DIAMOY 2.0”.

Product mass: g

Equimolar?

Fraction (if it is not equimolar):

<input type="text"/>	Al
<input type="text"/>	B
<input type="text"/>	C
<input type="text"/>	Co
<input type="text"/>	Cr
<input type="text"/>	Cu
<input type="text"/>	Fe
<input type="text"/>	Hf
<input type="text"/>	Mn
<input type="text"/>	Mo
<input type="text"/>	N
<input type="text"/>	Nb
<input type="text"/>	Ni
<input type="text"/>	Sn
<input type="text"/>	Ta
<input type="text"/>	Ti
<input type="text"/>	V
<input type="text"/>	W
<input type="text"/>	Zr

Source: own authorship, 2022.

6.2.4 Obtainment of the powder referred to each alloy element

Some chemical elements were individually available in powder, others in chip, others in bar, and others in piece form. Some chemical elements are also available in compounds of two elements (for example, Fe-Ta, Fe-Nb, Fe-V). The ones in powder form were acquired in small plastic pots, the ones in chip, bar, and piece form were

purchased in plastic bags. For example, [Fig. 27](#) shows the pots of iron, manganese, nickel, chrome, and aluminum. [Tab. 3](#) lists the chemical elements used in this thesis, their available form, and their purity.

Table 3 - Chemical elements, their available forms, and purity.

Chemical elements	Available form	Purity (%)
Al	Powder	≥ 99.00
Cr	Powder	≥ 99.00
Cu	Powder	≥ 99.00
Fe	Powder, and piece	≥ 99.00
Mo	Powder, and piece	≥ 99.99
Nb	Powder, chip, and piece	≥ 99.00
Ta	Powder, and piece	≥ 99.00
Ti	Bar	≥ 99.00
V	Powder, and piece	≥ 99.00
W	Powder	≥ 99.00

Source: own authorship, 2023.

Figure 27 - Pots of iron, manganese, nickel, chrome, and aluminum powder.



Source: own authorship, 2022.

6.2.5 Weighing of each powder mass (metallic powder of each alloy element)

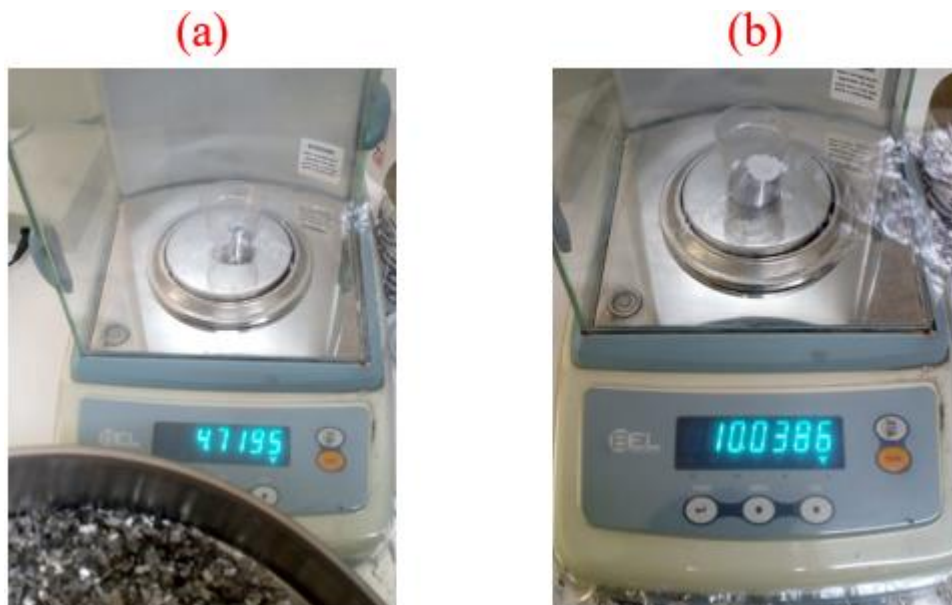
The weighing process consists of the following steps:

- (a) transferring the required quantity of powder of the alloy element from the correspondent small plastic pot to the beaker;

- (b) weighing of the alloy element;
- (c) transferring the weighted alloy element to another beaker (where all the element powders will be mixed;
- (d) repetition of the process from the stage (a) until stage (c) till all the elements are in the second beaker.

Commonly, the alloy elements were available to the project already in the form of powder, but there were exceptions. For example, niobium was first obtained in chip-shaped machines. Then it has been cut into smaller pieces to be part of the alloy (see [Fig. 28a](#)). As titanium was available only in bar form, it has been cut into a major piece with almost its required mass, and the remaining part was obtained in the form of powder produced by filing (see [Fig. 28b](#)), what might have contaminated the alloy powder.

Figure 28 - (a) weighing process of the niobium pieces; (b) weighing process of the titanium bar.



Source: own authorship, 2022.

6.2.6 Mixing of the powders in the most homogeneous manner

After weighing all the alloy elements, the powder was disposed of in a heterogeneous manner. To obtain the most homogeneous powder mix possible, a metallic spoon was used to mix the elements inside the beaker (alternated movements,

spiral movements, and manual vibrations). [Fig. 29](#) shows the powder of the alloy elements being mixed, aiming at achieving the most homogeneous mix as possible. However, as titanium and niobium were frequently added up to the alloy in pieces, they do not take part in this initial mix. They were positioned right above the upper part of the compacted powder when the melting process was being performed.

Figure 29 - Powder mixing with a spoon in the beaker.



Source: own authorship, 2022.

6.3 Obtainment of Compacted Powder Blend

The obtainment of the compacted powder blend includes the compaction of the powder mass, melting of the compacted powder, solidification of the molten alloy, transformation of the solidified alloy into powder (blend), and pressing of the blend in almost final dimensions of the product.

6.3.1 Pressing (compaction) of the powder mass

Once a relatively homogeneous powder mix is achieved, it must be pressed in order to form a compact powder mix to minimize the efforts in the posterior stage of homogenization of the molten alloy. The following steps describe the pressing stage:

- (a) opening of the double piston and cylinder set, separating the three parts.
- (b) cleaning, by using cotton (or paper) embedded in hydrated ethyl alcohol 70°, of each part of previously opened set;

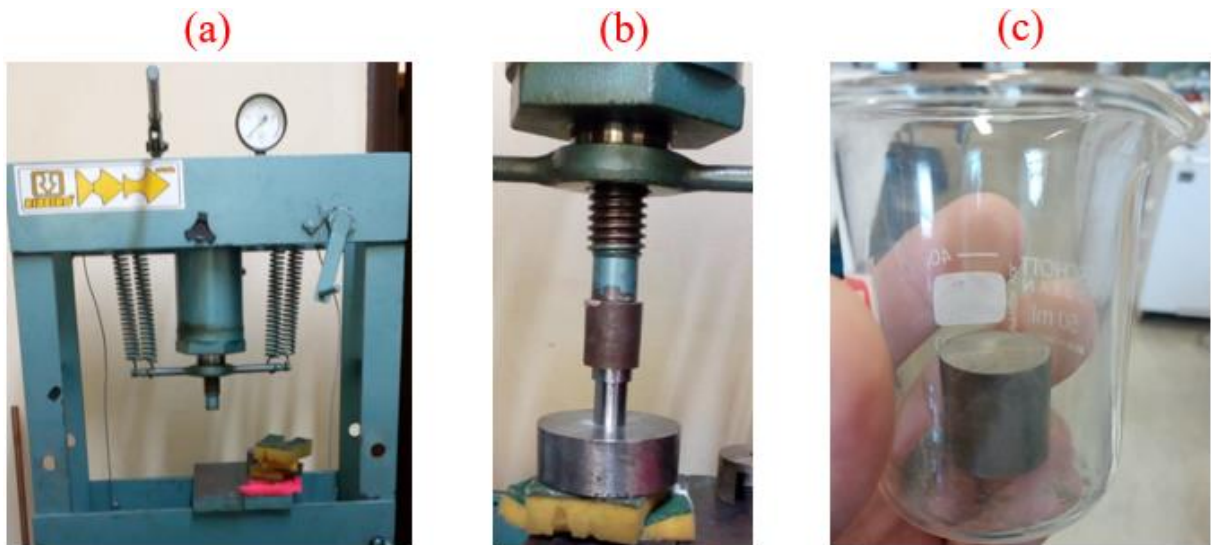
- (c) insertion of the powder mix of metal alloy elements into the piston and cylinder set chamber;
- (d) closure of the set (with the powder inside its chamber);
- (e) positioning of the set in the central position of the press;
- (f) alignment of the piston of the press to the positioned set;
- (g) application of pressure into the entire set;
- (h) holding on the pressure for at least five seconds to allow accommodation;
- (i) relief of the pressure to collect the set;
- (j) removal of one of the pistons from the set;
- (k) usage of an extractor to push the cylinder until it touches its end stop;
- (l) usage of tweezers to remove the metallic compact disc from the piston and place it inside a beaker.

[Fig. 30a](#) shows the hydraulic pressing equipment. [Fig. 30b](#) shows the detail of the interface between the pressing equipment and the matrix inside which there is the metal powder being pressed. The extraction stage is performed with the aid of the pressing and an extractor (see [Fig. 30b](#)). The compacted powder cylinder already extracted can be seen in [Fig. 30c](#).

Titanium and niobium pieces were not included in the mass to be compacted because as they are in form of bars or pieces they probably would damage the walls of the matrix. Therefore, only the other alloy elements were included in the mass to be compacted.

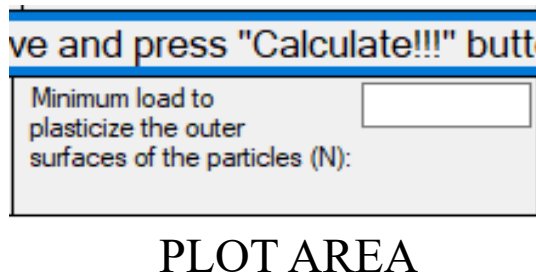
The pressure to be applied in order to compact the powder was obtained via the software PComp, developed exclusively for this thesis. Consequently, the minimum load to plasticize the outer surfaces of the particles (main output, see [Fig. 31](#)) was imposed to the equipment in order to try to assure the plasticization of the particles, forming a highly compacted cylinder.

Figure 30 - (a) pressing equipment; (b) pressing equipment forcing down the pin of the matrix against the hole of the matrix; (c) compacted powder cylinder in the beaker.



Source: own authorship, 2022.

Figure 31 - Main output field of "PComp" software.



Source: own authorship, 2022.

6.3.2 Melting of the compacted powder

After being compacted, the disc was melted in order to form a homogenized alloy. Therefore, the cylinder was placed into the chamber of the plasma furnace Rematitan autocast (Dentarium®) dotted with a tungsten electrode (see [Fig. 32](#) and [Fig. 33a](#)). The chamber inlet was fed with argon gas by a cylinder in order to difficult the oxidation mechanisms when the alloy was at high temperature (see [Fig. 33b](#)). When turned on, the electrode performs an electric discharge over the compacted cylinder (as can be seen in [Fig. 33c](#)), which is expected to melt partially or entirely. If it is a partial melt, it is necessary to turn the disc upside down to promote the tentative of

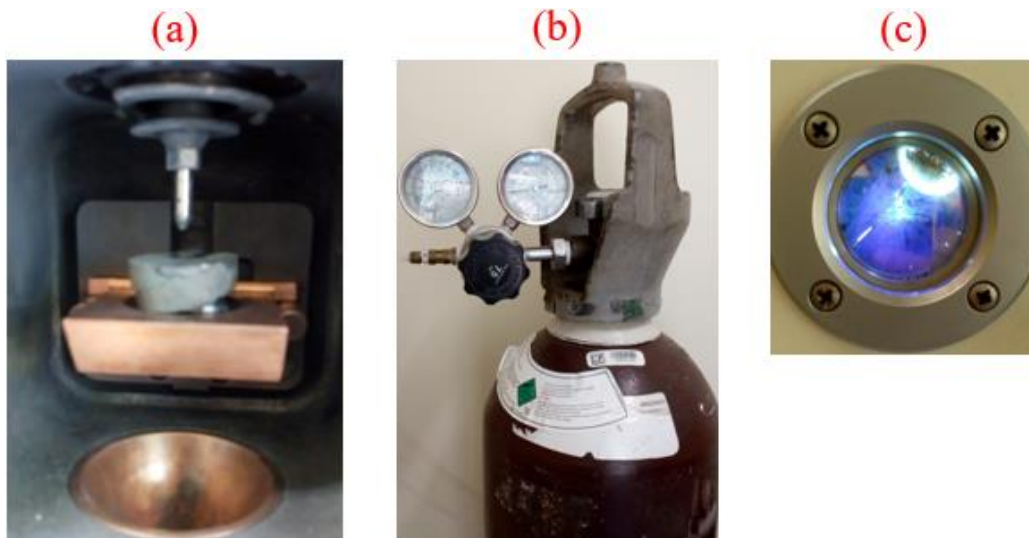
melting the yet unmelted part. To achieve the desired degree of homogenization, even if the cylinder was entirely melted in the first tentative, it may be necessary to turn the cylinder upside down to another melt(s).

Figure 32 - Plasma furnace Rematitan autocast (Dentaram®).



Source: own authorship, 2022.

Figure 33 - (a) plasma furnace chamber with tungsten electrode; (b) gas cylinder; (c) electrical discharge from the tungsten electrode to the cylinder in the furnace chamber.



Source: own authorship, 2022.

The necessary number of melts depends on the observation of the microstructure of the brand new alloy. After the electrical discharge is completed, the molten alloy is let fall into the ingot mold. Therefore, the molten alloy solidifies inside the ingot, assuming the form of the ingot. In this thesis, the furnace is set up to 49 seconds of exposure time of the compacted mix. In [Fig. 34a](#), the ingot results in the form of a flat cylinder; in [Fig. 34b](#), the form of a slim cylinder; and, in [Fig. 35](#), the form of a rectangular cross-section prism.

Figure 34 - (a) flat cylinder ingot mold; (b) slim cylinder ingot mold.



Source: own authorship, 2022.

Figure 35 - Ingot mold of rectangular cross-section prism.



Source: own authorship, 2022.

6.3.3 Solidification of the molten alloy

The molten alloy in the plasma furnace chamber was solidified under an argon atmosphere in order to partially avoid oxidation. Due to its high energy level, the external surface was expected to oxidize anyway. Water was used to cool the molten cylinder, solidifying it. [Fig. 36a](#) and [Fig. 36b](#) show, respectively, a solidified alloy in a flat cylinder ingot mold, and another in a slim cylinder ingot mold.

Figure 36 - (a) solidified alloy in a flat cylinder ingot mold; (b) solidified alloy in a slim cylinder ingot mold.



Source: own authorship, 2022.

6.3.4 Separation of a sample for verification of hardness and chemical composition

The core mass of the solidified alloy was separated in order to check its hardness and chemical composition. First, the solidified alloy was put into a mold inside which a resin was poured and left to solidify. The mass of resin and the solidified alloy (see [Fig. 37](#)) were then sanded to acquire the required surface finish to be tested.

Figure 37 - Resin and solidified alloy sanded to be tested.



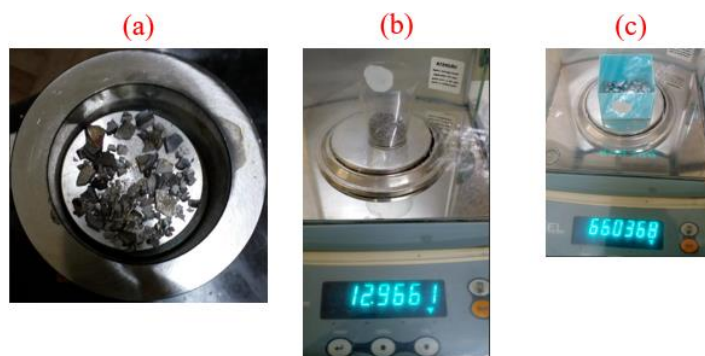
Source: own authorship, 2022.

6.3.5 Transformation of the remaining part of the solidified alloy into powder (blend) and sieving to use granulation powder of up to 200 micrometers

By performing one of the methods described in [section 3.3](#) it is possible to make powder from the obtained alloy, which now constitutes a blend, allowing it to be used in any product by the adequate means. In this thesis, the mechanical method (see [section 3.3.3](#)) was selected to run this process. As it is a fracture mechanics-governed phenomenon, the particle size reduction during this process was achieved by generating cracks, propagating, and fracturing them. Although the efficiency is low, the cost is also low. The low cost of the mechanical method associated with its prompt availability in the Thermophysical Laboratory (UNISO) led to its selection in this thesis.

First, the solidified alloy (in the form of a cylinder or another prism) was hammered inside a plastic protection, aiming at obtaining fragments of the referred alloy, which were then subjected to pressing in order to reduce the particle size (as per [Fig. 38a](#)).

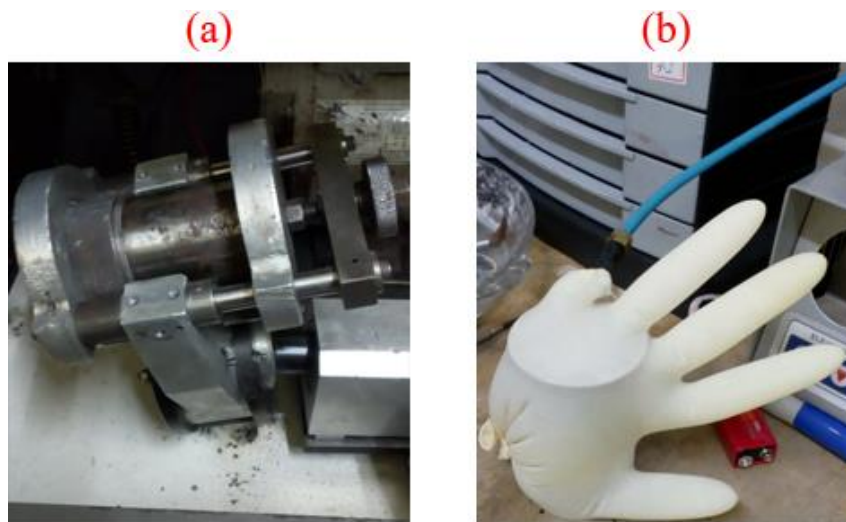
Figure 38 - (a) alloy inside matrix before pressing; (b) alloy being weighted; (c) balls being weighted.



Source: own authorship, 2022.

After this stage, the particles were weighted (see [Fig. 38b](#)) because the verified mass is used to determine the mass of the balls (see [Fig. 38c](#)) in the mechanical comminution process. This employed process is called shaker milling and similar to the planetary ball milling, but with the steel balls and the alloy particles inside a sealed cylinder (see [Fig. 39a](#)). However, before the cylinder has been closed, the monoglove technique (see [Fig. 39b](#)) was applied to remove the oxygen from inside the cylinder (already with the particles and balls). This set was moved around all the possible degrees of freedom to comminute the powder. Small and large balls were used in the ratio of 5:1, i.e. for each large ball, five small ones are added to the cylinder, and the mass of all the balls is ten times greater than the particles mass. The time of ball milling process depends on the material to comminute, method, and mass to reduce into powder. An empirical time of twenty minutes was used in the procedures of this thesis.

Figure 39 - Cylinder sealed with the alloy particles and the balls inside it.



Source: own authorship, 2022.

After this time, the particles, powder, and balls were retrieved from the ball-milling cylinder and then sieved using the adequate sieve to separate the acceptable powder from the particles (see [Fig. 40a](#), and [Fig. 40b](#)). The latter were going to be comminuted again in order to achieve the desired size. This procedure was repeated until all the powder passed through the required sieve.

Figure 40 - (a) sieving process to separate the acceptable particles from the non-acceptable ones; (b) 500 micrometers sieve (intermediate sieve to reach up to 200 micrometers).



Source: own authorship, 2022.

6.3.6 Powder density obtainment

The alloy density was estimated by pycnometrics technique, in which Helium gas is pressurized inside a chamber (where there is metal alloy powder sample) (see [Fig. 41](#)).

Figure 41 - Pycnometer Quantachrome model Ultrapyc 1200e.



Source: own authorship, 2022.

For each powder sample, three attempts were conducted, in which the mean of the volume of the powder, its density, and the standard deviation of the volume were extracted. The equipment “Quantachrome model Ultrapyc 1200e” (see [Fig. 41](#)), installed in the Applied Nuclear Physics Laboratory (LAFINAU, UNISO), requires the powder mass and the alloy nomenclature to be inserted to begin the evaluation. The values obtained by this technique must be compared to theoretical values to check if the measured values converge to the theoretical values.

6.3.7 Compaction of the blend in almost final dimensions of the product

According to the activities developed in this thesis, in order to obtain the desired product in almost its final dimensions, a mold had to be prepared to receive the powder to be compacted, and posteriorly sintered (see [Fig. 42](#)).

Figure 42 - Pressing of the alloy powder to form a compacted cylinder right before sintering.



Source: own authorship, 2022.

6.4 Software Developed for Powder Compaction

In order to describe the behavior of the powder mass quantitatively, there are several approaches, of which three are listed here. The first one considers the compacted powder mass as a homogeneous sample, extracting the relation between pressure and density, and radial pressure, for example. Another manner to deal with

this physical situation is to apply the continuum mechanics and/or computer simulation, obtaining the response stresses, deformations, and density distribution. The last approach cited here refers to the micromechanics of compaction, where the behavior of the individual particles under pressure is analyzed.

A software for compaction denominated “PComp” was coded in Microsoft Visual Studio 10.0® via emulation of Microsoft Visual Basic 6.0® ambient. There are ten input data fields in the “PComp” interface. In the following list, they are associated with the corresponding variable (after the description of the field) adopted in this paper and the referred main equation. The input data are presented in [Tab. 4](#).

Table 4 - Input data in “PComp”, corresponding data and equations.

Input data	Variable	Equation
Powder mass (g)	m	31
Bulk volume (mm^3)	V_{bu}	32
Theoretical volume (mm^3)	V_{th}	33
Compacted powder height (mm)	h	59
Particle inner radius (mm)	a	40
Particle outer radius (mm)	b	40
Material yield strength (MPa)	S_y	40
Friction coefficient between powder and die	μ	48
Punch diameter (mm)	$2r$	55
Compacted powder diameter after extraction (mm)	L_f	60

Source: own authorship, 2022.

It provides the following output: (a) the field “Porosity (%)” represents the variable ϕ ; (b) the field “Load to extract the powder compact (N)” corresponds to the variable F_e ; (c) the field “Minimum load to plasticize the outer surfaces of the particles (N)” is associated to the variable P_{MIN} ; (d) the field “Radial pressure during pressing (MPa)” is represented by the variable P_r ; and (e) the field “Spring back (%)” corresponds to the variable S_b . Just below the output described, the last output, “Plot area”, plots the axial stress distribution along the height of the powder mass (see [Fig. 43](#)).

Figure 43 - Empty interface of "PComp" software.

The screenshot shows the PComp software interface. It features a title bar with the icon and name 'PComp', and standard window controls (minimize, maximize, close). The main area is divided into three columns of input fields:

- Column 1:** Powder mass (g), Bulk volume (mm³), Theoretical volume (mm³), Compact powder height (mm).
- Column 2:** Particle inner radius (mm), Particle outer radius (mm), Material yield strength (MPa), Friction coefficient between powder and side wall of die.
- Column 3:** Punch diameter (mm), Compacted powder cylinder diameter after extraction (mm).

Below the input fields are two buttons: a green 'Calculate!!!' button and a red 'Restart' button. A blue banner with white text reads: 'Fill in only the 10 fields above and press "Calculate!!!" button. Read the 5 results below.' Below this banner are five output fields arranged in three columns:

- Column 1:** Porosity (%), Load to extract the powder compact (N).
- Column 2:** Minimum load to plasticize the outer surfaces of the particles (N).
- Column 3:** Radial pressure during pressing (MPa), Spring back (%).

At the bottom of the interface is a large section labeled 'PLOT AREA'.

Source: own authorship, 2022.

The referred software intends to guarantee that all the powder particles plasticize their outer surfaces. If this condition is reached, in case of sintering, the porosity can be reduced.

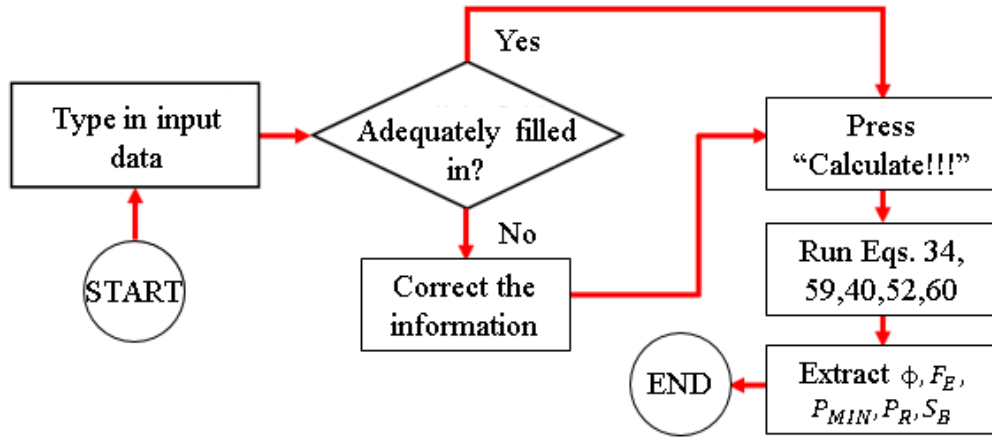
It is worth mentioning that, in fact, the computer program only estimates the described output data and these outputs may not reflect the physical condition of the sample. This is due to the uncertainty inherently involved in the process. Two examples are particle size, and form. The former is considered as a mean size, and the latter is sphere-like. Measurement procedures and estimation of unknown parameters are also sources of uncertainty. Therefore, the software only estimates the output data, which may differ from the real situation.

According to [Fig. 43](#), all the fields are initially in a blank state. As input data, there are ten fields to be filled in as a minimum requirement for calculation. Contrarily, an error message will appear. After this task is accomplished, it is necessary to press the green "Calculate!!!" button to obtain the six output data (five values, and the plot of the axial stress *versus* the mass powder height). The red "Restart" button has to be pressed if a new calculation has to be performed. This action restarts the software with all the fields in blank state.

To provide the referred output from the required input, an adequate internal software architecture is brought, which consists of programming sentences sequentially

disposed. As an alternative, the computer program operation process is illustrated by means of a flowchart in [Fig. 44](#).

Figure 44 - Computer program “PComp” workflow.



Source: own authorship, 2021.

6.5 Sintering

The sintering processes conducted within the scope of this thesis can be resumed in [Tab. 5](#), where the columns from left to right represent, respectively:

- (a) Code of the alloy subjected to sintering, which is given to facilitate the reference to the alloys from now on.
- (b) alloy subjected to sintering;
- (c) fusion number;
- (d) powder granulation;
- (e) gas used in the process;
- (f) temperature rate of the ascent ramp, T_{RAR} ;
- (g) threshold temperature (constant value of temperature in order to allow the required transformations), T_{THR} ;
- (h) time spent in threshold temperature t_{THR} ;
- (i) temperature rate of the descent ramp, T_{RDR} .
- (j) addition (getters), applied to minimize the presence of oxygen (to avoid oxidation), in a volume that occupies all the passages in the sintering furnace.

Table 5 - Sintering parameters for the alloys.

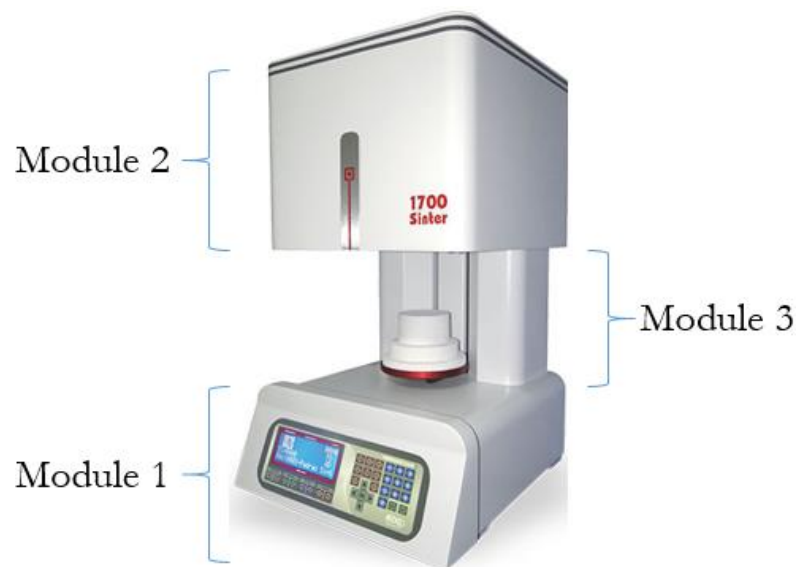
Co de	Alloy	Fusi on	Gran. (μm)	Gas	T_{RAR} (°C/min)	T_{THR} (°C)	t_{THR} (h)	T_{RDR} (°C/min)	Add
01	L4	F1	500	Ar-H ₂ (4%)	10	1200	1	20	None
02	L4.1	F1	500	Ar-H ₂ (4%)	10	1200	1	20	None
03	L7	F1	500	Ar-H ₂ (4%)	10	1200	1	20	None
04	L7	F4	500	Ar-H ₂ (4%)	10	1200	1	20	None
05	L7	F5	500	Ar-H ₂ (4%)	10	1200	1	20	None
06	L4	F1	500	Ar-H ₂ (4%)	10	1200	1	20	Zr
07	L4.1	F1	500	Ar-H ₂ (4%)	10	1200	1	20	Zr
08	L7	F1	500	Ar-H ₂ (4%)	10	1200	1	20	Zr
09	L7	F4	500	Ar-H ₂ (4%)	10	1200	1	20	Zr
10	L7	F5	500	Ar-H ₂ (4%)	10	1200	1	20	Zr
11	L4	F1	500	Ar	10	1200	1	20	Nb+Zr
12	L4.1	F1	500	Ar	10	1200	1	20	Nb+Zr
13	L5	F1	300	Ar	10	1200	1	20	Nb+Zr
14	L7	F1	500	Ar	10	1200	1	20	Nb+Zr
15	L7	F4	500	Ar	10	1200	1	20	Nb+Zr
16	L4	F1	500	Ar	10	1200	1	20	Zr+C
17	L4.1	F1	500	Ar	10	1200	1	20	Zr+C
18	L5	F1	300	Ar	10	1200	1	20	Zr+C
19	L7	F4	500	Ar	10	1200	1	20	Zr+C
20	L4	F1	200	Ar-H ₂ (4%)	10	1300	2	20	None
21	L5	F1	300	Ar-H ₂ (4%)	10	1300	2	20	None
22	L5	F3	500	Ar-H ₂ (4%)	10	1300	2	20	None
23	FN22	F1	500	Ar-H ₂ (4%)	10	1300	2	20	None
24	L4	F1	200	Ar-H ₂ (4%)	10	1300	2	20	None
25	L4Cu	F1	125	Ar-H ₂ (4%)	10	1300	2	20	None
26	L5	F3	500	Ar-H ₂ (4%)	10	1300	2	20	None
27	L5Cu	F3	125	Ar-H ₂ (4%)	10	1300	2	20	None
28	FN22	F1	500	Ar-H ₂ (4%)	10	1300	2	20	None
29	L4	F1	500	Ar-H ₂ (20%)	10	1400	1	20	None
30	L5	F3	500	Ar-H ₂ (20%)	10	1400	1	20	None
31	L5Cu	F3	500	Ar-H ₂ (20%)	10	1400	1	20	None
32	L5.1	F1	500	Ar-H ₂ (20%)	10	1400	1	20	None
33	L4	F1	500	Ar-H ₂ (5%)	10	1400	3	20	None
34	L5	F3	500	Ar-H ₂ (5%)	10	1400	3	20	None
35	L5Cu	F3	500	Ar-H ₂ (5%)	10	1400	3	20	None
36	L5.1	F1	500	Ar-H ₂ (5%)	10	1400	3	20	None
37	L4	F1	500	Ar	10	1100	1	20	None
38	L4	F1	200	Ar	10	1400	3	20	None
39	L5	F4	500	Ar	10	1400	3	20	None
40	L5Cu	F3	500	Ar	10	1400	3	20	None
41	L5.1	F1	500	Ar	10	1400	3	20	None

Source: own authorship, 2022.

6.5.1 Furnace employed

The furnace employed in sintering is the F1700 Sinter vertical equipment from EDG manufacturer, located at Thermophysical Laboratory, University of Sorocaba (UNISO). It comprises module 1 (electronic control, power module, communication, and feeding), module 2 (furnace muffle, sensors, and drives), and module 3 (elevator, and motor), as per [Fig. 45](#).

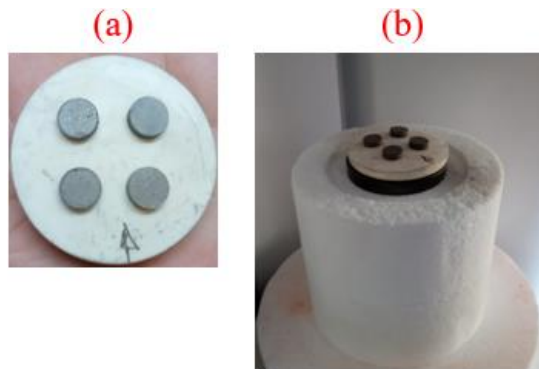
Figure 45 - Sintering furnace composed of three modules.



Source: own authorship, 2022.

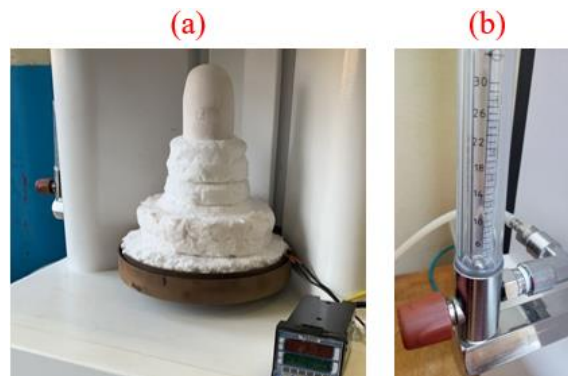
The compacted cylinders are disposed over a ceramic plate (see [Fig. 46a](#)) or a ceramic cup that is placed over the base of the sintering chamber (see [Fig. 46b](#)), which is completed with the cover, as per [Fig. 47a](#). The sintering chamber is located at the elevator, which is triggered to raise the chamber to reach up the furnace muffle. Inside the muffle, the chamber will experiment with a programmed temperature variation over time. Before starting the program, the gas flow was adjusted at about 200 ml/min in the flowmeter in order to minimize the oxidation in the cylinders (see [Fig. 47b](#)).

Figure 46 - (a) compacted flat cylinders before going into the sintering furnace; (b) ceramic plate over the sintering chamber base.



Source: own authorship, 2022.

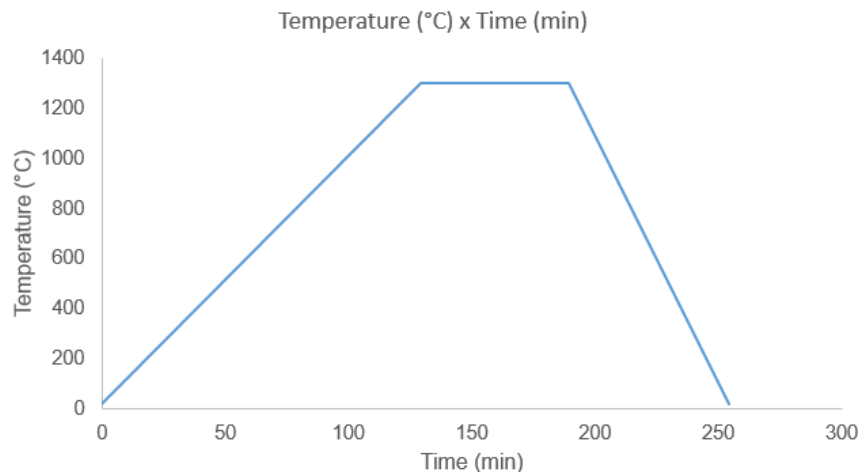
Figure 47 - (a) cover and insulation placed over the plate in order to form the sintering chamber; (b) flowmeter of the sintering furnace.



Source: own authorship, 2022.

The programs created inside the furnace memory for this thesis using the electronic control screen automatically actuate the elevator and, as soon as the elevator reaches its highest position, the program starts counting time and elevating the temperature. Thenceforth, the sintering program is executed until it stops due to an abnormality or until it ends (see [Fig. 48](#)). The sintering program comprises a rising ramp, a horizontal level, and a descending ramp. Although the program should be designed inputting the ramp slopes, it is expected that the temperature gradients are nonlinear in the experiment. [Fig. 49a](#) and [Fig. 49b](#) show, respectively, the ascending ramp and the constant temperature of the horizontal level.

Figure 48 - One of the programs created for sintering the compacted cylinders.



Source: own authorship, 2022.

Figure 49 - Control screen showing: a) ascending ramp being executed in the experiment; b) highest horizontal level in the experiment.



Source: own authorship, 2022.

The sintered cylinders were then analyzed in terms of their densification and oxidation, aiming at checking if the selected parameters were well suited for the experiments performed.

6.5.2 Sintered part density obtainment

In this thesis, the density of the sintered parts were obtained via two methods:

- (a) the simple calculation, based on mass/volume ratio.
- (b) the Archimedes' principle (hydrostatic weighing).

In the latter method, the sintered part was weighted in stationary air. Then, the part was weighted in the condition of total immersion in water. Therefore, Eq. 74 gives the density of the sintered part (ρ_{SP}), where W_{AIR} is the weight of the sintered part in air, W_{WATER} is the weight of the sintered part in water, and ρ_{WATER} is the density of water.

$$\rho_{SP} = \frac{W_{AIR}}{W_{AIR} - W_{WATER}} \rho_{WATER} , \quad (74)$$

[Fig. 50](#) shows a sintered part totally immersed in water being weighted in order to have its density determined.

Figure 50 - Hydrostatic weighing.



Source: own authorship, 2022.

6.5.3 Dilatometry

The pellets were placed in the dilatometer (SETARAM Setsys TMA 18) under a load corresponding to two times the gravitational acceleration. The atmosphere to which the samples were subjected was 50 mL/min dynamic Ar-10% H_2 and the heating rate was 10 °C/min up to 1500 °C, for a dwelling time of 1 h. The samples were also

analyzed at a Setaram Setsys Evolution 18 DSC up to 1500 °C at the same heating rate, without a holding time. Copper (3 wt.% Cu, 3 μ m powder) was mixed with L5 alloy powder because it has no solubility in most refractory metals found in the alloy formulation, actually being repealed by such metals ([RESTIVO et al., 2014](#)) ([RESTIVO; CASTANHO, 2010](#)). Therefore, copper stands as a liquid phase all along the process and can increase the densification by the liquid phase sintering (LPS). The sample holder, probe and crucibles were made from dense alumina. Some 8 mm diameter pellets were also prepared for furnace sintering in the range 1300-1400 °C under flowing Ar-4%H₂.

In this thesis, the dilatometry study was conducted over L4, L5, and L5.1 alloys because of their availability in the moment of the test. Moreover, they were the highest produced alloys. Therefore, their dilatometric profiles and DSC curves were obtained.

6.6 Software Developed for Sintering

Sintering demands qualitative and quantitative analyses of the results to substantiate the process effectiveness and efficiency. This is justified by the results that ground the decision-making process in the prediction of future experiments related to this process. The quantification and analysis of the involved parameters frequently demands procedural calculation.

Like “PComp”, “DIAMOY 1.0”, and DIAMOY 2.0”, “SINT” is a software coded in Microsoft Visual Basic 6.0® via emulation in Microsoft Visual Studio 10.0®. To obtain the output data, six data have to be input: (a) the field “Initial mass (g):” represents the variable m_i ; (b) the field “Initial height (mm):” corresponds to H_i ; (c) the field “Initial diameter (mm):” is associated to D_i ; (d) the field “Final mass (g):” represents m_f ; (e) the field “Final height (mm):” corresponds to H_f ; (f) the field “Final diameter (mm):” is associated to D_f . SINT is a tool that aims to provide the following five output data: (a) the field “Specific area variation:” is represented by k_s ; (b) the field “Initial density (g / cm³):” corresponds to ρ_i ; (c) the field “Final density (g / cm³):” corresponds to ρ_f ; (d) the field “Shrinkage:” is represented by S_k ; and (e) the field “Densification:” corresponds to Ψ (see [Fig. 51](#)).

Figure 51 - Empty interface of “SINT” software.

The screenshot shows a window titled "SINT" with a standard Windows title bar (minimize, maximize, close buttons). The interface is divided into two main sections: "INPUT DATA" and "OUTPUT DATA".

INPUT DATA: This section contains six input fields arranged in two columns and three rows. The left column has "Initial mass (g):", "Initial height (mm):", and "Initial diameter (mm):". The right column has "Final mass (g):", "Final height (mm):", and "Final diameter (mm):". Below these fields are two buttons: a red "Restart" button on the left and a blue "Calculate!!!" button on the right.

OUTPUT DATA: This section contains five input fields arranged in two columns and three rows. The left column has "Specific area variation:", "Initial density (g/cm³):", and "Final density (g/cm³):". The right column has "Shrinkage (%)ate":", "Densification (%)":", and an empty field for "Final density (g/cm³):".

Source: own authorship (2022).

Each of the five output data are associated to its corresponding variable and equation in [Tab. 6](#).

Table 6 - Output data in “SINT”, corresponding data, and equations.

Output data	Variable	Equation
Specific area variation (%)	k_s	66
Initial density (g / cm^3)	ρ_i	70
Final density (g / cm^3)	ρ_f	69
Linear shrinkage (%)	S_k	67
Densification (%)	Ψ	71

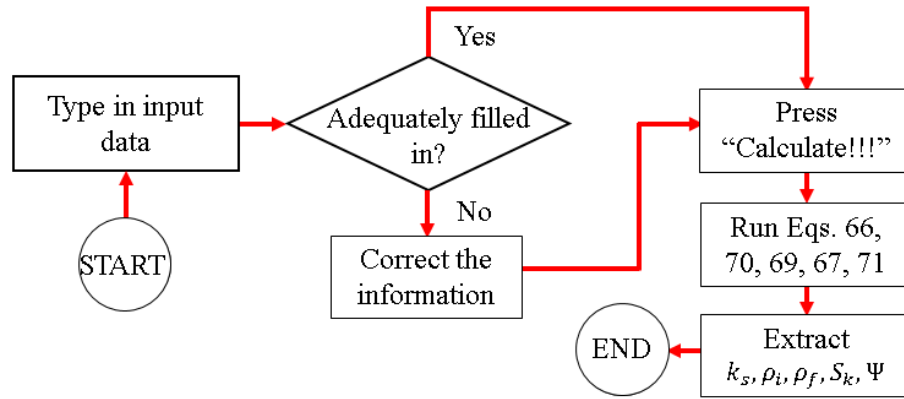
Source: own authorship (2022).

It is worth noting that eventual discrepancies may arise from the software results due to different existing sources of uncertainty. Consequently, it is not possible to assure that the output data will reflect the real situation.

When the icon of “SINT” software is double-clicked, the window shown in [Fig. 51](#) pops up. All the fields are initially in a blank state. In order to proceed to calculation, all the input data have to be filled in. If not adequately filled in, the program will show an error message. In the case of adequate input data filled in, the blue “Calculate!!!” button should be pressed, which will turn in the five referred output data. The red “Restart” button should be pressed if a new round of calculation has to be performed,

restarting the fields in the blank state. In addition, the computer program operation is shown in a flowchart in [Fig. 52](#).

Figure 52 - Computer program “SINT” workflow.



Source: own authorship (2022).

The input data in “SINT” software refers to alloy code 20 (from [Tab. 5](#)) and is shown in [Tab. 7](#).

Table 7 - Input data in “SINT”, corresponding variables, and values.

Input data	Variable	Value
Initial mass (<i>g</i>)	m_i	0.5476
Initial height (<i>mm</i>)	H_i	2.1500
Initial diameter (<i>mm</i>)	D_i	8.1000
Final mass (<i>g</i>)	m_f	0.5449
Final height (<i>mm</i>)	H_f	1.9500
Final diameter (<i>mm</i>)	D_f	8.0500

Source: own authorship (2022).

6.7 Alloy Testing

The scope of testing of the obtained alloys includes hardness testing, and scanning electron microscopy (SEM).

6.7.1 Hardness testing

The conceived EHMMAs were subjected to Vickers hardness testing in order to check their hardness and properly determine if they can be classified as EHMMAs. The metal sample was positioned at the center of the adjustable round table of the

durometer, located at the thermophysical laboratory (model Micron, see [Fig. 53](#)). It was configured to apply a load at a selected point of the sample, and measure the diagonals of the indentation produced. The dimensions of the diagonals were extracted via the upper *vernier*, and typed in via electronic panel. The equipment then provided the hardness magnitude to be read in the panel. The strategy of the hardness tests is to indent the samples (several times each one), and measure the diagonals and the fractures (when visible) using the hardness testing equipment. Most of the samples were tested upon loads of 1 *kgf* and/or 3 *kgf*.

Figure 53 - Hardness testing equipment.



Source: own authorship, 2022.

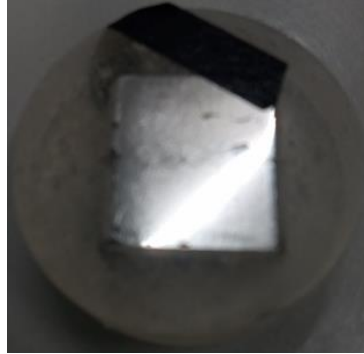
Before the list of metallic alloys exposed in [Tab. 5](#), those actually verified for their hardness were L4, L5, L5Cu, and L5.1 (according to [Tab. 10](#)) due to their availability in the time range intended for the tests, in addition to the fact that they were the most produced alloys.

6.7.2 Scanning electron microscopy (SEM) testing and dilatometry

The SEM testing was conducted in order to check the chemical composition of the tested alloys, and the degree of solid solution formation. The microstructure was evaluated in many different regions of the sample, which was obtained after polishing the solidified alloy sample (see [Fig. 54](#)). The black ribbon establishes the ground

connection between the metallic sample and the equipment in order to discharge the electrons.

Figure 54 - Alloy sample wrapped by resin to be scanned.



Source: own authorship, 2022.

In this thesis, SEM tests were performed in as-cast alloys (L4, L5, and L5.1), and in sintered samples of L4, L5, and L5.1 alloys.

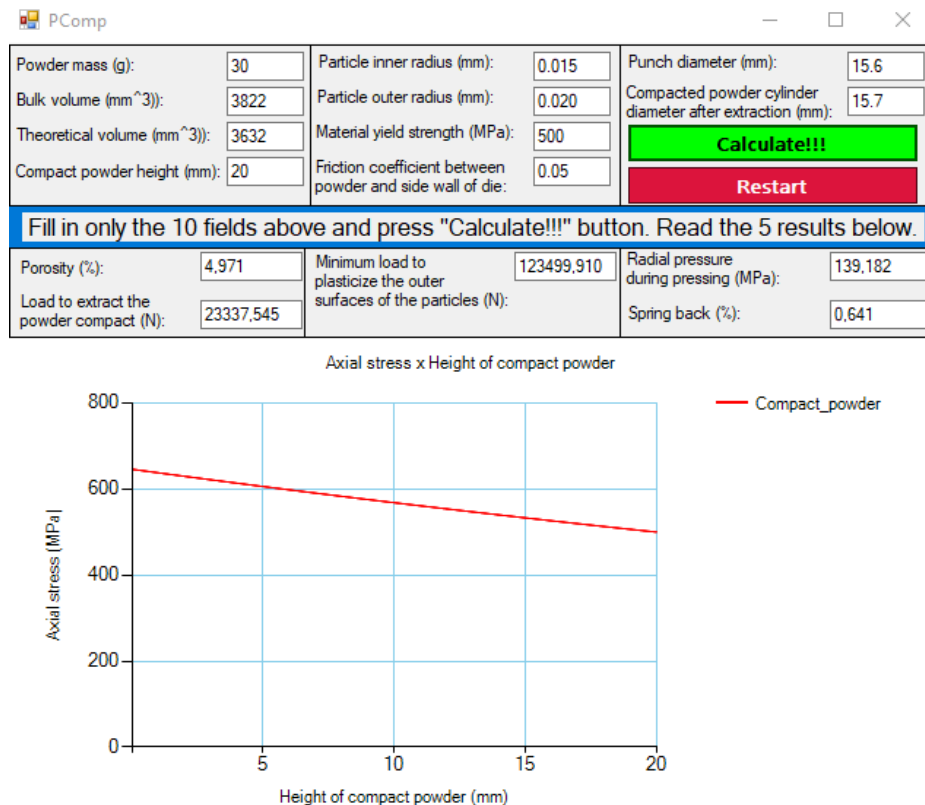
7 RESULTS AND DISCUSSION

This section includes results in powder compaction, prediction of the alloys, hardness, Scanning Electron Microscopy (SEM), Backscattered Electron (BSE), Differential Scanning Calorimetry (DSC), sintering, and production within this thesis.

7.1 Powder Compaction

As an example of the calculation to produce one of the compacted flat cylinders mentioned herein, the following data should be inputted in the software “PComp”. Metal alloy powder mass of 30 g, with a bulk volume of 3822 mm³, a theoretical volume of 3632 mm³, a particle inner radius of 0.015 mm, a particle outer radius of 0.020 mm, a material yield strength of 500 MPa, a friction coefficient between powder and die wall of 0.05, a punch diameter of 15.6 mm, and a compacted powder diameter after extraction of 15.7 mm (Fig. 55).

Figure 55 - “PComp” software and its results to compact a flat cylinder.



Source: own authorship (2022).

According to [Fig. 55](#), this compacted powder has a porosity of 4.971%, a radial pressure of 139.182 MPa during the pressing process, and a spring back effect of 0.641%. In terms of loads, the maximum to plasticize the outer surfaces of the particles is 123499.910 N, and the load to extract the compacted powder is 23337.545 N. Besides that, by observing the plot “Axial stress versus Height of the compacted powder”, the value of the curve assures that at the most distant point ($h = 20\text{ mm}$) the value of axial stress is not below the value corresponding to the material yield strength. This indicates that all the domain of compacted powder is in the plastic regime. Therefore, the software here introduced may be used as a tool to help in the pressing process observing the limiting conditions, although it can be easily adapted and updated to fulfill other requirements.

Therefore, the developed software is intended to: (a) be a close package encompassing the theoretical background to conduct the pressing process in an easier manner; (b) speed up of the preparation and execution of pressing; (c) predict the behavior and the results related to the compacted powder; (d) be a portable tool, which can be accessed in any Windows®-based device.

7.2 Prediction of the Designed Alloys Using the Software “DIAMOY 2.0”

The results using “DIAMOY 2.0” are reported in terms of the comparison between some of the calculated parameters from DIAMOY 2.0 and the same parameters available in ([RESTIVO, T. A. G.; RESTIVO, G. M. G., 2021](#)), referred to L6 alloy (AlCrFeMoNbTaTiVW) and L4 alloy (Cr₃FeMoNbTaTiV), according to the nomenclature found in ([RESTIVO, T. A. G.; RESTIVO, G. M. G., 2021](#)). This is the procedure followed in order to partially validate some of the results from the software.

[Fig. 56](#) and [Fig. 57](#) present the input data filled in (in the left side) and the output data printed (in the right side), separated by a green rectangle related to L6 and L4 alloys, respectively. In the “output” section, there are twenty parameters calculated and five statuses associated with their corresponding criteria, totaling twenty-five outputs. It is worth noting that the value of the field “product mass” (20 g) typed in does not influence the calculated parameters and statuses, but only the mass of each element in the solid solution.

By the fact that L6 alloy is equimolar and has nine distinct elements, the fourth region “Fraction (if it is not equimolar)” should be kept blank. In the case of L4 alloy,

there are seven chemical elements, being chromium molar fraction three times greater than the fraction of each other element. Therefore, the region “Fraction (if it is not equimolar)” should be filled in with the corresponding molar fraction. It is important to note that the action of filling in the molar fraction region (if it is not equimolar) does not avoid the checking of the second region “Alloy elements”.

Figure 56 - Interface of “DIAMOY 2.0” with the results related to L6 alloy.

The screenshot shows the DIAMOY 2.0 software interface. The **INPUT:** section includes a 'Product mass' field set to 20 g, an 'Equimolar?' dropdown set to 'Yes', and a 'Fraction (if it is not equimolar):' field. A list of alloy elements is shown with checkboxes: Al (checked), B, C, Co, Cr (checked), Cu, Fe (checked), Hf, Mn, Mo (checked), N, Nb (checked), Ni, Sn, Ta (checked), Ti (checked), V (checked), W (checked), and Zr. There are 'Restart!' and 'Calculate!' buttons. The **OUTPUT:** section displays a table of results for the L6 alloy.

Element	Mass (g)
Al	0,6854
B	0,0000
C	0,0000
Co	0,0000
Cr	1,3209
Cu	0,0000
Fe	1,4187
Hf	0,0000
Mn	0,0000
Mo	2,4375
N	0,0000
Nb	2,3602
Ni	0,0000
Sn	0,0000
Ta	4,5968
Ti	1,2160
V	1,2941
W	4,6703
Zr	0,0000

Atomic radii difference, Delta_r (%):	14,286
Status of atomic radii difference:	OK
Mean atomic radius (pm):	134,614
Polydispersion of atomic radii, delta:	0,052
Status of polydispersion of atomic radii:	OK
Chromium Equivalent (%):	144,786
Topological discrepancy, gamma:	1,179
Status of topological discrepancy:	NOK
Mean VEC:	5,333
Status of mean VEC:	BCC
Standard deviation of VEC:	1,333
Mean Electronegativity (Pauling):	1,766
Electronegativity difference (Pauling):	0,282
Mean melting point (°C):	2135,811
Standard deviation of melting point (°C):	791,710
Mean density (g / cm ³):	9,219
Standard deviation of density (g / cm ³):	5,140
Mean bulk modulus (GPa):	172,556
Standard deviation of bulk modulus (GPa):	68,243
Entropy of mixing (J / mol K):	18,268
Status of entropy of mixing:	STABLE
Average mixing enthalpy (kJ / mol):	-11,274
Standard deviation of mixing enthalpy (kJ / mol):	7,311
Lowered Gibbs' free energy (kJ / mol):	-55,280
Entropy-enthalpy relation:	3,903

Source: own authorship (2022).

Regarding the five statuses related to the presented criteria, the only one not fulfilled was the associated with topological discrepancy, γ , which status in both [Fig. 56](#) and [Fig. 57](#) is “NOK” (not ok). This means that this parameter was not attended because γ should be less than 1.175, as described in [subsection 2.5.5](#). The calculated values for L6 and L4 alloys are, respectively, 1.179, and 1.181.

Figure 57 - Interface of "DIAMOY 2.0" with the results related to L4 alloy.

DIAMOY 2.0

INPUT: Product mass: 20 g

Alloy elements: ☐ Al ☐ B ☐ C ☐ Co ☒ Cr ☐ Cu ☐ Hf ☐ Mn ☒ Mo ☐ N ☒ Nb ☐ Ni ☐ Sn ☒ Ta ☒ Ti ☒ V ☐ W ☐ Zr

Equimolar? **No** Fraction (if it is not equimolar):

Restart!

Calculate!

OUTPUT:

Element	Mass (g)
Al	0,0000
B	0,0000
C	0,0000
Co	0,0000
Cr	4,5859
Cu	0,0000
Fe	1,6413
Hf	0,0000
Mn	0,0000
Mo	2,8200
N	0,0000
Nb	2,7306
Ni	0,0000
Sn	0,0000
Ta	5,3181
Ti	1,4068
V	1,4972
W	0,0000
Zr	0,0000

Atomic radii difference, Delta_r (%):	14,286
Status of atomic radii difference:	OK
Mean atomic radius (pm):	132,027
Polydispersion of atomic radii, delta:	0,059
Status of polydispersion of atomic radii:	OK
Chromium Equivalent (%):	149,038
Topological discrepancy, gamma:	1,181
Status of topological discrepancy:	NOK
Mean VEC:	5,667
Status of mean VEC:	BCC
Standard deviation of VEC:	1,054
Mean Electronegativity (Pauling):	1,693
Electronegativity difference (Pauling):	0,187
Mean melting point (°C):	2105,980
Standard deviation of melting point (°C):	460,239
Mean density (g / cm ³):	8,365
Standard deviation of density (g / cm ³):	3,267
Mean bulk modulus (GPa):	166,777
Standard deviation of bulk modulus (GPa):	34,664
Entropy of mixing (J / mol K):	15,222
Status of entropy of mixing:	STABLE
Average mixing enthalpy (kJ / mol):	-7,322
Standard deviation of mixing enthalpy (kJ / mol):	4,394
Lowered Gibbs' free energy (kJ / mol):	-43,538
Entropy-enthalpy relation:	4,946

Source: own authorship (2022).

The comparison between the parameter values found in ([RESTIVO, T. A. G.; RESTIVO, G. M. G., 2021](#)) and the presented software is made in [Tab. 8](#) for L6 alloy, and in [Tab. 10](#) for L4 alloy. The first column corresponds to the parameter being compared, the second refers to the parameter values presented in ([RESTIVO, T. A. G.; RESTIVO, G. M. G., 2021](#)), the third expresses the results obtained from DIAMOY 2.0, and the fourth refers to the relative error between the data from second and third columns.

Table 8 - Comparison of parameter values between ([RESTIVO, T. A. G. and RESTIVO, G. M. G., 2021](#)) and the software developed (DIAMOY 2.0) for L6 alloy.

Parameter	RESTIVO, T. A. G. and RESTIVO, G. M. G., 2021	DIAMOY 2.0	Relative error (%)
δ	0.053	0.052	1.923
$\Delta r(\%)$	14.500	14.286	1.498
Cr_{eq}	145.000	144.786	0.148
γ	1.179	1.179	0.000
\tilde{V}	5.330	5.333	0.056
$\Delta\chi$	0.282	0.282	0.000
$\tilde{T}(^{\circ}C)$	2135.850	2135.811	0.002
$\tilde{\rho}(g / cm^3)$	9.390	9.219	1.855
$\Delta S_{MIX}(J / mol K)$	18.300	18.268	0.175
$\Delta H_{MIX}(kJ / mol)$	-11.300	-11.274	0.230

Source: own authorship (2022).

From [Tab. 8](#), it can be observed a relatively good agreement between the results obtained by the software and those by ([RESTIVO, T. A. G.; RESTIVO, G. M. G., 2021](#)) in terms of the relative error, which ranges from 0.000 (γ , and $\Delta\chi$) to 1.923% (δ) for the L6 alloy. It is important to point out that the null values of relative error are probably justified by the adopted rounding processes of both sources.

Therefore, within a 1.923% error margin, the results presented by the computer program can be used to partially validate the software related to L6 alloy ([RESTIVO, T. A. G.; RESTIVO, G. M. G., 2021](#)). In addition to the comparison of the parameters presented herein, none of the statuses obtained via the developed computer program was different from the presented in ([RESTIVO, T. A. G.; RESTIVO, G. M. G., 2021](#)).

Table 9 - Comparison of the available parameter values between ([RESTIVO, T. A. G. and RESTIVO, G. M. G., 2021](#)) and DIAMOY 2.0 in what refers to L4 alloy.

Parameter	RESTIVO, T. A. G. and RESTIVO, G. M. G. (2021)	DIAMOY 2.0	Relative error (%)
δ	0.059	0.059	0.000
$\Delta r(\%)$	14.500	14.286	1.498
Cr_{eq}	149.1	149.038	0.042
γ	1.181	1.181	0.000
\tilde{V}	5.670	5.667	0.053
$\Delta\chi$	0.187	0.187	0.000
$\tilde{T}(^{\circ}C)$	2105.85	2105.98	0.006
$\tilde{\rho}(g / cm^3)$	8.640	8.365	3.183
$\Delta S_{MIX}(J / mol K)$	15.200	15.222	0.145
$\Delta H_{MIX}(kJ / mol)$	-7.200	-7.322	1.666

Source: own authorship (2022).

In what refers to L4 alloy ([Tab. 9](#)), the results also present a relatively good agreement between those obtained by DIAMOY 2.0 and those by ([RESTIVO, T. A. G.; RESTIVO, G. M. G., 2021](#)). In this case, the relative error ranges from 0.000 (δ, γ , and $\Delta\chi$) to 3.183% ($\tilde{\rho}$). As pointed out in the description of the relative errors of L6 alloy, the null values of relative error related to L4 alloy are also possibly explained by the selected rounding processes. Consequently, in what refers to L4 alloy, the results presented by DIAMOY 2.0 can be used to validate the software within a 3.183% error margin. Similarly to what happened for L6 alloy, none of the statuses obtained via DIAMOY 2.0 was different from the reported in ([RESTIVO, T. A. G.; RESTIVO, G. M. G., 2021](#)). Consequently, the proposed software DIAMOY 2.0 can be used as a designing tool aiming at predicting the behavior of the intended alloys and possibly be tested upon the design process of similar EHMMAAs.

7.3 Hardness Values

The measured hardness values are disposed of in [Tab. 10](#). The sixth column corresponds to the load applied to the samples. The seventh column refers to the number of indentations applied to each sample, thus resulting in a mean value of Vickers hardness (seventh column). The number of indentations is mainly due to the dimensions of the sample, in which the limiting factor was the distance between indentations.

Table 10 - Hardness values measurements.

Code (Tab. 5)	Alloy	Fusion	T _{THR} (°C)	t _{THR} (h)	Load (kgf)	Indentations	Mean HV	Std dev HV
01	L4	F1	1100	3	1	5	1031,7	18,5
01	L4	F1	1100	3	3	3	895,2	8,7
01	L4	F1	1400	3	1	12	304,3	117,9
13	L5	F1	1100	3	1	5	978,5	33,4
13	L5	F1	1100	3	3	3	934,8	33,4
22	L5	F3	1400	3	1	7	487,4	96,4
27	L5Cu	F3	1400	3	1	17	766,3	223,7
32	L5.1	F1	1100	3	1	5	1055	46,4
32	L5.1	F1	1100	3	3	3	989,6	34,5
32	L5.1	F1	1400	3	1	12	1006,4	54,5
32	L5.1	F1	1400	3	3	3	907,3	68,7

Source: own authorship (2022).

Related to L4 alloy, the results in [Tab. 10](#) range from 154.0 HV (1400 °C) to 1051.2 HV (1100 °C, 1 kgf). L5 alloy varies between 340.9 HV (1400 °C) and 1026.7 HV (1100 °C, 1 kgf). L5Cu alloy goes from 422.5 HV to 1116.7 HV. The L5.1 alloy ranges from 847.9 HV (1400 °C, 3 kgf) to 1116.7 HV (1100 °C, 1 kgf). The lowest standard deviations related to L4, L5, L5Cu, and L5.1 are, respectively, 8.7, 33.4, 223.7, and 34.5, while the highest ones are, respectively, 117.9, 96.4, 223.7, and 68.7. By observing these values, both temperature and testing load influence the hardness achieved. In what refers to temperature, except for L5Cu, alloys heat-treated at 1100 °C presented the highest values of hardness, while the lowest values come from those heat-treated at 1400 °C. In the case of L5Cu, there is no sample heat treated at 1100 °C tested. This may be because there was grain coalescence (grain growth) at 1400 °C. This diminishes the hardness. Another possibility refers to a partial phase segregation, which tends to reduce the hardness. Concerning testing load, the load 1 kgf provides the highest hardness values. This can be explained by the fact that Vickers hardness depends on the load applied ([PETRÍK; PALFY, 2011](#)).

7.4 Sintering Results

Item divided into sintering results from experiment, from the SINT software, and from dilatometry.

7.4.1 Sintering results from experiments

Sintering procedures and codification of alloys (to simplify their presentation in tables) were followed as described in the sintering section (Material and Methods, [Section 6.5](#)). Therefore, the results related to the samples of the alloys (pre-and post-sintered) are presented in [Tab. 11](#). Therefore, the following data are presented in [Tab. 11](#): (a) alloy code (see [Tab. 5](#)); (b) alloy sample; (c) initial mass of the sample, $m_i(g)$; (d) initial diameter of the sample, $D_i(mm)$; (e) initial height of the sample, $H_i(mm)$; (f) initial density of the sample, $\rho_i(g / cm^3)$; (g) final mass of the sample, $m_f(g)$; (h) final diameter of the sample, $D_f(mm)$; (i) final height of the sample, $H_f(mm)$; (j) final density of the sample, $\rho_f(g / cm^3)$; (k) relative error of the density, $\varepsilon_p(\%)$.

Table 11 - Densification data for the samples subjected to sintering.

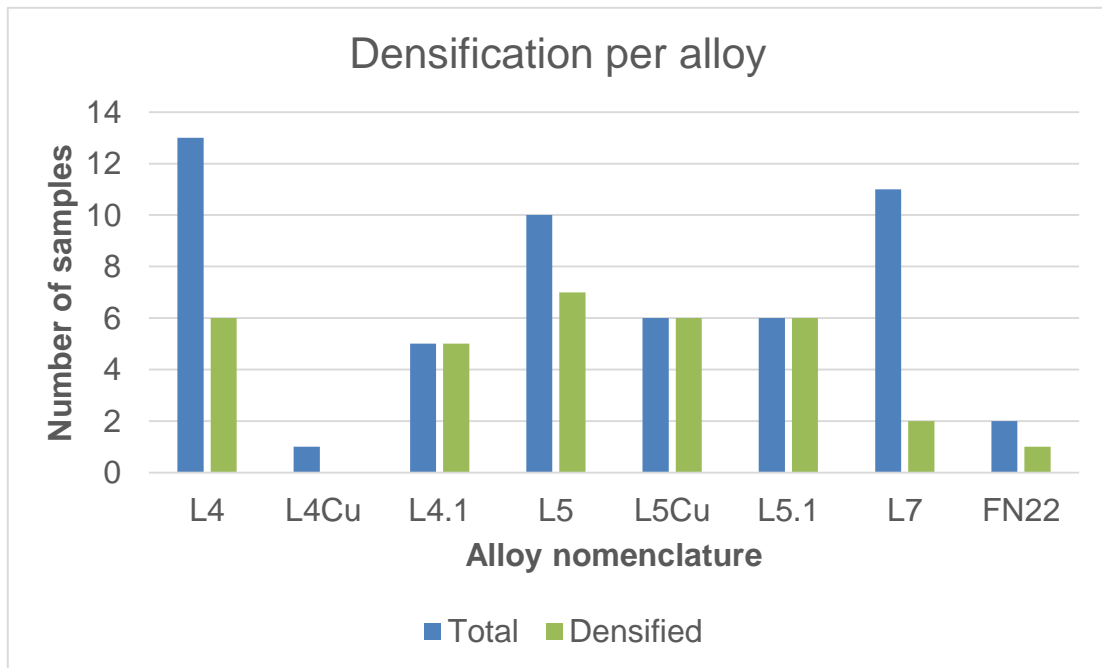
Co de	m_i (g)	D_i (mm)	H_i (mm)	ρ_i (g/cm ³)	m_f (g)	D_f (mm)	H_f (mm)	ρ_f (g/cm ³)	ε_ρ (%)
01	0.5950	8.00	1.95	6.07	0.6167	8.33	2.07	5.47	-9.94
02	0.7308	8.05	2.65	5.41	0.7682	8.19	2.71	5.38	-0.69
03	0.5961	8.05	1.90	6.16	0.6188	8.24	1.97	5.89	-4.44
04	0.6067	8.00	2.00	6.03	0.6293	8.24	2.04	5.78	-4.15
05	0.6032	8.05	2.15	5.51	0.617	8.15	2.17	5.45	-1.13
06	0.6993	8.00	2.20	6.32	0.6983	8.10	2.25	6.02	-4.76
07	0.7003	8.00	2.60	5.36	0.7055	8.25	2.59	5.10	-4.90
08	0.6994	8.00	2.10	6.63	0.7024	8.05	2.12	6.51	-1.75
09	0.7134	8.05	2.40	5.84	0.7198	8.06	2.33	6.05	3.67
10	0.7003	8.00	2.55	5.46	0.7088	8.06	2.51	5.53	1.30
11	0.7860	8.00	3.50	4.47	0.7876	8.20	2.75	5.42	21.39
12	0.6552	8.05	2.55	5.05	0.6649	8.20	2.65	4.75	-5.89
13	0.8046	8.10	2.40	6.51	0.809	8.05	2.45	6.49	-0.28
14	0.7930	8.05	2.50	6.23	0.8019	8.10	2.55	6.10	-2.08
15	0.8405	8.10	2.80	5.83	0.8467	8.10	2.85	5.76	-1.03
16	0.8535	8.05	2.95	5.68	0.8947	8.30	3.05	5.42	-4.63
17	0.6882	8.05	2.65	5.10	0.7308	8.35	3.00	4.45	-12.82
18	0.7354	8.05	2.35	6.15	0.7839	8.30	2.50	5.80	-5.75
19	0.9300	8.00	3.10	5.97	0.9769	8.05	3.25	5.91	-1.05
20	0.5476	8.10	2.15	4.94	0.5449	8.05	1.95	5.49	11.08
21	0.4457	8.10	1.50	5.77	0.4458	8.05	1.50	5.84	1.27
22	0.6991	8.10	2.35	5.77	0.7032	8.00	2.45	5.71	-1.09
23	0.9003	8.05	3.55	4.98	0.8974	7.45	3.35	6.15	23.33
24	0.5040	7.05	2.30	5.61	0.5023	7.06	2.34	5.48	-2.32
25	0.3704	7.05	1.70	5.58	0.374	7.08	1.78	5.34	-4.38
26	0.4813	7.05	2.20	5.60	0.486	6.96	2.17	5.89	5.04
27	0.3760	7.05	1.75	5.50	0.377	6.99	1.66	5.92	7.52
28	0.5382	7.05	2.55	5.40	0.5363	6.80	3.18	4.64	-14.11
29	0.1881	3.60	3.32	5.57	0.1895	3.71	3.42	5.13	-7.91
30	0.1276	3.50	2.40	5.53	0.1265	3.18	2.30	6.92	25.32
31	0.1088	3.50	2.10	5.39	0.1086	3.14	1.88	7.46	38.53
32	0.1074	3.60	2.26	4.67	0.1087	4.00	1.66	5.21	11.61
33	0.8050	8.10	3.00	5.21	0.8075	7.75	2.78	6.16	18.25
34	0.7977	8.15	2.75	5.56	0.7989	7.29	2.49	7.69	38.24
35	0.8431	8.10	2.90	5.64	0.8454	7.27	2.64	7.71	36.73
36	0.8149	8.10	3.95	4.00	0.8111	7.09	3.23	6.36	58.87
37	0.1297	3.60	2.38	5.35	0.1337	3.70	2.62	4.75	-11.35
38	0.7210	8.10	2.50	5.60	0.7155	7.32	2.27	7.49	33.82
39	0.8561	8.10	3.00	5.54	0.8574	7.55	2.87	6.67	20.50
40	0.6908	8.10	2.40	5.59	0.6877	7.43	2.23	7.11	27.33
41	0.8278	8.10	3.90	4.12	0.826	6.85	3.26	6.88	66.91

Source: own authorship (2022).

[Tab. 11](#) shows that the majority of the samples has not densified. Among the possible reasons for this are: (a) inadequate atmosphere; (b) insufficient compaction; (c) non-optimum exposure time; and (d) non-optimum temperature. In terms of densification, the worst result comes from FN22 alloy, which presented a relative error in the density of -14.11%, while the best result relates to L5.1 alloy, 66.91%.

From the 55 samples sintered, 27 have densified, i.e. 49.10%. Stratifying these values into the specified alloys, the following data is noticeable ([Fig. 58](#)). The blue bars over each alloy denomination mean the number of specific alloy samples subjected to sintering. The green bars over each alloy category indicate the number of densified samples under each category. Among these alloys, L4.1, L5Cu, and L5.1 need to be highlighted because all the samples subjected to sintering have densified. On the other hand, the only one L4 sample sintered has not densified. The other alloys just had a partial densification.

Figure 58 - Densification per alloy.



Source: own authorship (2022).

The densification of each alloy can also be verified by means of the ratio final-theoretical densities $[(\rho_f / \rho_{th}) 100] \%$. [Tab. 12](#) presents the code (see [Tab. 5](#)) and the

sample of each alloy associated to its final density (ρ_f), and theoretical density (ρ_{th}), aiming at showing how close their final densities are from the theoretical ones.

Table 12 - Densification data for the samples subjected to sintering.

Code	Sample	Alloy	ρ_f (g/cm ³)	ρ_{th} (g/cm ³)	$[(\rho_f / \rho_{th}) 100]$ %
01	02	L4	5.47	8.37	65.35
02	01	L4.1	5.38	6.82	78.89
03	01	L7	5.89	8.66	68.04
04	01	L7	5.78	8.66	66.82
05	01	L7	5.45	8.66	62.96
06	01	L4	6.02	8.64	72.00
07	01	L4.1	5.10	8.64	60.92
08	01	L7	6.51	8.66	75.20
09	01	L7	6.05	8.66	69.94
10	01	L7	5.53	8.66	63.93
11	02	L4	5.42	8.37	64.83
12	01	L4.1	4.75	6.82	69.65
13	01	L5	6.49	8.52	76.14
14	01	L7	6.10	8.66	70.49
15	02	L7	5.76	8.66	66.60
16	01	L4	5.42	8.37	64.81
17	01	L4.1	4.45	6.82	65.22
18	01	L5	5.80	8.52	68.01
19	01	L7	5.91	8.66	68.22
20	01	L4	5.49	8.37	65.64
21	01	L5	5.84	8.52	68.53
22	01	L5	5.71	8.52	67.01
23	01	FN22	6.15	7.37	83.34
24	01	L4	5.48	8.37	65.55
25	01	L4Cu	5.34	8.38	63.66
26	01	L5	5.89	8.52	69.08
27	01	L5Cu	5.92	8.53	69.35
28	01	FN22	4.64	7.37	62.98
29	01	L4	5.13	8.37	61.27
30	01	L5	6.92	8.52	81.27
31	02	L5Cu	7.75	8.53	90.77
32	01	L5.1	5.21	6.98	74.69
33	01	L4	6.10	8.37	72.94
34	02	L5	7.69	8.52	90.21
35	02	L5Cu	7.71	8.53	90.40
36	01	L5.1	6.73	6.98	96.49
37	01	L4	4.75	8.37	56.74
38	01	L4	7.49	8.37	89.54
39	01	L5	6.36	8.52	74.68

40	01	L5Cu	7.11	8.53	83.34
41	02	L5.1	6.88	6.98	98.54

Source: own authorship (2023).

[Tab. 13](#) compiles the range of percentage of theoretical density for each alloy. By observing these results, L4Cu does not get close to its theoretical density, although just one sample is reported. Among the alloys with two or more samples, the lowest range corresponds to L7, while the largest range belongs to L4. The highest minimum and maximum final-theoretical densities ratios comes from L5.1, which suggests that L5.1 is the most sinterable.

Table 13 - Range of the ratio final-theoretical densities $[(\rho_f / \rho_{th}) 100] \%$ from minimum to maximum.

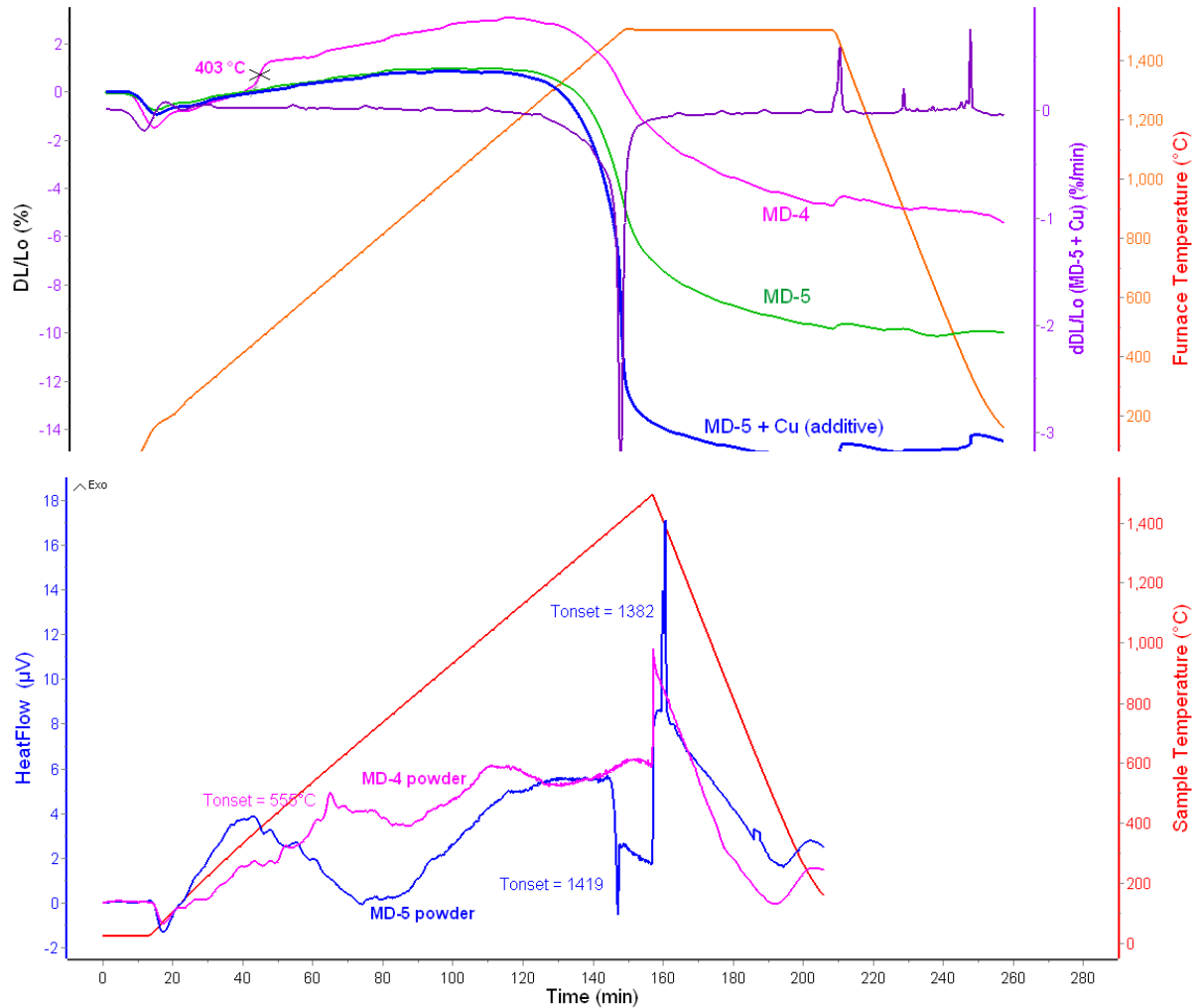
		Minimum		Maximum		
Alloy	Code	Sample	$[(\rho_f / \rho_{th}) 100] \%$	Code	Sample	$[(\rho_f / \rho_{th}) 100] \%$
L4	37	01	56.74	38	01	89.54
L4.1	07	01	60.92	02	01	78.89
L4Cu	25	01	63.66	25	01	63.66
L5	18	01	68.01	34	02	90.21
L5.1	32	01	74.69	41	02	98.54
L5Cu	27	01	69.35	31	02	90.77
L7	05	01	62.96	08	01	78.34
FN22	28	01	62.98	23	01	83.34

Source: own authorship (2023).

7.4.2 Dilatometry Results

[Fig. 59](#) shows the retraction profiles up to 1500 °C for both alloys together with the DSC curves.

Figure 59 - Dilatometric profiles up to 1500 °C under Ar-10%H₂; pellets form powdered L4 and L5 alloys with and without 3% Cu additive; retraction rate is also shown for L5Cu; below: Differential Scanning Calorimetry (DSC) curves for L4 and L5 powders.



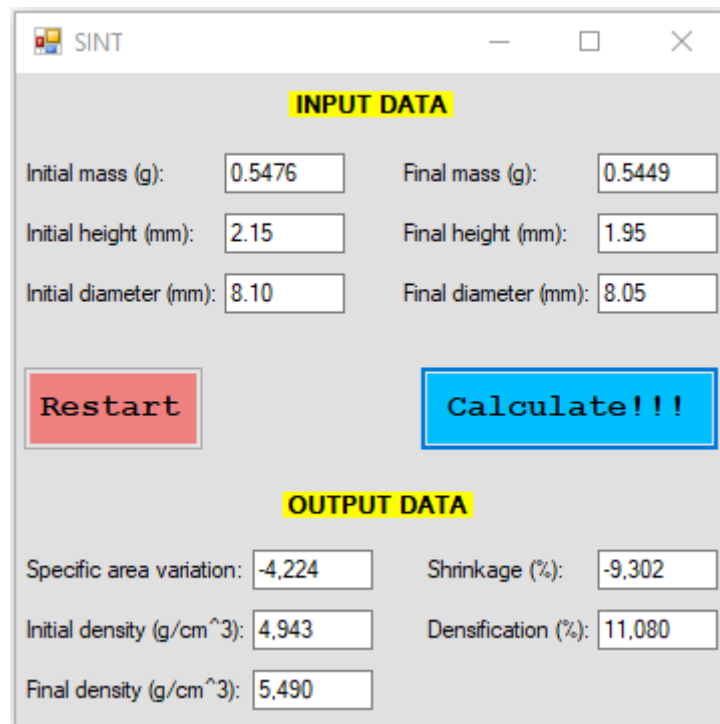
Source: own authorship (2022).

MD-4 (L4) alloy has shown marginal shrinkage, while MD-5 (L5) alloy has good sinterability up to 1500 °C. The shrinkage rate of MD-5 attains high values of -3 %/min (-85 $\mu\text{m}/\text{min}$) at 1490 °C. It can be seen at DSC curves that there is a melting peak for L5 powder at 1419 °C, followed by a solidification one at 1382 °C. Such peaks correspond to liquid phase formation already in the alloy, which explain the best sinterability of L5 powder even without Cu additive. On the other side, L4 has no clear melting peak, but conversely has an endothermic set of peaks indicating some phase is forming close to 558 °C, leading to sintering blockage thereafter.

7.4.3 Sintering results from SINT software

The results for the problem described in [Subsection 6.5](#) (referring to alloy code 20 from [Tab. 5](#)) are presented in [Fig. 60](#). The input data were inserted in the upper part of the interface in accordance with [Tab. 6](#) ([Subsection 6.6](#)). The blue “Calculate!!!” button was pressed and the results can be read in the lower part of the program window.

Figure 60 - Window of “SINT” with the results for the proposed problem.



The screenshot shows the SINT software window with the following data:

INPUT DATA	
Initial mass (g):	0.5476
Final mass (g):	0.5449
Initial height (mm):	2.15
Final height (mm):	1.95
Initial diameter (mm):	8.10
Final diameter (mm):	8.05

Buttons: Restart (red), Calculate!!! (blue)

OUTPUT DATA	
Specific area variation:	-4,224
Shrinkage (%):	-9,302
Initial density (g/cm ³):	4,943
Densification (%):	11,080
Final density (g/cm ³):	5,490

Source: own authorship (2022).

As can be observed in [Fig. 60](#), this compacted powder has specific area variation of -4.224%, an initial density of 4.943 g/cm^3 , a final density of 5.490 g/cm^3 , a linear shrinkage of -9.302%, and 11.080% of densification. A negative specific area variation (-4.224%) indicates a little tendency to densification, i.e. a body had a larger surface area before the sintering process and now has a smaller one (presents less porosity). When this information is associated with a negative increment measured in the mass and a positive increment in the cylinder volume after sintering, questions may arise about the densification effectiveness. Corroborating with the mass reduction, the negative calculated linear shrinkage corresponds to a reduction in cylinder height. The example here calculated is densified in a margin of 11.080%.

Given the results obtained, it may be feasible to use the SINT program to quantify and qualify the sintering process of other materials. The values presented herein can help in the decision-making process about sintering.

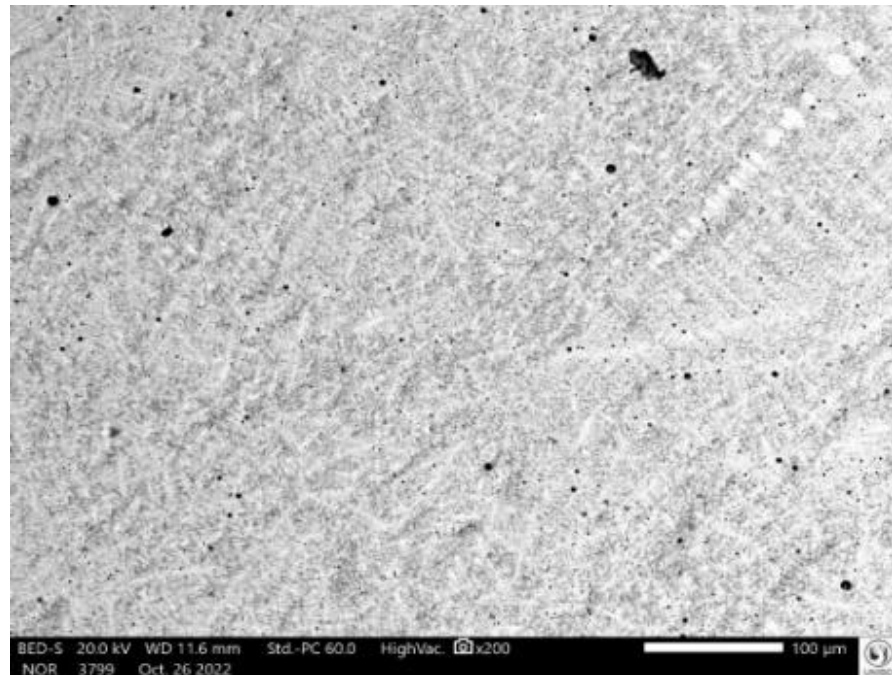
7.5 Scanning Electron Microscopy, Backscattered Electrons (SEM-BSE), and Energy-dispersive X-rays Spectrometer (DSC) Results

In the sequence, as-cast L4, L5, and L5.1 alloys, and sintered L4, L5, and L5.1 were subjected to SEM, BSE, and DSC presenting images related to their microstructures, chemical constitutions, and indentations. All the captured images are produced using 20 kV.

7.5.1 As-cast L4 alloy SEM-BSC results

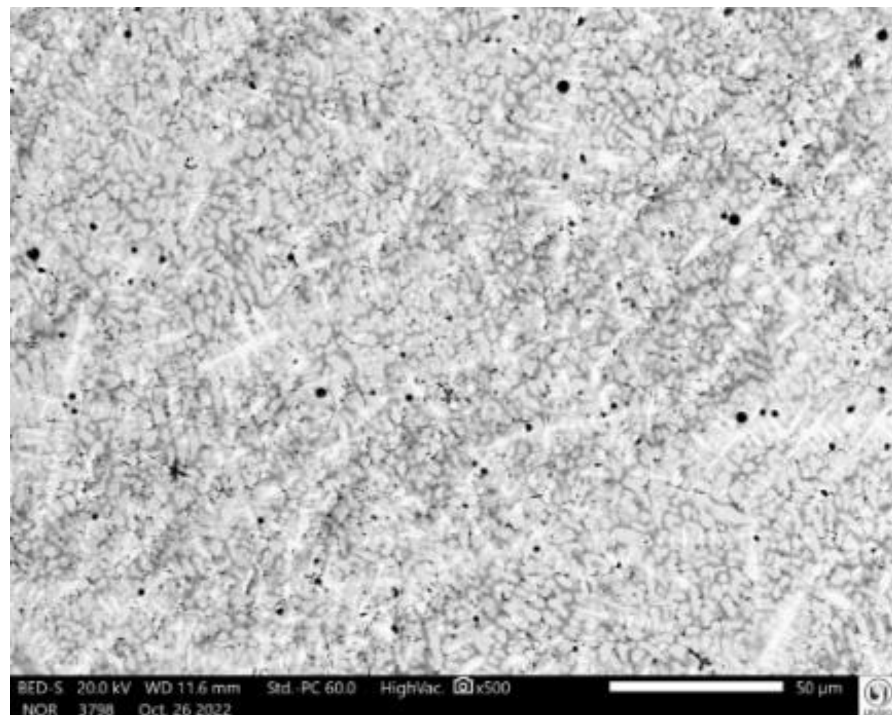
[Fig. 61](#), [Fig. 62](#), and [Fig. 63](#) show SEM-BSE results for as-cast L4 alloy (200x, 500x, and 1000x magnification, respectively). As the magnification increases, it is possible to observe two main contrast regions, in white and gray colors, that represent two distinct phases. The white phase is dendritic and is surrounded by the gray one (interdendritic). The minor region (in black nodules or droplets) is mainly constituted by titanium, also observed at some grain boundaries.

Figure 61 - As-cast L4 alloy SEM-BSE full-area: 200x magnification (trace scale 100 μm).



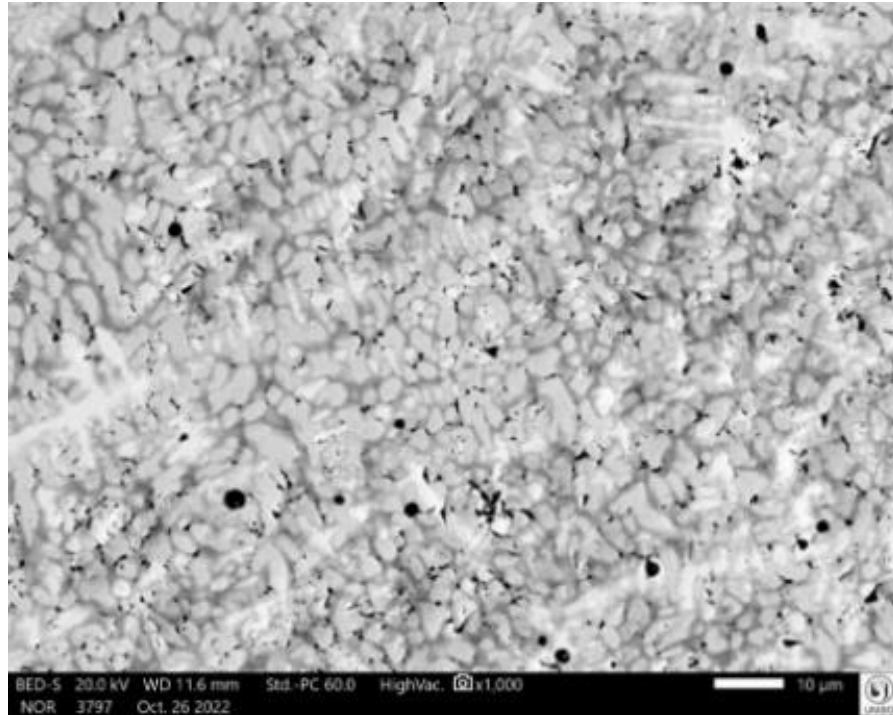
Source: own authorship (2022).

Figure 62 - As-cast L4 alloy SEM-BSE full-area: 500x magnification (trace scale 50 μm).



Source: own authorship (2022).

Figure 63 - (a) As-cast L4 alloy SEM-BSE full-area: 1000x magnification (trace scale 10 μm).



Source: own authorship (2022).

The white region has no defined shape and size, but represents the main area of the sample. It is randomly distributed all over the area of the sample. The gray region spreads along the contours of the white region, being slender in its form and adaptive to the white region delimitation. The black region seems to be nodular in its form and also randomly distributed over the sample area. All the phases are randomly found in a randomly picked sample region.

In what refers to the relationship between structure and properties, the typical grain shape is intended to provide hardness with moderate fracture toughness. The precipitate mean size is not considerable when compared to the pictorial microstructural parameters. Besides that, no apparent surface defects or voids were detected in the sample area analyzed.

[Tab. 14](#) brings out the minimum, maximum, and average grain size corresponding to the three distinct regions of the sample with 1000x magnification. These values were estimated via observation of the scale adopted in the SEM image at 1000x.

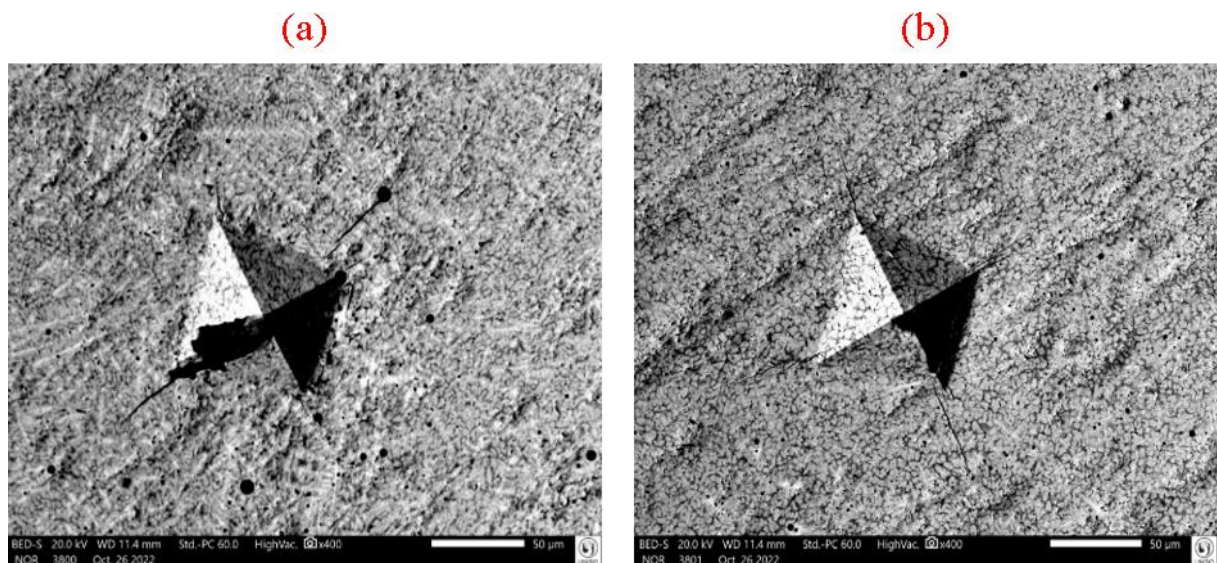
Table 14 - Minimum, maximum, and average grain sizes for L4 (1000x).

Region	Shape	Minimum grain size (μm)	Maximum grain size (μm)	Average grain size (μm)
White	Dendritic	2.00	20.00	11.00
Gray	Slender	1.00	30.00	15.50
Black	Nodular	0.50	3.00	1.75

Source: own authorship (2023).

[Fig. 64a](#), and [Fig. 64b](#) show two 400x magnified indentations made to measure L4 hardness. At indentation corners, cracks appear and commonly propagate until they find a titanium nodule. The extent of these cracks can be associated to the fracture toughness property by means of the existing theoretical and experimental background. The asymmetric indentations are probably due to either irregularities intrinsic to the process of grinding, or possible discrepancies in the process of inlaying the sample into the resin cylinder (misalignment between the resin that evolves the alloy sample and the upper surface of the sample). In addition, each indentation is produced in a random orientation in what refers to the grains because there is not a fixed orientation for the indentations, and the grains are randomly disposed.

Figure 64 - As-cast L4 alloy SEM-BSE, 400x magnific. (trace scale 50 μm): (a) 1st; (b) 2nd indentation.

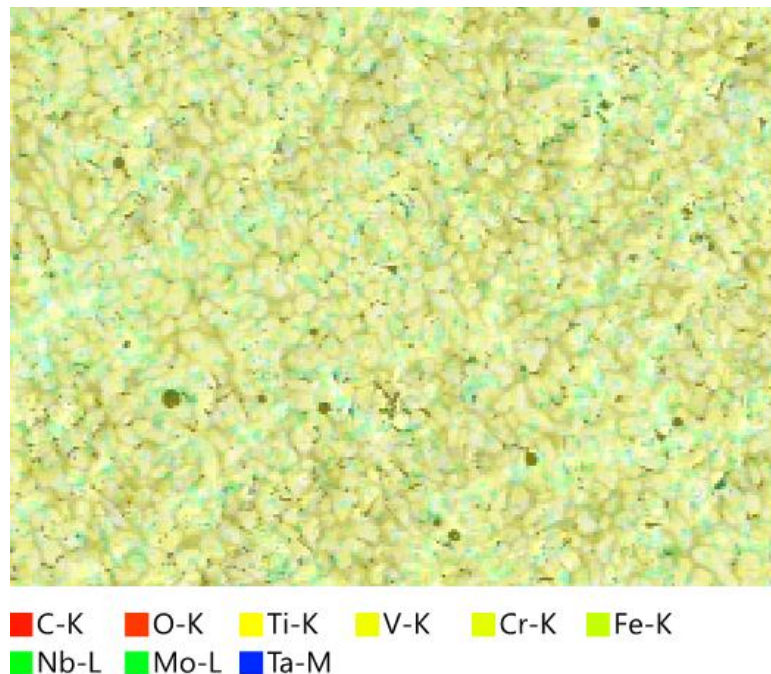


Source: own authorship (2022).

The composition of L4 alloy comprises iron, niobium, molybdenum, tantalum, titanium, chrome, vanadium, and traces of carbon, silicon and oxygen. This can be observed in [Fig. 65](#), [Fig. 66](#), [Fig. 67](#), [Fig. 68](#), [Fig. 69](#), and [Fig. 70](#).

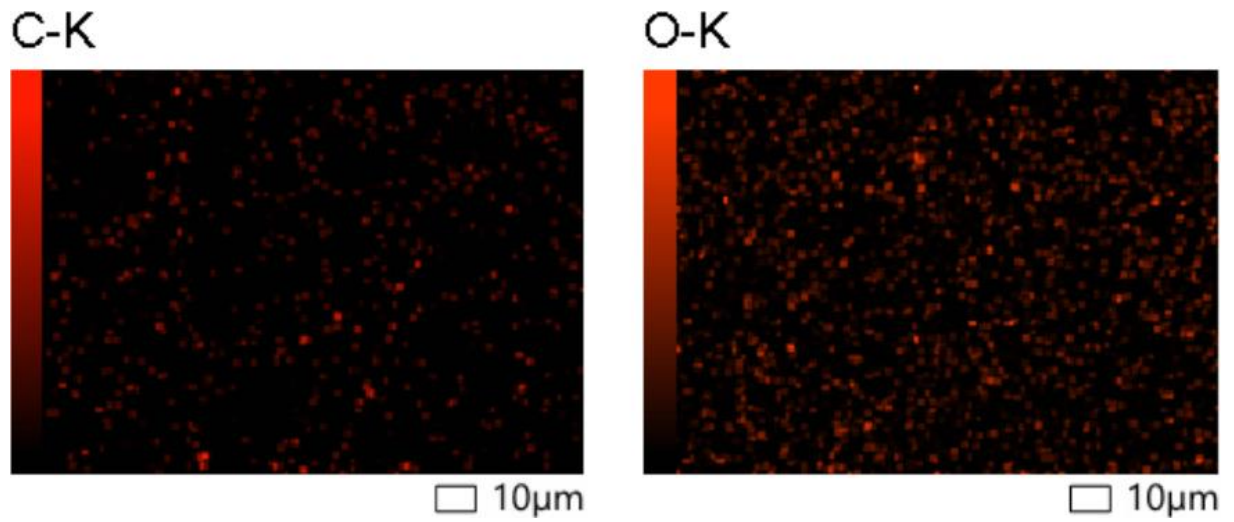
The experimentally obtained chemical composition of L4 alloy and its theoretical composition deviate probably due to the specific points picked, i.e. in these points the experimental composition does not agree with the theoretical one. To each chemical element, a tone of color is attributed in [Fig. 65](#), besides the location of the element in the sample area.

Figure 65 - As-cast L4 alloy SEM-BSE: Energy Dispersive Spectroscopy (EDS) map.



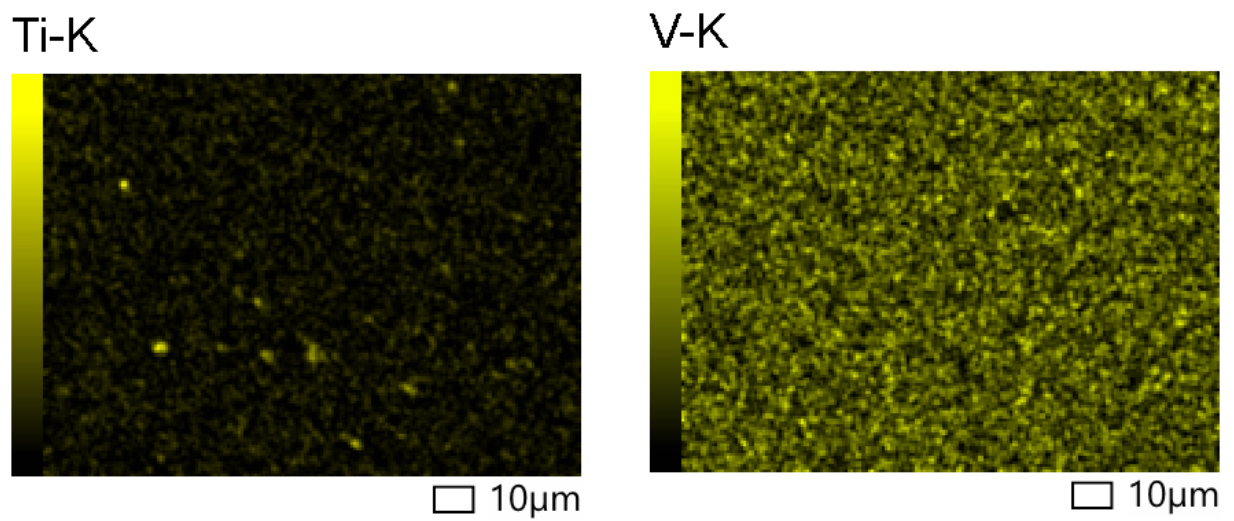
Source: own authorship (2022).

Figure 66 - As-cast L4 alloy SEM-BSE: EDS element maps of carbon and oxygen.



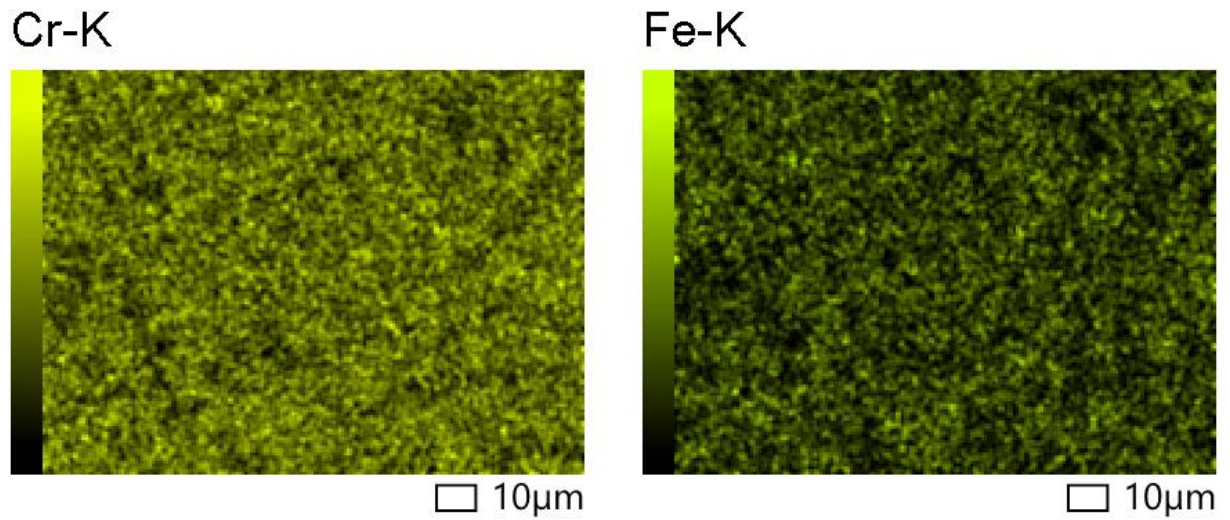
Source: own authorship (2022).

Figure 67 - As-cast L4 alloy SEM-BSE: EDS element maps of titanium and vanadium.



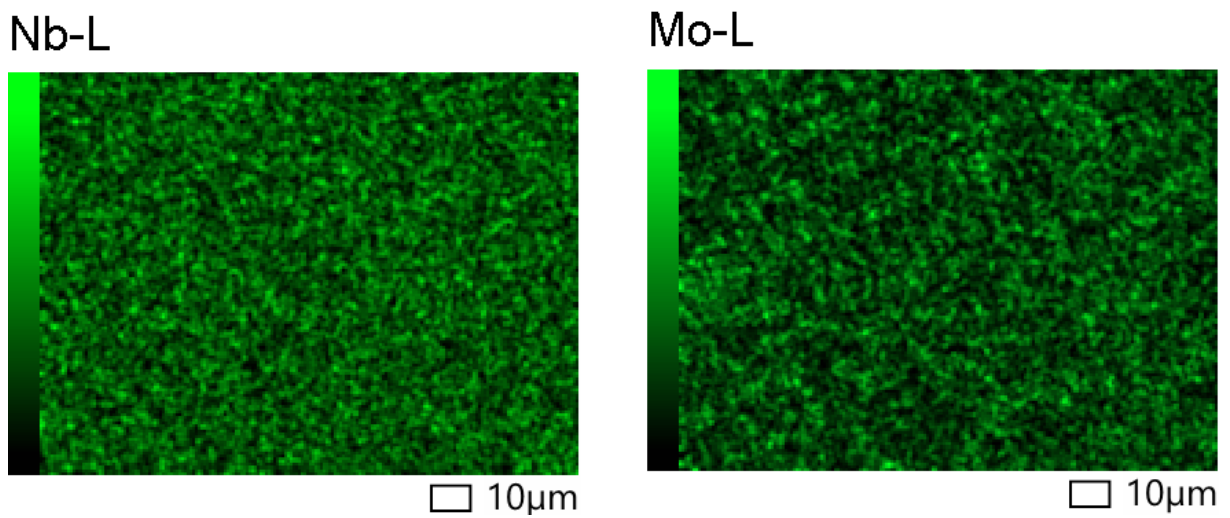
Source: own authorship (2022).

Figure 68 - As-cast L4 alloy SEM-BSE: EDS element maps of chrome and iron.



Source: own authorship (2022).

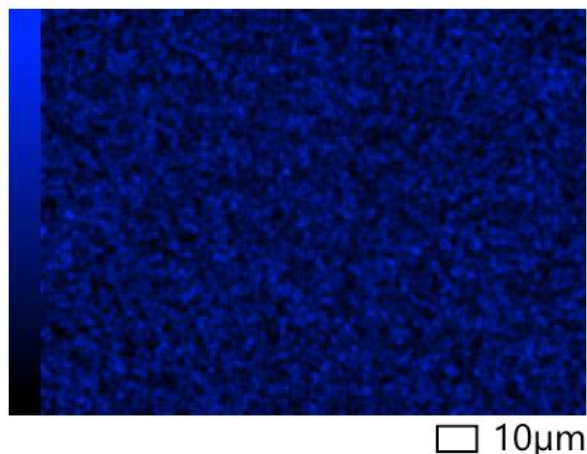
Figure 69 - As-cast L4 alloy SEM-BSE: EDS element maps of niobium and molybdenum.



Source: own authorship (2022).

Figure 70 - As-cast L4 alloy SEM-BSE: EDS element map of tantalum.

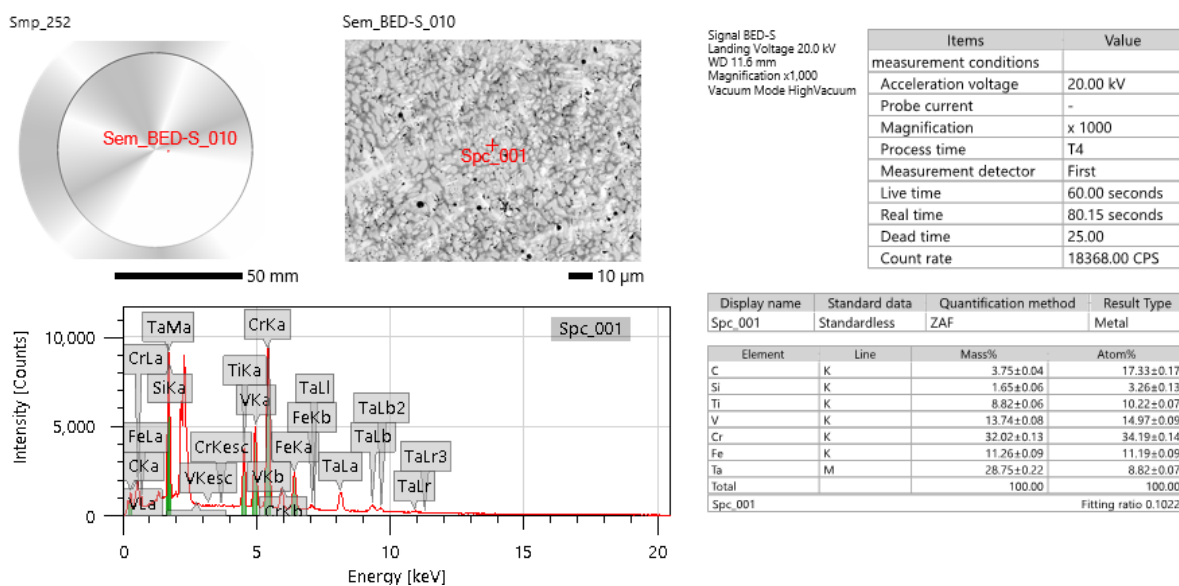
Ta-M



Source: own authorship (2022).

At one of the white points, as per [Fig. 71](#), the chemical composition is as follows (atomic %): carbon (17.33 ± 0.17), silicon (3.26 ± 0.13), titanium (10.22 ± 0.07), vanadium (14.97 ± 0.09), chrome (34.19 ± 0.14), iron (11.19 ± 0.09), and tantalum (8.82 ± 0.07).

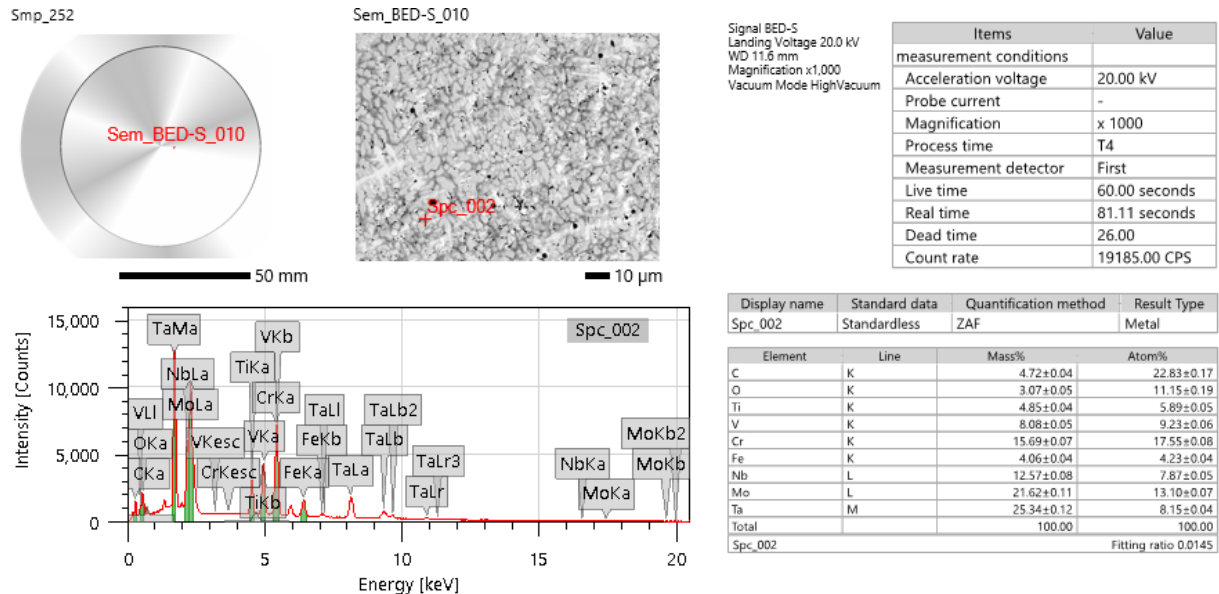
Figure 71 - As-cast L4 alloy SEM-BSE: Chemical composition of one of the white points.



Source: own authorship (2022).

[Fig. 72](#) presents the chemical composition (also in atomic %) in the gray regions: carbon (22.83 ± 0.17), oxygen (11.15 ± 0.19), titanium (5.89 ± 0.05), vanadium (9.23 ± 0.06), chrome (17.55 ± 0.08), iron (4.23 ± 0.04), niobium (7.87 ± 0.05), molybdenum (13.10 ± 0.07), and tantalum (8.15 ± 0.04).

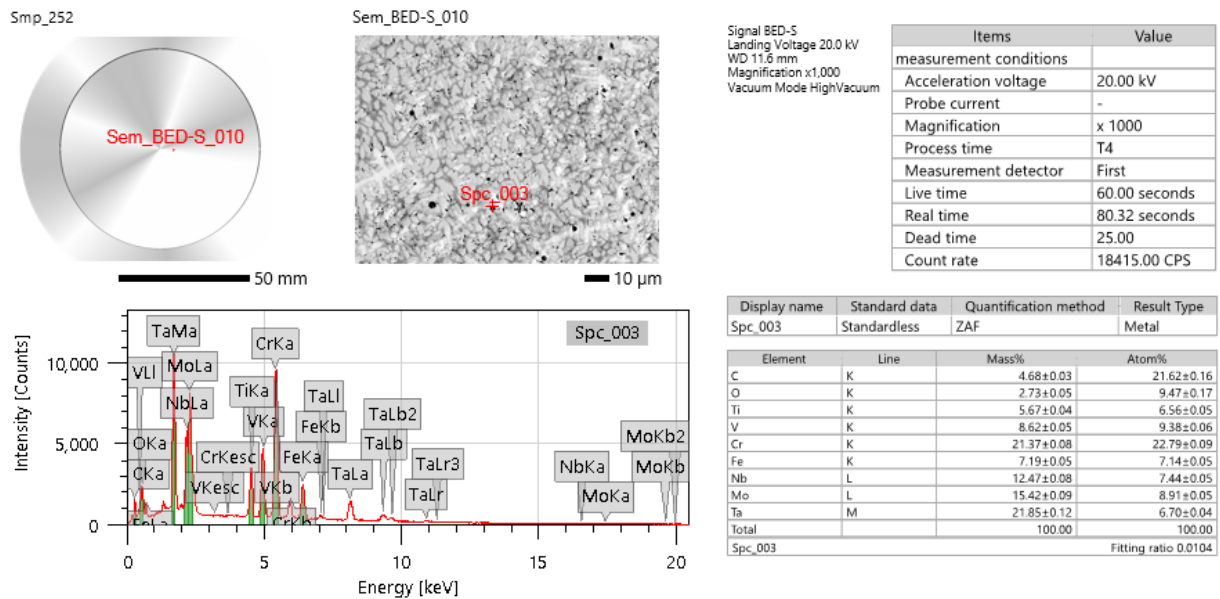
Figure 72 - As-cast L4 alloy SEM-BSE: Chemical composition of one of the gray points.



Source: own authorship (2022).

In addition, the black regions are probably composed by the following chemical elements (in atomic %), as per [Fig. 73](#): carbon (21.62 ± 0.16), oxygen (9.47 ± 0.17), titanium (6.56 ± 0.05), vanadium (9.38 ± 0.06), chrome (22.79 ± 0.09), iron (7.14 ± 0.05), niobium (7.44 ± 0.05), molybdenum (8.91 ± 0.05), and tantalum (6.70 ± 0.04).

Figure 73 - As-cast L4 alloy SEM-BSE: Chemical composition of one of the black points.



Source: own authorship (2022).

[Tab. 15](#) shows the compositions of the distinct regions before and after the carbon and oxygen normalization for L4 alloy. The results are close to the theoretical composition of the alloy, 33.34 for Cr and 11.11 at.% for Fe and the other components.

Table 15 - Composition before and after carbon and oxygen normalization for L4 alloy.

		Before C and O normalization			After C and O normalization		
Element	Theoretical atomic %	Experimental white region atomic %	Experimental gray region atomic %	Experimental black region atomic %	Experimental white region atomic %	Experimental gray region atomic %	Experimental black region atomic %
C	0.00	17.33	22.83	21.62	0.00	0.00	0.00
Cr	33.34	34.19	17.55	22.79	41.35	25.60	32.12
Fe	11.11	11.19	4.23	7.14	13.54	6.17	10.06
Mo	11.11	0.00	13.10	8.91	0.00	19.11	12.56
Nb	11.11	0.00	7.87	7.44	0.00	11.48	10.48
O	0.00	0.00	11.15	9.47	0.00	0.00	0.00
Si	0.00	3.26	0.00	0.00	3.94	0.00	0.00
Ta	11.11	8.82	8.15	6.70	10.67	11.89	9.44
Ti	11.11	10.22	5.89	6.56	12.36	8.59	9.25
V	11.11	14.97	9.23	9.23	18.11	13.04	13.01

Source: own authorship (2023).

[Tab. 16](#) compiles the comparison between theoretical and experimental values in atomic percentage composition for L4 alloy before carbon and oxygen normalization.

Table 16 - Comparison between theoretical and experimental chemical composition for L4 alloy before carbon and oxygen normalization in the three distinct regions.

Element	Theoretical atomic %	Experimental white region atomic %	Absolute value of relative error %	Experimental gray region atomic %	Absolute value of relative error %	Experimental black region atomic %	Absolute value of relative error %
C	0.00	17.33	NA	22.83	NA	21.62	NA
Cr	33.34	34.19	2.50	17.55	47.36	22.79	31.64
Fe	11.11	11.19	0.72	4.23	61.93	7.14	35.73
Mo	11.11	0.00	NA	13.10	17.91	8.91	19.80
Nb	11.11	0.00	NA	7.87	29.16	7.44	33.03
O	0.00	0.00	0.00	11.15	NA	9.47	NA
Si	0.00	3.26	NA	0.00	0.00	0.00	0.00
Ta	11.11	8.82	20.61	8.15	26.64	6.70	39.69
Ti	11.11	10.22	8.01	5.89	46.98	6.56	40.95
V	11.11	14.97	34.74	9.23	16.92	9.23	16.92

Source: own authorship (2023).

[Tab. 17](#) establishes the comparison between theoretical and experimental values in atomic percentage composition for L4 alloy after carbon and oxygen normalization.

Table 17 - Comparison between theoretical and experimental chemical composition for L4 alloy after carbon and oxygen normalization in the three distinct regions.

Element	Theoretical atomic %	Experimental white region atomic %	Absolute value of relative error %	Experimental gray region atomic %	Absolute value of relative error %	Experimental black region atomic %	Absolute value of relative error %
C	0.00	0.00	NA	0.00	0.00	0.00	NA
Cr	33.34	40.81	22.41	25.60	23.22	32.12	3.66
Fe	11.11	13.36	20.25	6.17	44.46	10.06	9.45
Mo	11.11	0.00	NA	19.11	72.00	12.56	13.05
Nb	11.11	0.00	NA	11.48	3.33	10.48	5.67
O	0.00	0.00	0.00	0.00	0.00	0.00	0.00
Si	0.00	3.89	NA	0.00	0.00	0.00	0.00
Ta	11.11	10.53	5.22	11.89	7.02	9.44	15.03
Ti	11.11	12.20	9.81	8.59	22.68	9.25	16.74
V	11.11	17.87	60.85	13.04	17.37	13.01	17.10

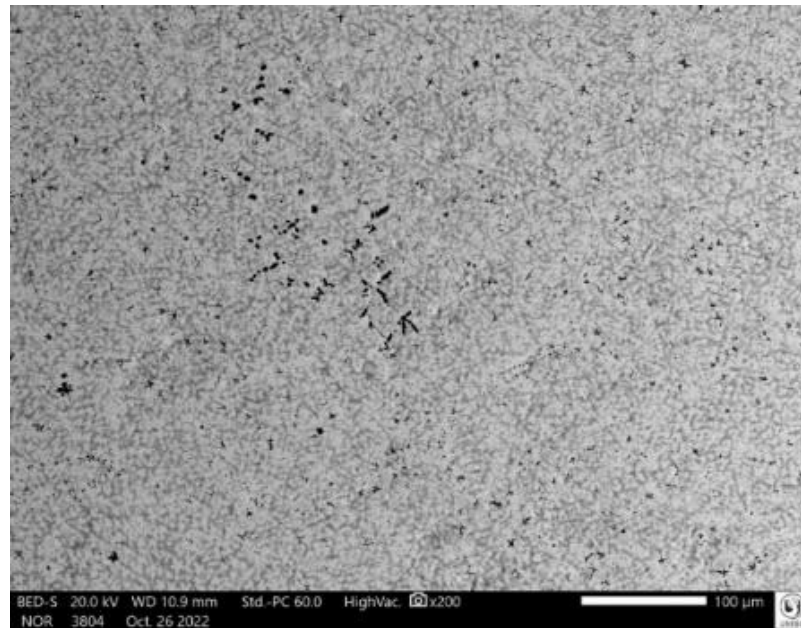
Source: own authorship (2023).

The high values of the relative errors between the theoretical composition and the one obtained via SEM-BSE are partially explained by the fact that the points collected in the sample are not representative of each described region (white, gray, and black points). The reason they are not representative comes from three peculiarities: (a) the possible sample region (a square of $10 \times 10 \text{ mm}$) itself is big compared to the sample area ($80 \times 100 \mu\text{m}$); (b) the points randomly picked have composition that probabilistically mismatches; (c) in reality, the point is a small area, and therefore, this small picked area can be partially picked in the desired region and simultaneously collected in one or more neighboring regions. Moreover, after carbon and oxygen normalization, the absolute value of the relative errors decreased.

7.5.2 As-cast L5 alloy SEM-BSE results

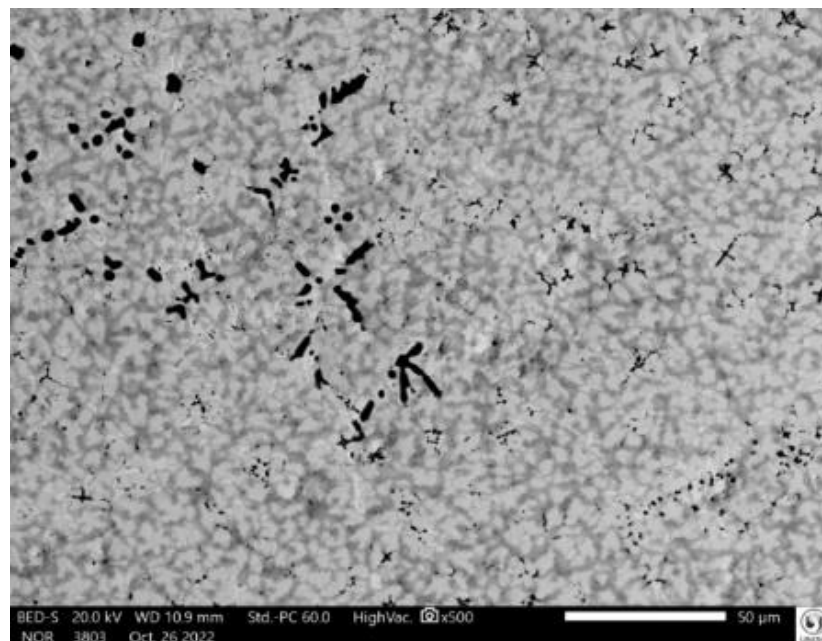
The results for as-cast L5 alloy SEM-BSE (200x, 500x, and 1000x magnification, respectively) are shown in [Fig. 74](#), [Fig. 75](#), and [Fig. 76](#). Two phases with dispersed black precipitates are present in L5. The precipitates of titanium (in black) are within one phase in white, and the other in gray.

Figure 74 - As-cast L5 alloy SEM-BSE: 200x magnification (trace scale 100 μm).



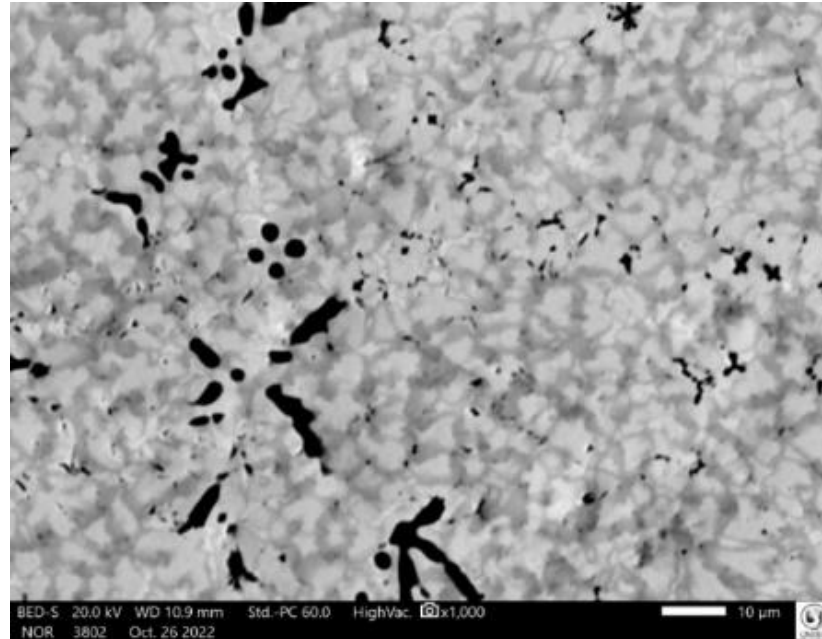
Source: own authorship (2022).

Figure 75 - As-cast L5 alloy SEM-BSE: 500x magnification (trace scale 50 μm).



Source: own authorship (2022).

Figure 76 - As-cast L5 alloy SEM-BSE: 1000x magnification (trace scale 10 μm).



Source: own authorship (2022).

The white phase is the matrix in which the gray phase is within, being representative in the sample. The gray phase has a slender form and its adaptability fulfills the room between the white regions. White and gray phases are randomly found in the sample surface. The black regions are concentrated in some regions of the sample and vary in their form, prevailing the dendritic one.

L5 microstructure provided hardnesses lower than L4 and it seems that it is reflected in more nodular grains of L5. Most of the titanium dendrites have considerable dimensions when compared to the white and gray phases. Moreover, no surface defects or voids were observed at the sample surface. Similarly to L4 ([Tab. 14](#)), the minimum, maximum, and average grain size related to the regions of the sample with 1000x magnification are shown in [Tab. 18](#) for L5. The magnitudes shown were based on observation of the scale adopted in the SEM image at its highest magnification.

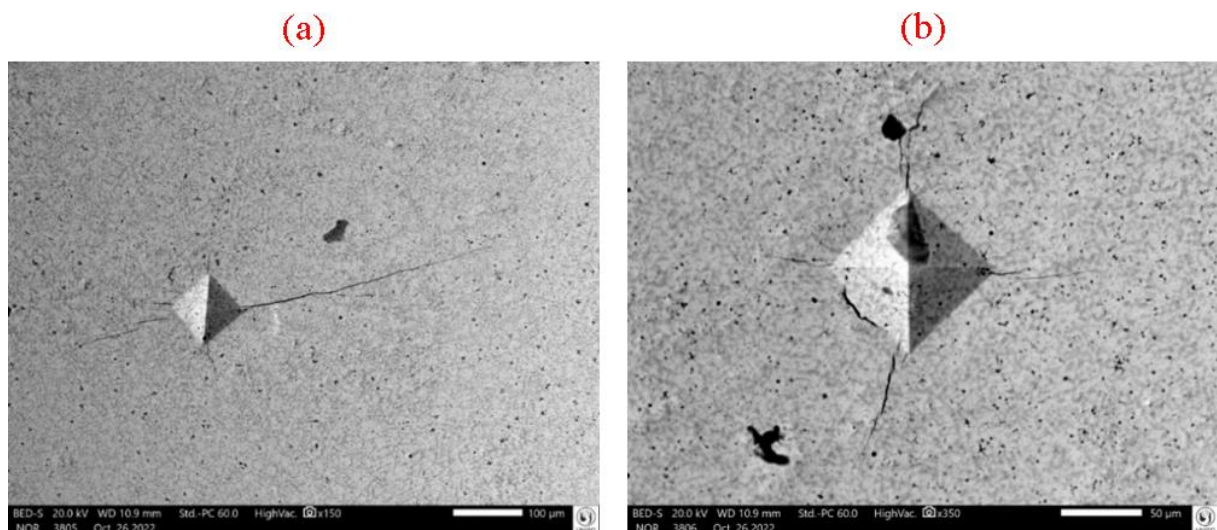
Table 18 - Minimum, maximum, and average grain sizes for L5 (1000x).

Region	Shape	Minimum grain size (μm)	Maximum grain size (μm)	Average grain size (μm)
White	Random	4.00	25.00	14.50
Gray	Slender	3.00	20.00	11.50
Black	Random	0.50	15.00	7.75

Source: own authorship (2023).

[Fig. 77a](#) and [Fig. 77b](#) show two indentations, one 150x-magnified, and the other 350x-magnified, which are produced to measure L5 hardness. Their indentation corners originate cracks, which commonly propagate until they find a titanium precipitate. By applying theoretical and empirical formulations, it is possible to calculate the fracture toughness based on the crack length. The asymmetry in the indentations is possibly related to either inherent irregularities in the grinding process or non-parallelism between the lower plane of the resin cylinder and the metallic plane of the sample. Moreover, the two indentations shown are randomly made with respect to the orientation of the grains.

Figure 77 - As-cast L5 alloy SEM-BSE indentations: (a) 1st: 150x magnification (trace scale 100 μm); (b) 2nd: 350x (trace scale 50 μm).

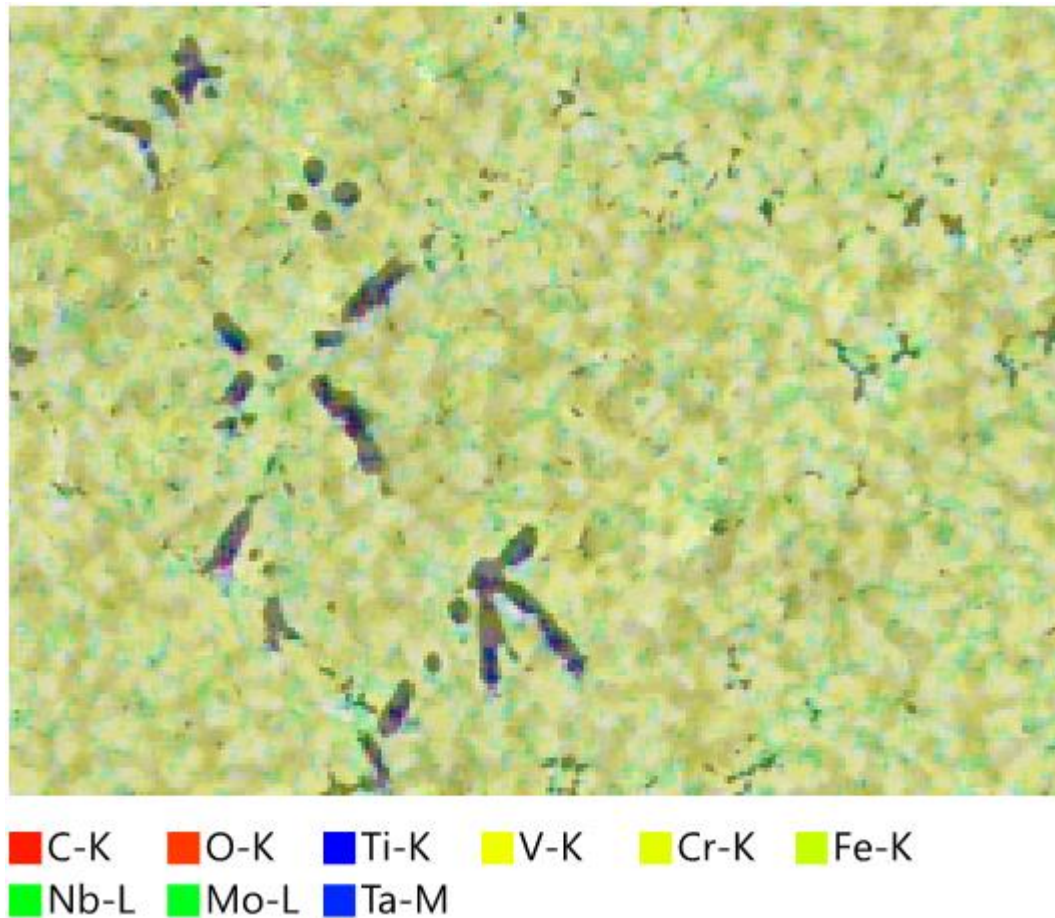


Source: own authorship (2022).

The composition of L5 alloy encompasses iron, niobium, molybdenum, tantalum, titanium, chrome, vanadium, and traces of carbon, sulphur, nitrogen, and

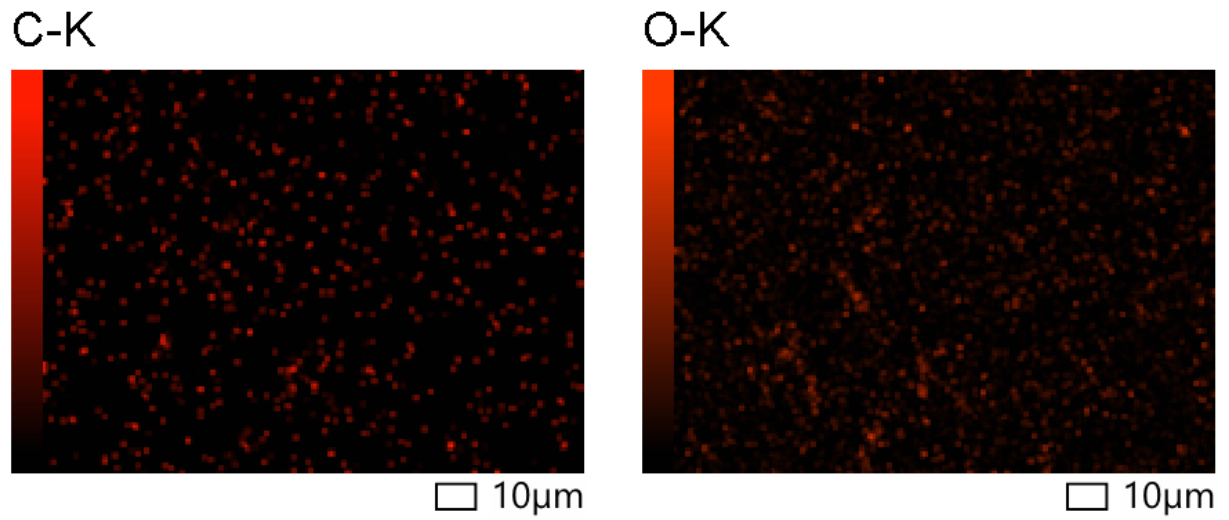
oxygen. The chemical compositions are in [Fig. 78](#), [Fig. 79](#), [Fig. 80](#), [Fig. 81](#), [Fig. 82](#). , and [Fig. 83](#). [Fig. 78](#) shows the tones of the colors that represent each chemical element involved in the production of the referred alloy, and the location of the element in the sample area.

Figure 78 - As-cast L5 alloy SEM-BSE: Energy Dispersive Spectroscopy (EDS) map.



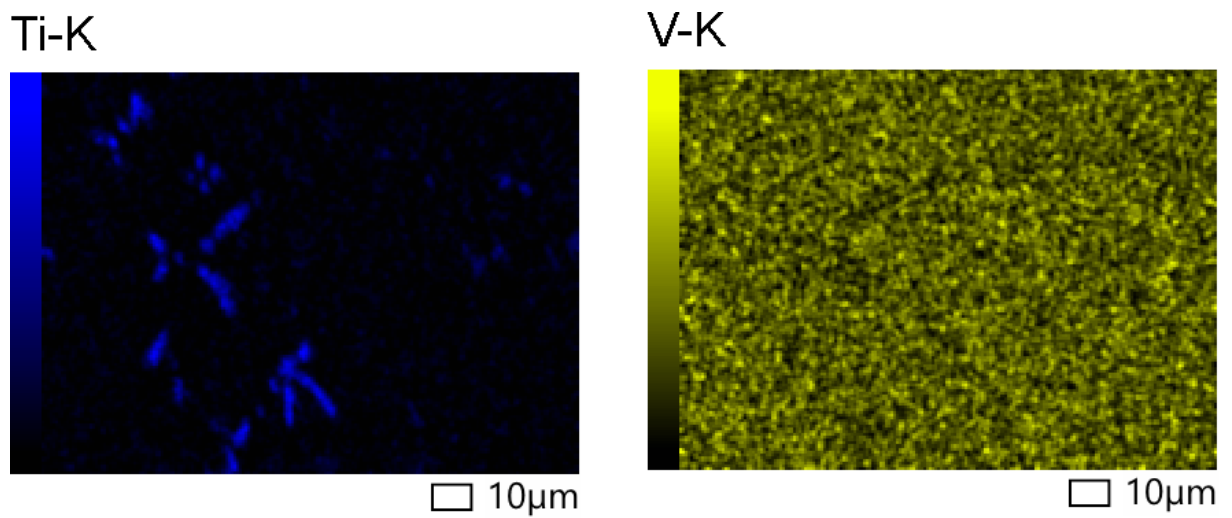
Source: own authorship (2022).

Figure 79 - As-cast L5 alloy SEM-BSE: EDS element maps for carbon and oxygen.



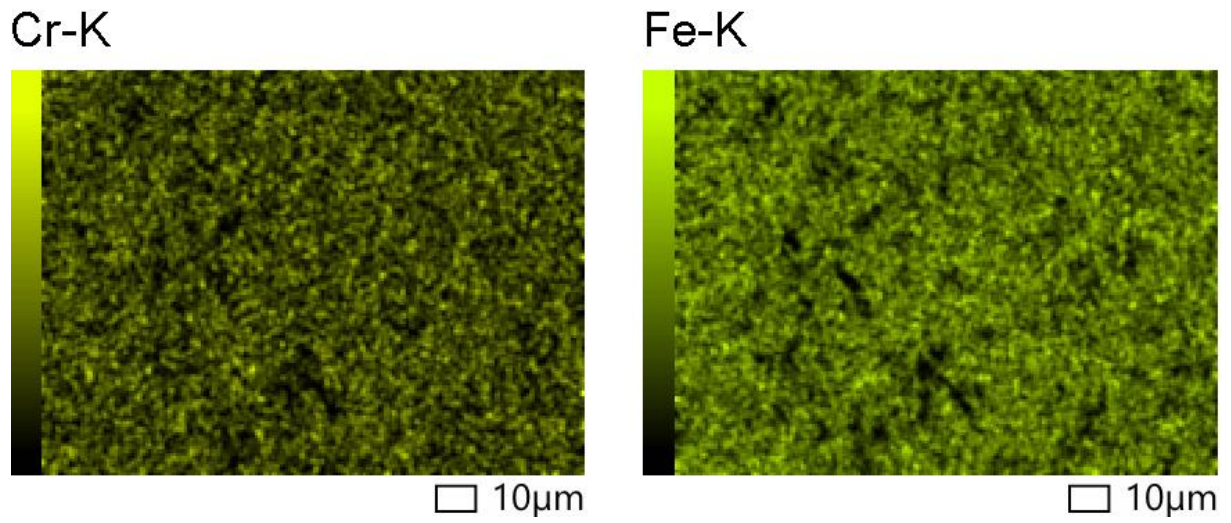
Source: own authorship (2022).

Figure 80 - As-cast L5 alloy SEM-BSE: EDS element maps for titanium and vanadium.



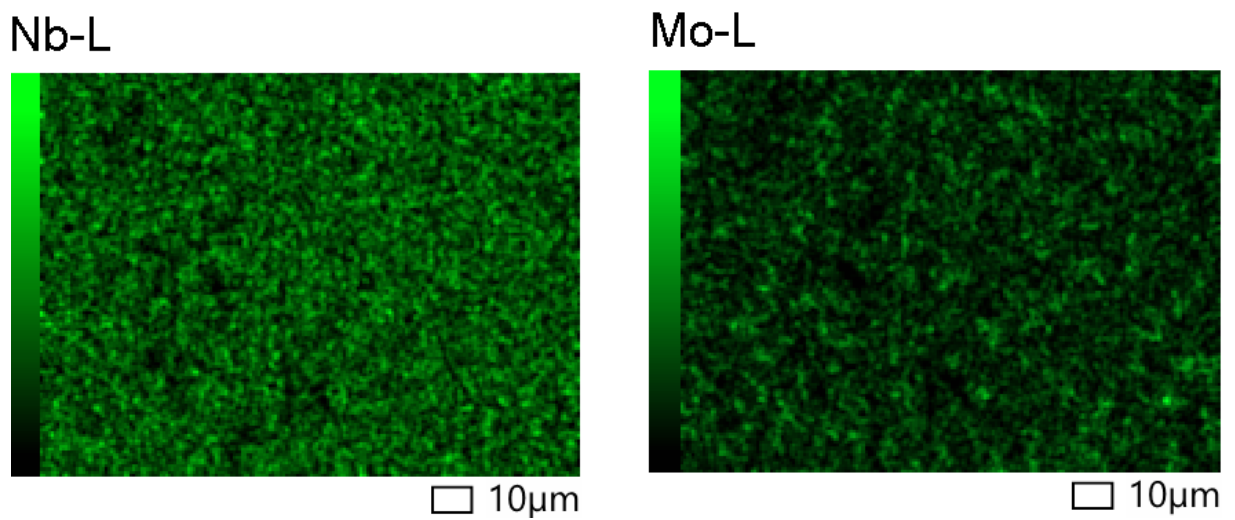
Source: own authorship (2022).

Figure 81 - As-cast L5 alloy SEM-BSE: EDS element maps for chrome and iron.



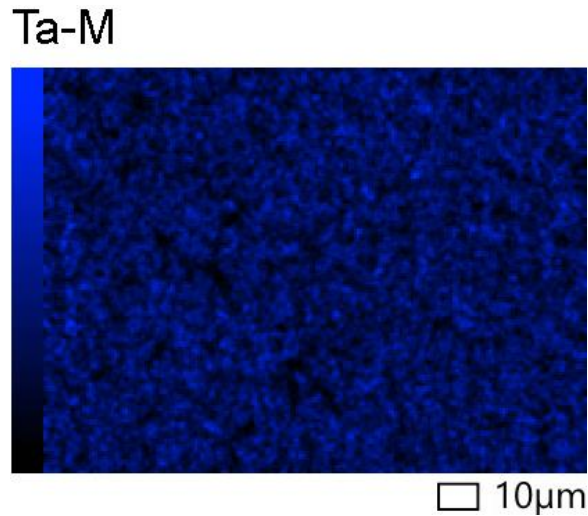
Source: own authorship (2022).

Figure 82 - As-cast L5 alloy SEM-BSE: EDS element maps for niobium and molybdenum.



Source: own authorship (2022).

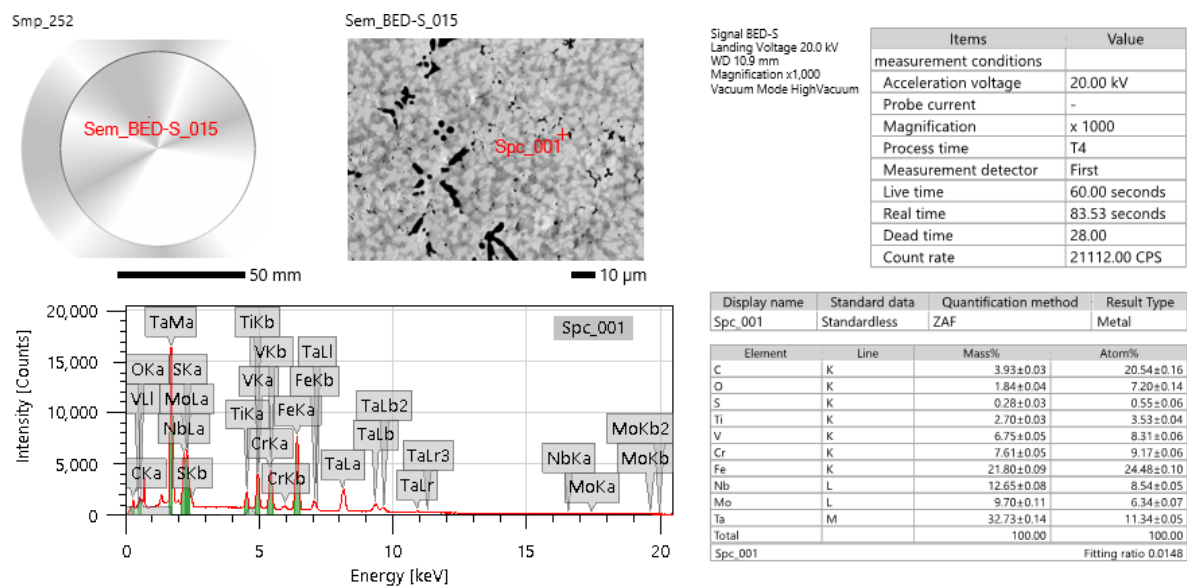
Figure 83 - As-cast L5 alloy SEM-BSE: EDS element map for tantalum.



Source: own authorship (2022).

The chemical composition at one of the white points of L5 alloy, as per [Fig. 84](#), is as follows (in atomic %): carbon (20.54 ± 0.16), oxygen (7.20 ± 0.14), sulphur (0.55 ± 0.06), titanium (3.53 ± 0.04), vanadium (8.31 ± 0.06), chrome (9.17 ± 0.06), iron (24.48 ± 0.10), niobium (8.54 ± 0.05), molybdenum (6.34 ± 0.07), and tantalum (11.34 ± 0.05).

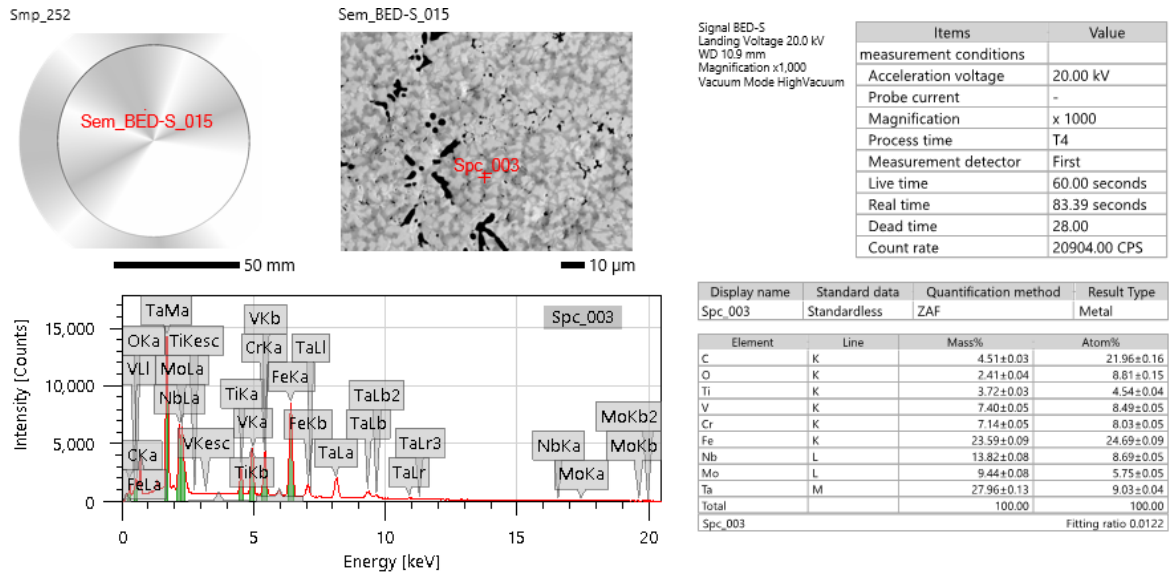
Figure 84 - As-cast L5 alloy SEM-BSE: Chemical composition of one of the white points.



Source: own authorship (2022).

[Fig. 85](#) presents the chemical composition (also in atomic %) in the gray regions: carbon (21.96 ± 0.16), oxygen (8.81 ± 0.15), titanium (4.54 ± 0.04), vanadium (8.49 ± 0.05), chrome (8.03 ± 0.05), iron (24.69 ± 0.09), niobium (8.69 ± 0.05), molybdenum (5.75 ± 0.05), and tantalum (9.03 ± 0.04).

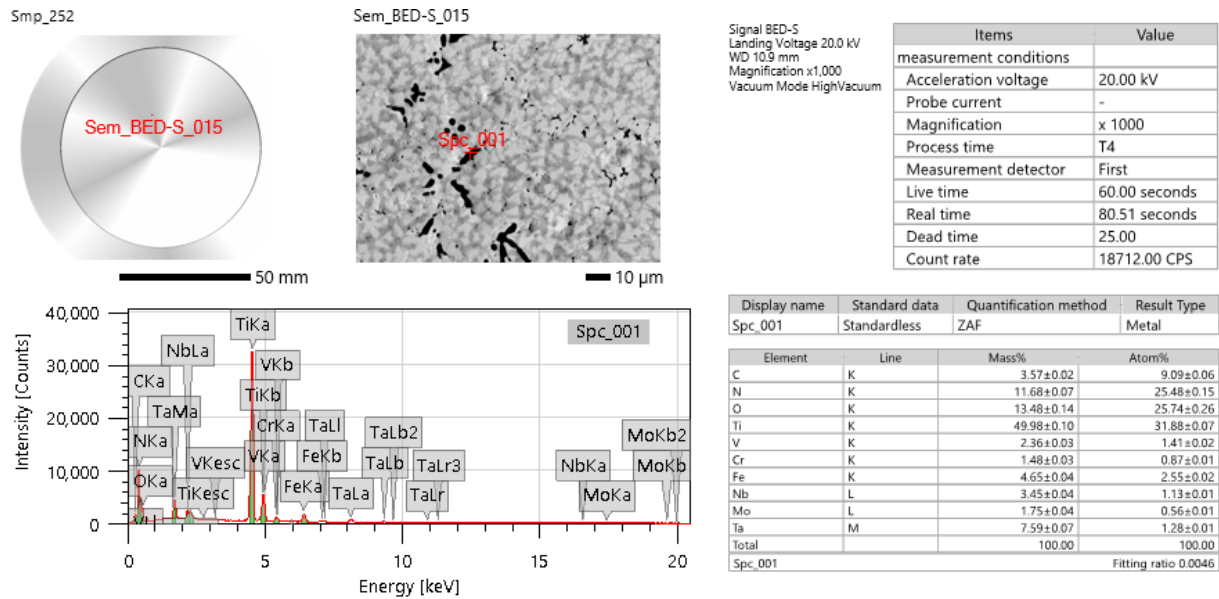
Figure 85 - As-cast L5 alloy SEM-BSE: Chemical composition of one of the gray points.



Source: own authorship (2022).

The black regions of L5 alloy are composed by the chemical elements (in atomic %, [Fig. 86](#)): carbon (9.09 ± 0.06), nitrogen (25.48 ± 0.15), oxygen (25.74 ± 0.26), titanium (31.88 ± 0.07), vanadium (1.41 ± 0.02), chrome (0.87 ± 0.01), iron (2.55 ± 0.02), niobium (1.13 ± 0.01), molybdenum (0.56 ± 0.01), and tantalum (1.28 ± 0.01).

Figure 86 - As-cast L5 alloy SEM-BSE: Chemical composition of one of the black points.



Source: own authorship (2022).

The compositions of the three regions before and after the carbon and oxygen normalization for L5 alloy are shown in [Tab. 19](#).

Table 19 - Composition before and after carbon and oxygen normalization for L5 alloy.

		Before C and O normalization			After C and O normalization		
Element	Theoretical atomic %	Experimental white region atomic %	Experimental gray region atomic %	Experimental black region atomic %	Experimental white region atomic %	Experimental gray region atomic %	Experimental black region atomic %
C	0.00	20.54	21.96	9.09	0.00	0.00	0.00
Cr	11.11	9.17	8.03	0.87	11.54	10.29	1.33
Fe	33.34	24.48	24.69	2.55	30.81	31.64	3.89
Mo	11.11	6.34	5.75	0.56	7.98	7.37	0.86
Nb	11.11	8.54	8.69	1.13	10.75	11.14	1.72
O	0.00	0.00	0.00	25.48	0.00	0.00	0.00
Si	0.00	7.20	8.81	25.74	9.06	11.29	39.33
Ta	0.00	0.55	0.00	0.00	0.69	0.00	0.00
Ti	11.11	11.34	9.03	1.28	14.27	11.57	1.96
V	11.11	3.53	4.54	31.88	4.44	5.82	48.73

Source: own authorship (2023).

[Tab. 20](#) establishes the comparison between theoretical and experimental values of atomic percentage composition for L5 alloy before carbon and oxygen normalization.

Table 20 - Comparison between theoretical and experimental chemical composition for L5 alloy before carbon and oxygen normalization in the three phases.

Element	Theoretical atomic %	Experimental white region atomic %	Absolute value of relative error %	Experimental gray region atomic %	Absolute value of relative error %	Experimental black region atomic %	Absolute value of relative error %
Carbon	0.00	20.54	NA	21.96	NA	9.09	NA
Chrome	11.11	9.17	17.46	8.03	27.72	0.87	92.17
Iron	33.34	24.48	26.57	24.69	25.94	2.55	92.35
Molybdenum	11.11	6.34	42.93	5.75	48.24	0.56	95.00
Niobium	11.11	8.54	23.13	8.69	21.78	1.13	89.83
Oxygen	0.00	0.00	0.00	0.00	0.00	25.48	NA
Silicon	0.00	7.20	NA	8.81	NA	25.74	NA
Tantalum	0.00	0.55	NA	0.00	NA	0.00	NA
Titanium	11.11	11.34	2.07	9.03	18.72	1.28	88.48
Vanadium	11.11	3.53	68.23	4.54	40.86	31.88	186.95

Source: own authorship (2023).

[Tab. 21](#) compares the theoretical and experimental values of atomic percentage composition for L5 alloy after carbon and oxygen normalization.

Table 21 - Comparison between theoretical and experimental chemical compositions for L5 alloy after carbon and oxygen normalization in the three phases.

Element	Theoretical atomic %	Experimental white region atomic %	Absolute value of relative error %	Experimental gray region atomic %	Absolute value of relative error %	Experimental black region atomic %	Absolute value of relative error %
C	0.00	0.00	NA	0.00	NA	0.00	0.00
Cr	11.11	11.54	3.87	10.29	7.38	1.33	88.03
Fe	33.34	30.81	7.59	31.64	5.10	3.89	88.33
Mo	11.11	7.98	28.17	7.37	33.66	0.86	92.26
Nb	11.11	10.75	3.24	11.14	0.27	1.72	84.52
O	0.00	0.00	0.00	0.00	0.00	0.00	0.00
Si	0.00	9.06	NA	11.29	NA	39.33	NA
Ta	0.00	0.69	NA	0.00	NA	0.00	0.00
Ti	11.11	14.27	28.44	11.57	4.14	1.96	82.36
V	11.11	4.44	60.04	5.82	47.61	48.73	338.61

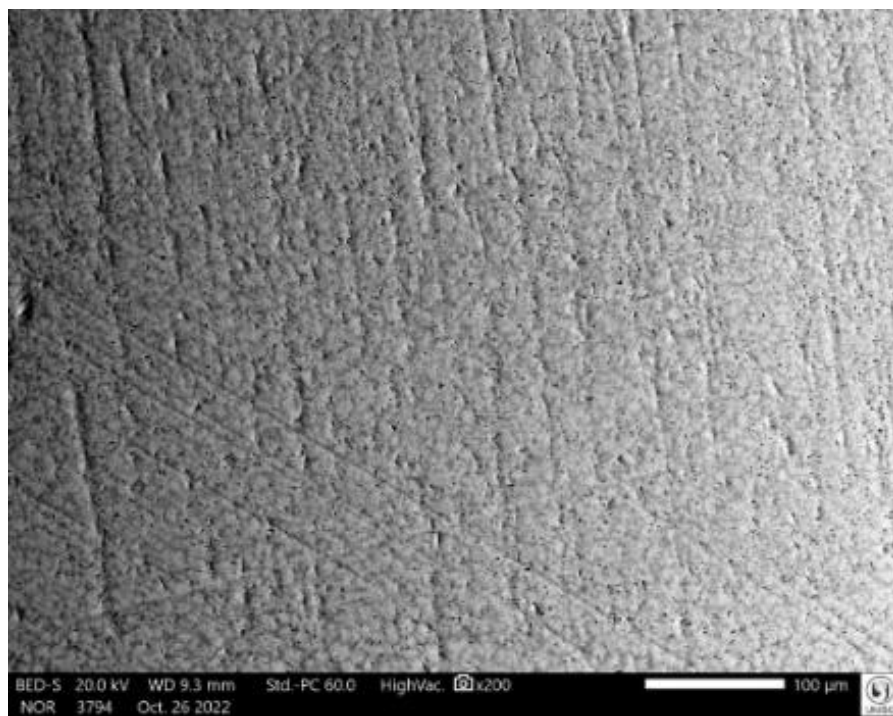
Source: own authorship (2023).

Theoretical and SEM-BSE compositions present high values of discrepancy. This is partially due to the points collected in the sample, which may be not representative of each described phase. As explained in [Subsection 7.5.1](#), the collected points are not representative because: (a) the sample area checked ($80 \times 100 \mu\text{m}$ in 1000x), compared to the total area of the sample (a square of $15 \times 15 \text{ mm}$), is small; (b) the compositions of the picked points diverge because the points are randomly taken; and (c) as the point is a small area, if the picked area is in the limit of another neighboring phase(s), then the intended composition is not achieved in SEM-BSE analysis. In addition, in most of the cases, the absolute value of the relative errors decreased after carbon and oxygen normalization.

7.5.3 As-cast L5.1 alloy SEM-BSE results

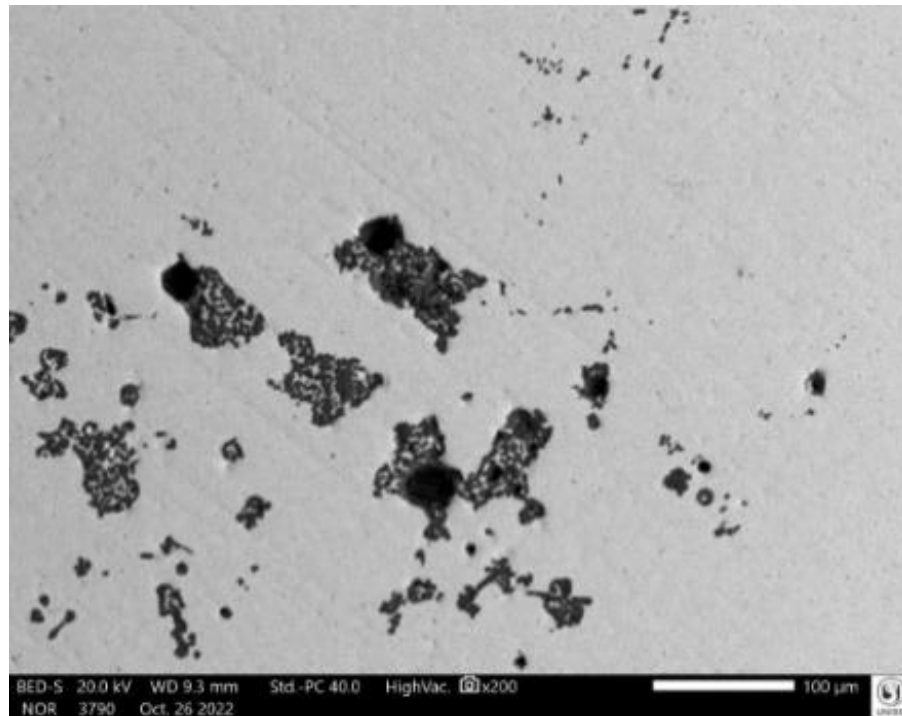
The SEM-BSE results for as-cast L5.1 alloy (200x, 200x, 500x, 1000x, and 3500x magnification, respectively) are shown in [Fig. 87](#), [Fig. 88](#), [Fig. 89](#), [Fig. 90](#) and [Fig. 91](#). In the last one ([Fig. 91](#)), two main contrast regions can be noted. Two distinct phases are represented: one in white, and the other in gray color, which corresponds to aluminum oxide (Al_2O_3). In the region mapped in [Fig. 91](#), the interdendritic phase (white) surrounds the dendritic phase (gray). The minor black regions, with distinct forms, are mainly constituted by titanium, which is also observed at some grain boundaries.

Figure 87 - As-cast L5.1 alloy 1st SEM-BSE: 200x magnification (trace scale 100 μm).



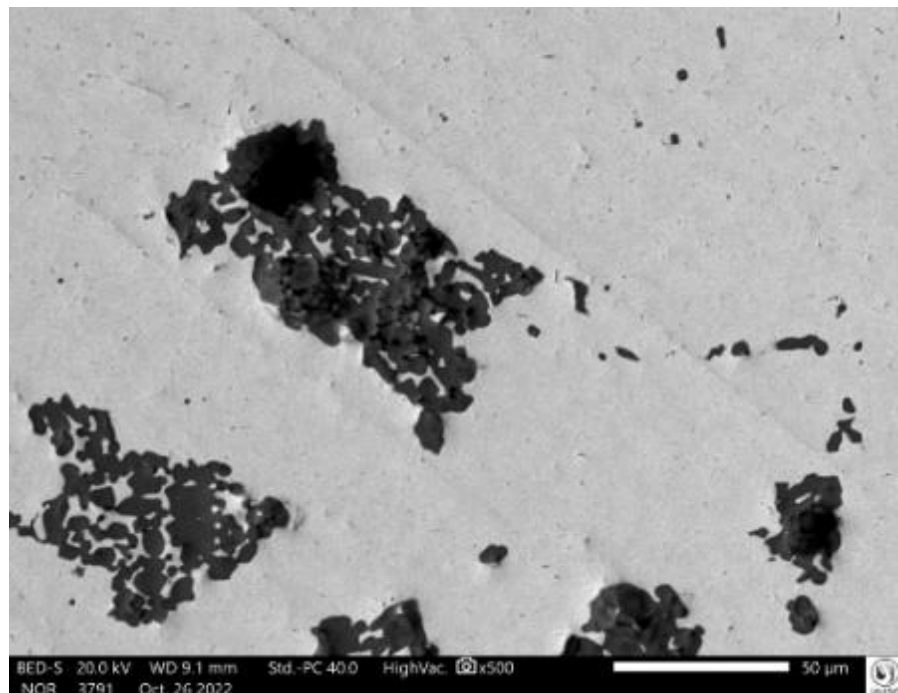
Source: own authorship (2022).

Figure 88 - As-cast L5.1 alloy 2nd SEM-BSE: 200x magnification (trace scale 100 μm).



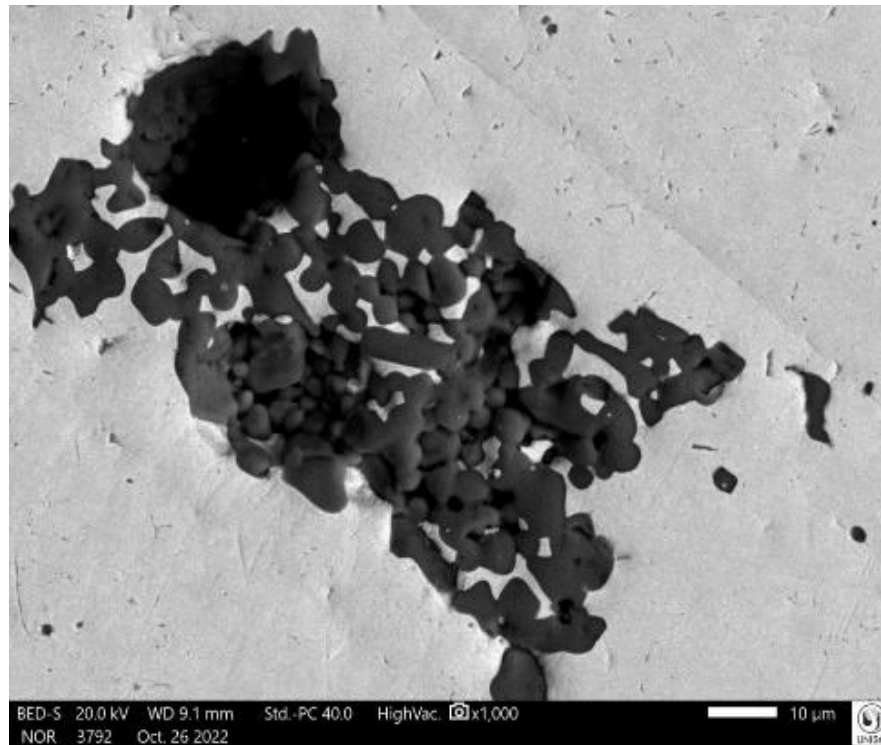
Source: own authorship (2022).

Figure 89 - As-cast L5.1 alloy SEM-BSE: 500x magnification (trace scale 50 μm).



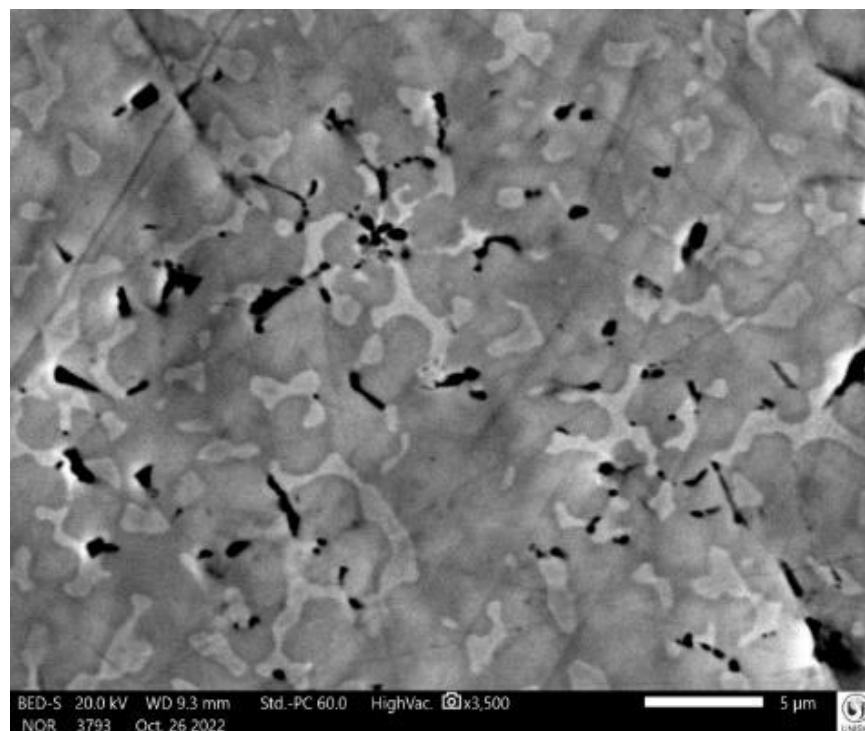
Source: own authorship (2022).

Figure 90 - As-cast L5.1 alloy SEM-BSE: 1000x magnification (trace scale 10 μm).



Source: own authorship (2022).

Figure 91 - As-cast L5.1 alloy SEM-BSE: 3500x magnification (trace scale 5 μm).



Source: own authorship (2022).

According to [Fig. 90](#), the white region is the most representative. However, an almost nodular form defines both gray and black regions. As can be observed in [Fig. 91](#), the area of the sample is predominantly gray, which shape and size are random. Its coarseness and preponderance turns white region into a dendritic one and reduces the black region to a minimum.

In view of [Fig. 87](#), [Fig. 88](#), and [Fig. 89](#), each precipitate varies in its shape and size, commonly placed at the grain boundaries. Moreover, the existence of apparent surface defects or voids were not apparently detected in the sample area analyzed.

According to the region, shape, minimum, maximum, and average grain sizes are presented in [Tab. 22](#) related to [Fig. 91](#), corresponding to the sample with 3500x magnification. These values were predicted by observing the scale adopted in the SEM image at 3500x.

Table 22 - Shape, minimum, maximum, and average grain size by region (3500x).

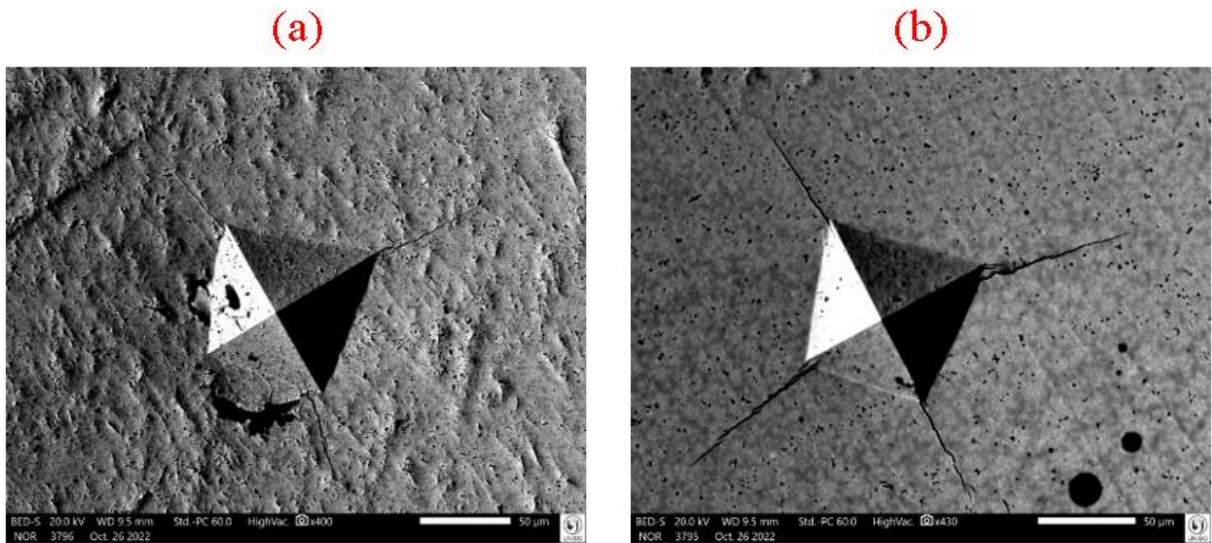
Region	Shape	Minimum grain size (μm)	Maximum grain size (μm)	Average grain size (μm)
White	Slender	0.50	6.00	3.25
Gray	Diverse	2.00	11.00	6.50
Black	Slender	0.30	4.00	2.15

Source: own authorship (2023).

[Fig. 92a](#) and [Fig. 92b](#) show two indentations over the surface of L5.1, one 400x-magnified, and the other 430x-magnified. Their indentation corners originate cracks, which commonly propagate until they find a titanium precipitate. The asymmetric indentations are probably explained by inherent irregularities in the process of grinding the upper surface of the sample or the lower surface of it. Moreover, each indentation is performed at a random orientation related to the grinding direction.

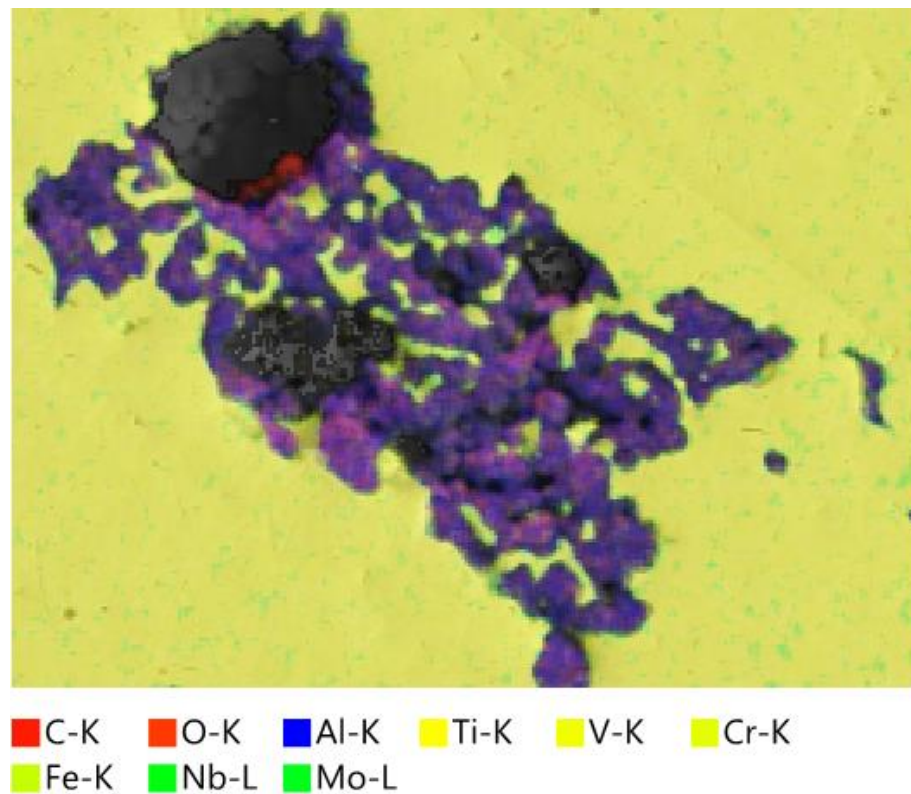
The composition of the L5.1 alloy includes aluminum, titanium, vanadium, chrome, iron, niobium, molybdenum, and traces of carbon, oxygen, and sulphur. The chemical compositions can be observed in [Fig. 93](#), [Fig. 94](#), [Fig. 95](#), [Fig. 96](#), [Fig. 97](#), and [Fig. 98](#).

Figure 92 - As-cast L5.1 alloy SEM-BSE indentations (trace scale 50 μm): (a) 1st. 400x magnification; 2nd 430x magnification.



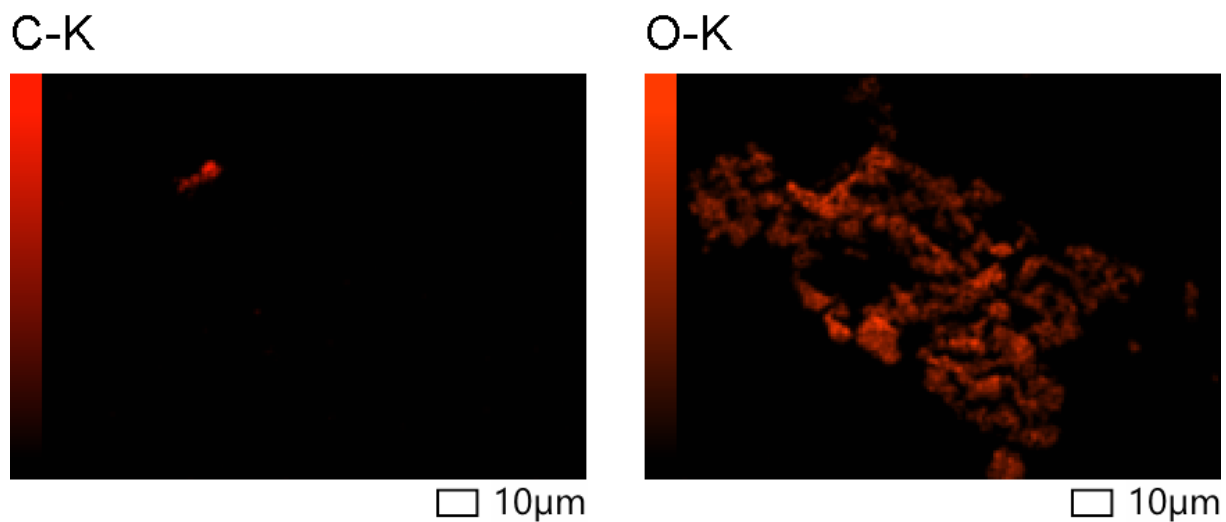
Source: own authorship (2022).

Figure 93 - As-cast L5.1 alloy SEM-BSE: Energy Dispersive Spectroscopy (EDS) map.



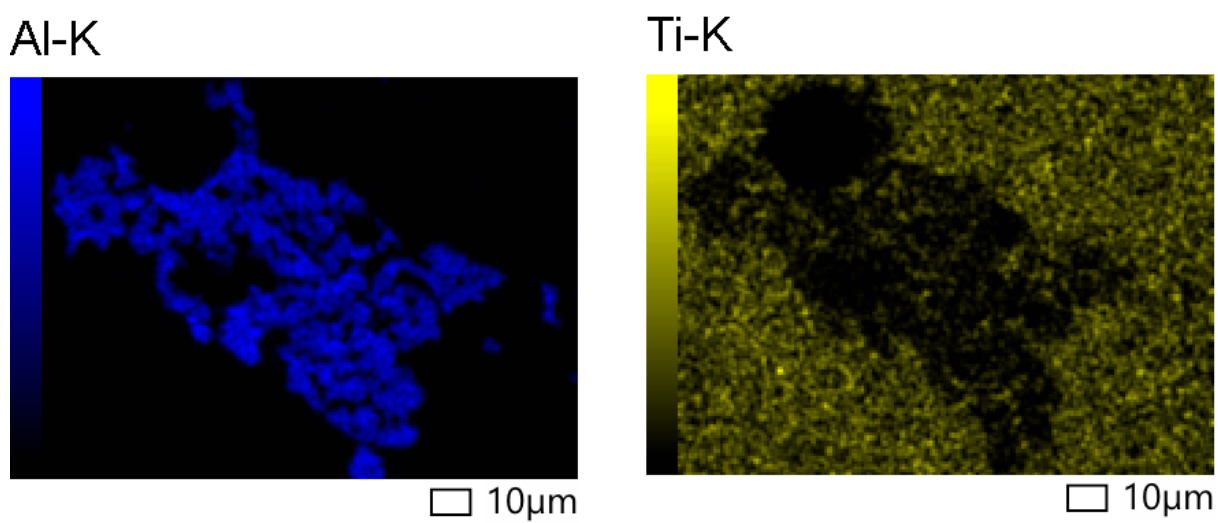
Source: own authorship (2022).

Figure 94 - As-cast L5.1 alloy SEM-BSE: EDS element maps for carbon and oxygen.



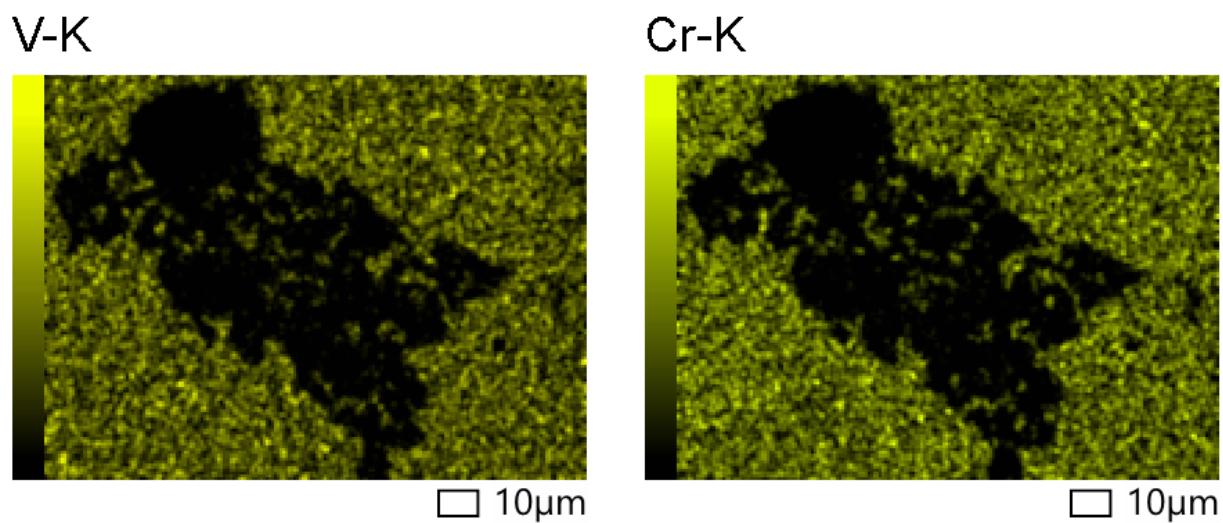
Source: own authorship (2022).

Figure 95 - As-cast L5.1 alloy SEM-BSE: EDS element maps for aluminum and titanium.



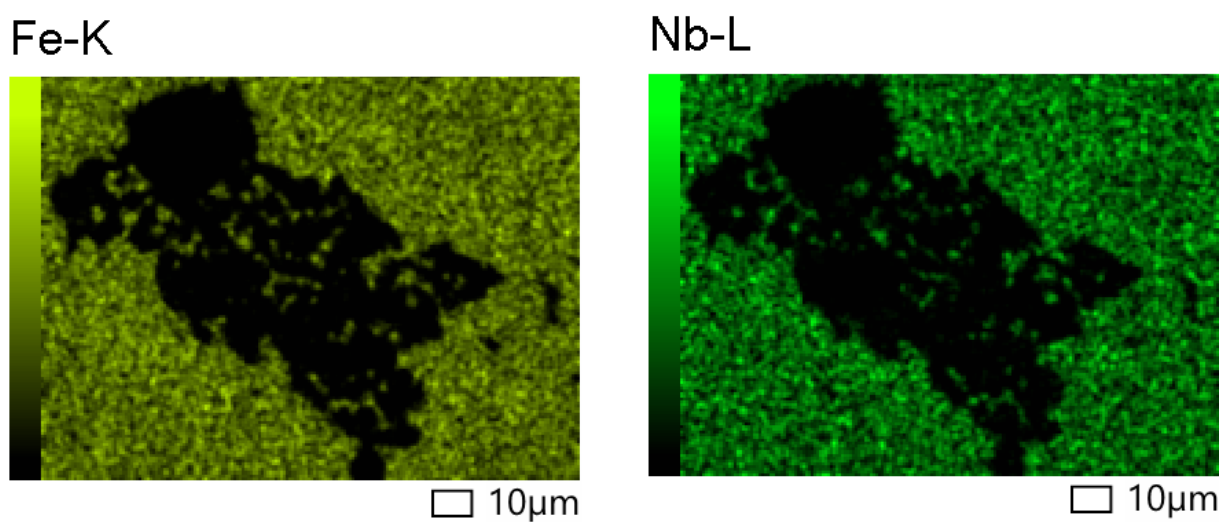
Source: own authorship (2022).

Figure 96 - As-cast L5.1 alloy SEM-BSE: EDS element maps for vanadium and chrome.



Source: own authorship (2022).

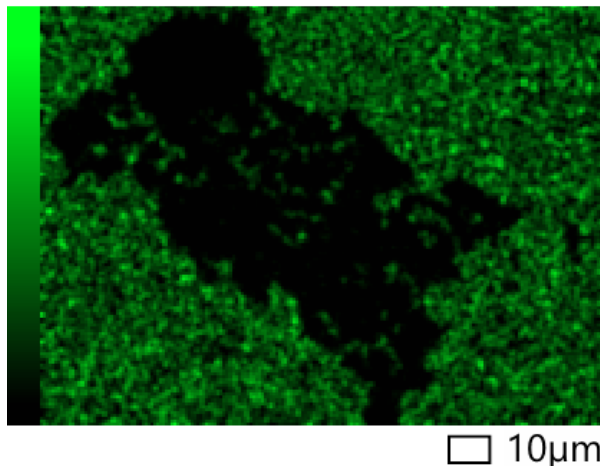
Figure 97 - As-cast L5.1 alloy SEM-BSE: EDS element maps for iron and niobium.



Source: own authorship (2022).

Figure 98 - As-cast L5.1 alloy SEM-BSE: EDS element map for molybdenum.

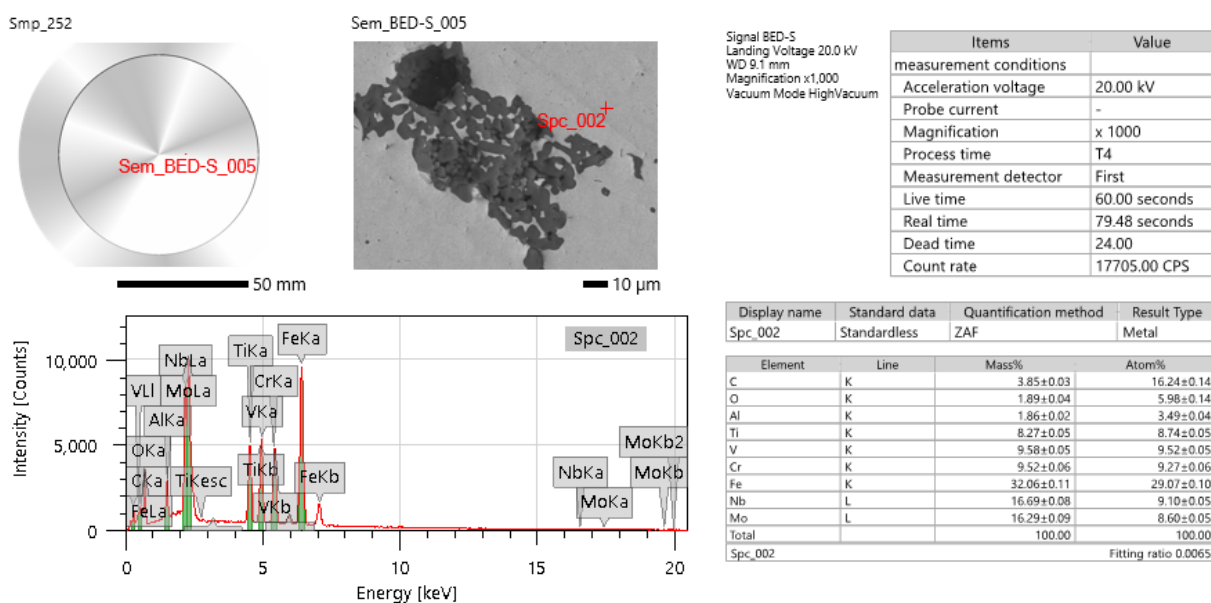
Mo-L



Source: own authorship (2022).

One of the white points of the L5.1 alloy presents the following chemical composition (in atomic %), as per [Fig. 99](#): carbon (16.24 ± 0.14), oxygen (5.98 ± 0.14), aluminum (3.49 ± 0.04), titanium (8.74 ± 0.05), vanadium (9.52 ± 0.05), chrome (9.27 ± 0.06), iron (29.07 ± 0.10), niobium (9.10 ± 0.05), and molybdenum (8.60 ± 0.05).

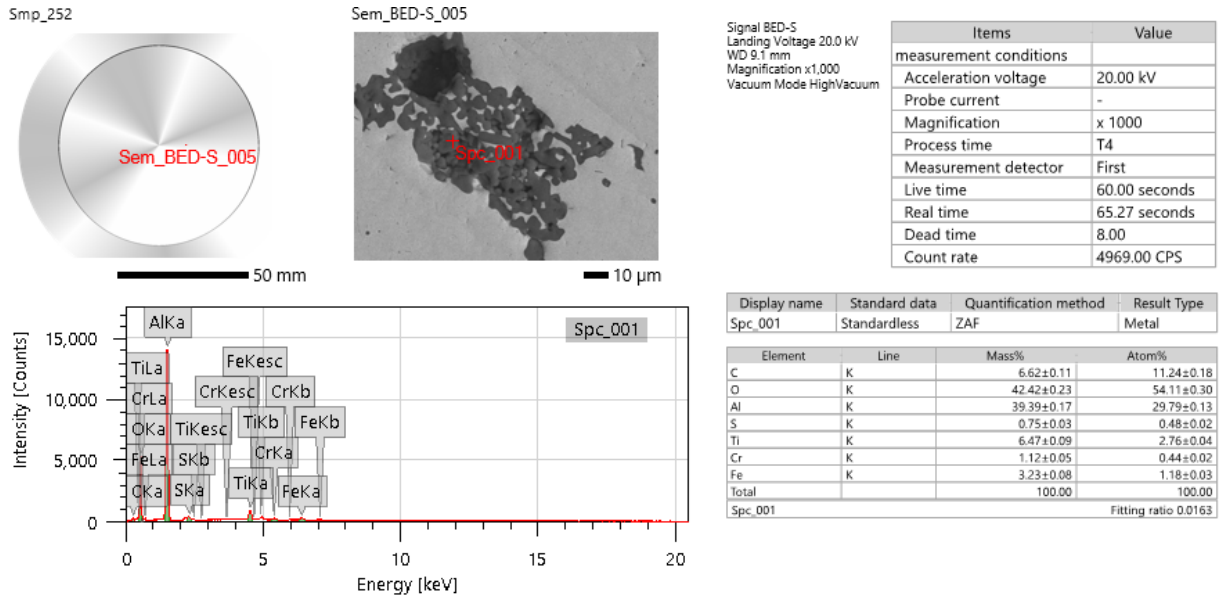
Figure 99 - As-cast L5.1 alloy SEM-BSE: Chemical composition of one of the white points (1000x magnification).



Source: own authorship (2022).

The chemical composition (in atomic %) in an aluminum oxide point is presented in [Fig. 100](#): carbon (11.24 ± 0.18), oxygen (54.11 ± 0.30), aluminum (29.79 ± 0.13), sulphur (0.48 ± 0.02), titanium (2.76 ± 0.04), chrome (0.44 ± 0.02), iron (1.18 ± 0.03).

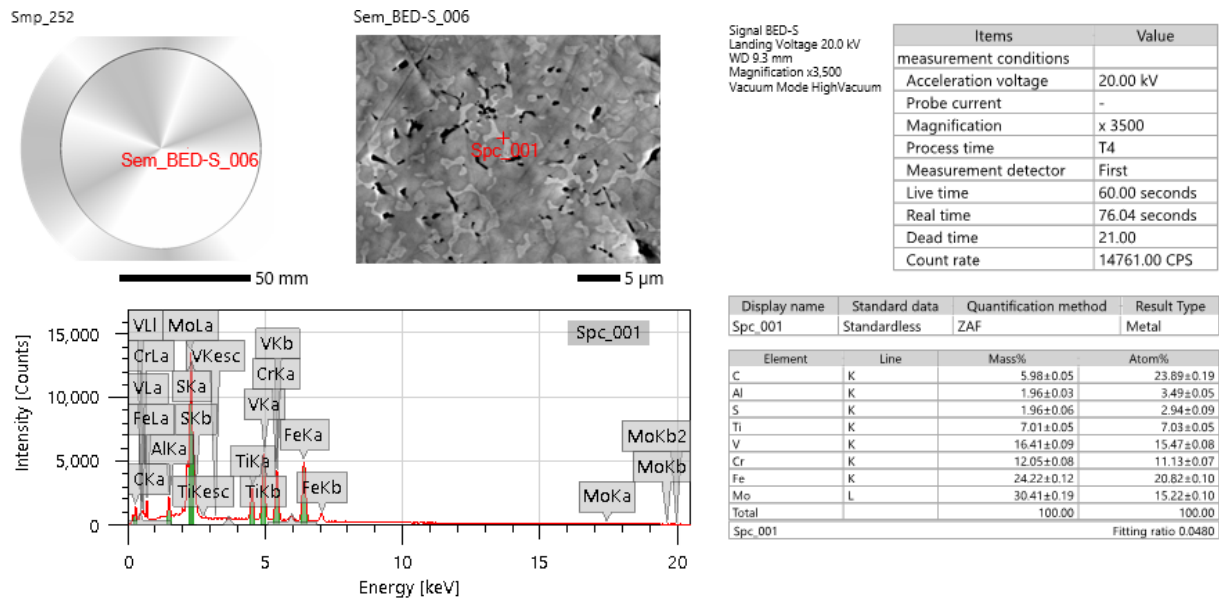
Figure 100 - As-cast L5.1 alloy SEM-BSE: Chemical composition of an aluminum oxide points.



Source: own authorship (2022).

Another white point of the L5.1 alloy presents the following chemical composition (in atomic %), as per [Fig. 101](#): carbon (23.89 ± 0.19), aluminum (3.49 ± 0.05), sulphur (2.94 ± 0.09), titanium (7.03 ± 0.05), vanadium (15.07 ± 0.08), chrome (11.13 ± 0.07), iron (20.82 ± 0.10), and molybdenum (15.22 ± 0.10).

Figure 101 - As-cast L5.1 alloy SEM-BSE: Chemical composition of one of the white points (3500x magnification).

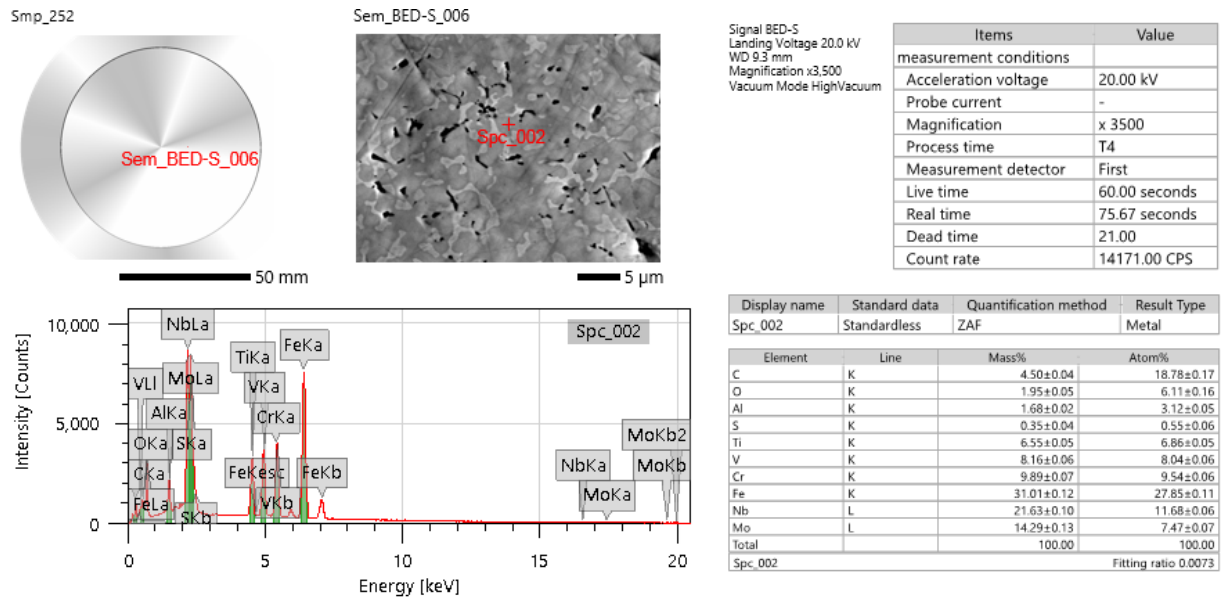


Source: own authorship (2022).

One of the gray points of the L5.1 alloy presents the following chemical composition (in atomic %), as per [Fig. 102](#): carbon (18.78 ± 0.17), oxygen (6.11 ± 0.16), aluminum (3.12 ± 0.05), sulphur (0.55 ± 0.06), titanium (6.86 ± 0.05), vanadium (8.04 ± 0.06), chrome (9.54 ± 0.06), iron (27.85 ± 0.11), niobium (11.68 ± 0.06), and molybdenum (7.47 ± 0.07).

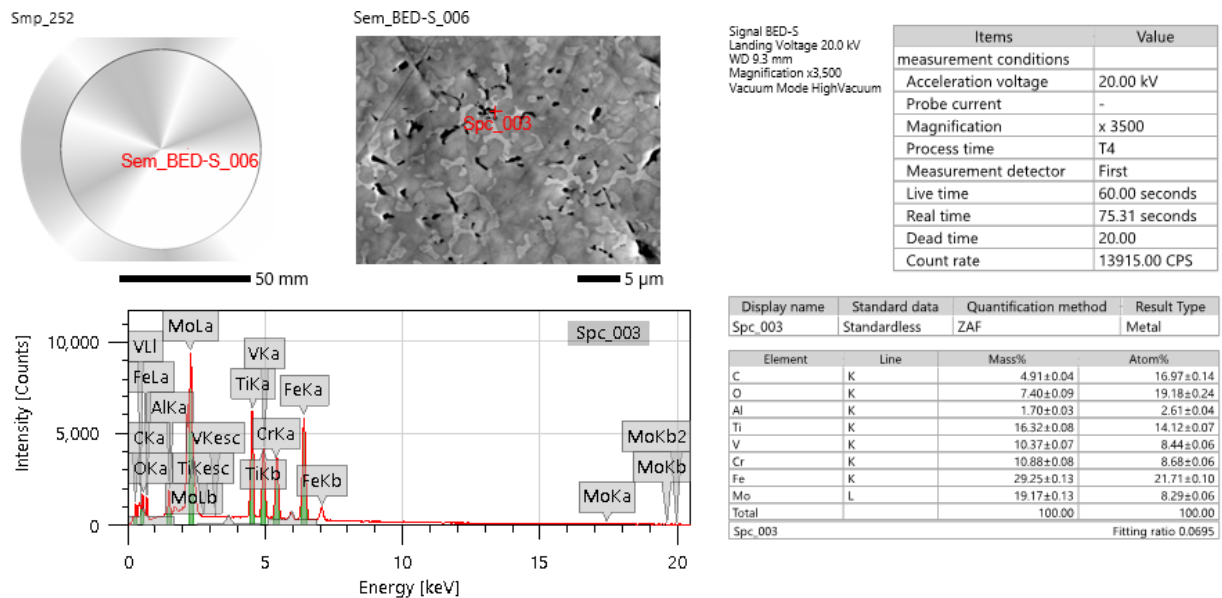
In the sequence, the black regions of the L5.1 alloy are composed by the following chemical elements (in atomic %), as per [Fig. 103](#): carbon (16.97 ± 0.14), oxygen (19.18 ± 0.24), aluminum (2.61 ± 0.04), titanium (14.12 ± 0.07), vanadium (8.44 ± 0.06), chrome (8.68 ± 0.06), iron (21.71 ± 0.10), and molybdenum (8.29 ± 0.06).

Figure 102 - As-cast L5.1 alloy SEM-BSE: Chemical composition of one of the gray points.



Source: own authorship (2022).

Figure 103 - As-cast L5.1 alloy SEM-BSE: Chemical composition of one of the black points.



Source: own authorship (2022).

The compositions of white, gray, and black regions before and after the carbon and oxygen normalization for L5.1 alloy are shown in [Tab. 23](#).

Table 23 - Composition before and after carbon and oxygen normalization for L5.1 alloy.

Element	Before C and O normalization				After C and O normalization		
	Theoretical atomic %	Experimental white region atomic %	Experimental gray region atomic %	Experimental black region atomic %	Experimental white region atomic %	Experimental gray region atomic %	Experimental black region atomic %
Al	11.11	3.49	3.12	2.61	4.37	4.15	4.08
C	0.00	16.24	18.78	16.97	0.00	0.00	0.00
Cr	11.11	9.27	9.54	8.68	11.62	12.71	13.59
Fe	33.34	29.07	27.85	21.71	36.44	37.08	34.01
Mo	11.11	8.60	7.47	8.29	10.78	9.95	12.98
Nb	11.11	9.10	11.68	0.00	11.40	15.55	0.00
N	0.00	0.00	0.00	0.00	0.00	0.00	0.00
O	0.00	5.98	6.11	19.18	0.00	0.00	0.00
S	0.00	0.00	0.00	0.00	0.00	0.00	0.00
Ti	11.11	8.74	6.86	14.12	10.95	9.14	22.12

Source: own authorship (2023).

[Tab. 24](#) compares theoretical and experimental values of atomic percentage composition for L5.1 alloy before carbon and oxygen normalization.

Table 24 - Comparison between theoretical and experimental chemical composition for L5.1 alloy before carbon and oxygen normalization in the three distinct regions.

Element	Theoretical atomic %	Experimental white region atomic %	Absolute value of relative error %	Experimental gray region atomic %	Absolute value of relative error %	Experimental black region atomic %	Absolute value of relative error %
Al	11.11	3.49	68.59	3.12	71.92	2.61	2.11
C	0.00	16.24	NA	18.78	NA	16.97	NA
Cr	11.11	9.27	16.56	9.54	14.13	8.68	7.03
Fe	33.34	29.07	12.81	27.85	16.47	21.71	34.88
Mo	11.11	8.60	22.59	7.47	32.76	8.29	25.38
Nb	11.11	9.10	18.09	11.68	5.13	0.00	NA
N	0.00	0.00	0.00	0.00	0.00	0.00	0.00
O	0.00	5.98	NA	6.11	NA	19.18	NA
S	0.00	0.00	0.00	0.00	0.00	0.00	0.00
Ti	11.11	8.74	21.33	6.86	38.25	14.12	27.09

Source: own authorship (2023).

[Tab. 25](#) provides the comparison between theoretical and experimental values of atomic percentage composition for L5.1 alloy after carbon and oxygen normalization.

Table 25 - Comparison between theoretical and experimental chemical composition for L5.1 alloy after carbon and oxygen normalization in the three distinct regions.

Element	Theoretical atomic %	Experimental white region atomic %	Absolute value of relative error %	Experimental gray region atomic %	Absolute value of relative error %	Experimental black region atomic %	Absolute value of relative error %
Al	11.11	4.37	60.67	4.15	62.64	4.08	63.28
C	0.00	0.00	0.00	0.00	0.00	0.00	0.00
Cr	11.11	11.62	4.59	12.71	14.40	13.59	22.32
Fe	33.34	36.44	9.30	37.08	11.22	34.01	0.99
Mo	11.11	10.78	2.97	9.95	10.44	12.98	16.83
Nb	11.11	11.40	2.61	15.55	39.96	0.00	NA
N	0.00	0.00	0.00	0.00	0.00	0.00	0.00
O	0.00	0.00	0.00	0.00	0.00	0.00	0.00
S	0.00	0.00	0.00	0.00	0.00	0.00	0.00
Ti	11.11	10.95	1.44	9.14	17.73	22.12	99.10

Source: own authorship (2023).

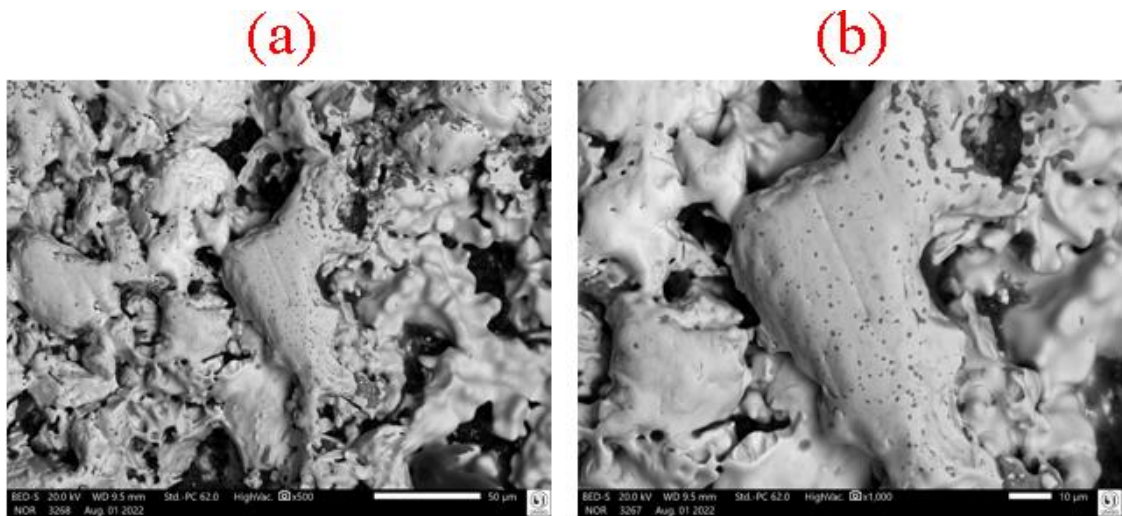
Theoretical and experimental compositions present high discrepancies in absolute relative values, which can be due to the fact that the sample points are not representative of the entire L5.1 alloy. Some reasons relies on the following items: (a) the sample area is approximately a circle with radius 7 mm, and the sample size is 70 x 80 μm in 3500x; (b) in what refers to probability, there is a chance to collect points which compositions do not match; (c) as a point is truly a small area, then this area may also present properties from adjacent areas. It is important to note that, after carbon and oxygen normalization, the absolute values of the relative errors decreased.

7.5.4 Sintered L4, L5, and L5.1 alloys SEM-BSE results

In what refers to sintered alloys, SEM-BSE results for L4 alloy (500x, and 1000x magnifications) are shown in [Fig. 104a](#), [Fig. 104b](#). Sintered L5 alloy (500x, and 1000x), and sintered L5.1 alloy (500x, and 1000x) are represented, respectively, in [Fig. 105a](#), [Fig. 105b](#), [Fig. 106a](#), and [Fig. 106b](#).

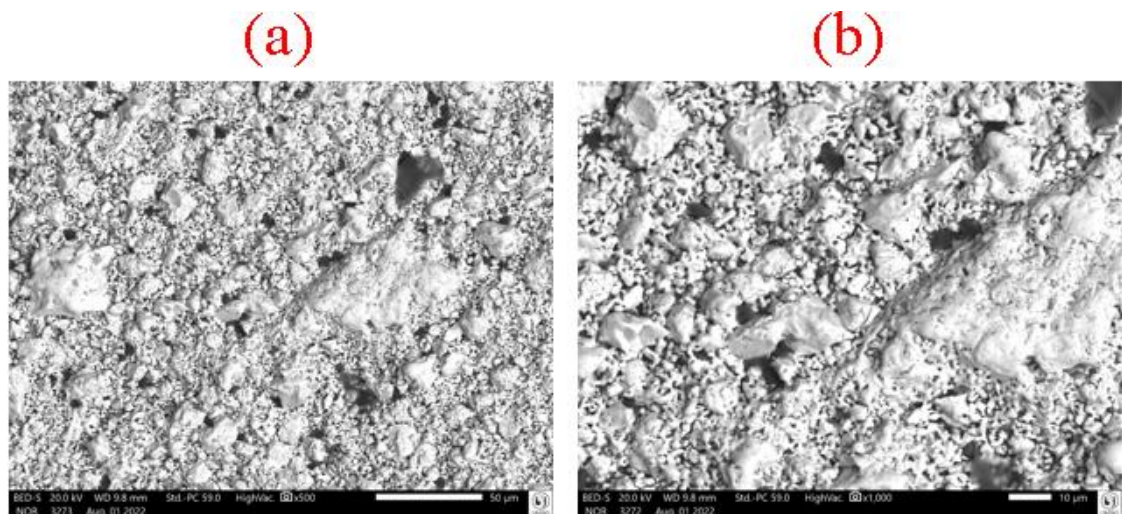
A typical sintered microstructure can be observed in [Fig. 104a](#) and in its amplification ([Fig. 104b](#)), presenting superficial irregularities, which addresses some porosity. This characteristic corroborates with the dilatometric results for L4 alloy ([Subsection 7.4.2](#)) and with densification data ([Subsection 7.4.1](#)). One of its phases acts like a barrier to sintering, preventing an effective densification.

Figure 104 - Sintered L4 alloy SEM-BSE: (a) 500x magnification (trace scale 50 μm); (b) 1000x magnification (trace scale 10 μm).



Source: own authorship (2023).

Figure 105 - Sintered L5 alloy SEM-BSE: (a) 500x magnification (trace scale 50 μm); (b) 1000x (trace scale 10 μm).

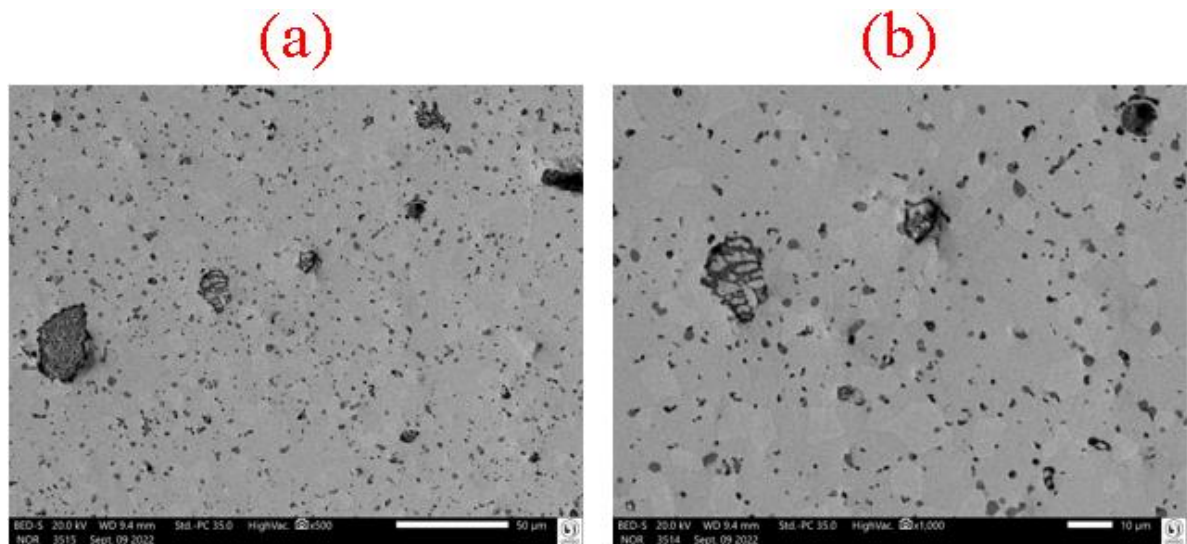


Source: own authorship (2023).

In terms of sintering, an intermediate result between sintered L4, and sintered L5.1 is presented by sintered L5 alloy (less porosity, thus more densification). [Fig. 106a](#), and [Fig. 106b](#) confirm what is described in performed dilatometry ([Subsection 7.4.2](#)) and with densification values ([Subsection 7.4.1](#)).

Sintered L5.1 microstructure addresses the most densified alloy, in which the microstructure is very similar to the one found in the as-cast state. As per [Subsection 7.4.1](#), the densification reached up to 98%.

Figure 106 - Sintered L5.1 alloy SEM-BSE: (a) 500x magnification (trace scale 50 μm); (b) 1000x (trace scale 10 μm).



Source: own authorship (2023).

7.6 Intellectual Production Within This Thesis

This thesis was developed throughout the doctorate time, producing the following technological products:

- (a) Expanded abstracts in congresses: 2 ([NONATO et al., 2022](#)), ([NONATO; RESTIVO, 2022b](#)).
- (b) Softwares: 4 ([NONATO; RESTIVO, 2023](#)), ([NONATO; RESTIVO, 2022a](#)), ([NONATO; RESTIVO, 2022b](#)), ([NONATO; RESTIVO, 2022c](#)),

([NONATO; RESTIVO, 2021](#)), ([NONATO; RESTIVO, 2021a](#)), ([NONATO; RESTIVO, 2023a](#)), ([NONATO; RESTIVO, 2022d](#)).

(c) Congress papers: 4 ([NONATO; RESTIVO, 2022](#)), ([NONATO; RESTIVO, 2021](#)), ([NONATO; RESTIVO, 2021a](#)), ([NONATO; RESTIVO, 2021b](#))

(d) Book chapters: 4 ([NONATO; RESTIVO, 2023](#)), ([NONATO; RESTIVO, 2022](#)), ([NONATO; RESTIVO, 2023a](#)), ([NONATO; RESTIVO, 2022d](#)).

(e) Papers accepted for publication in future issues of periodicals: 1 ([RESTIVO *et al.*, 2023](#)).

(f) Papers sent to periodicals, waiting for decision to publish or not: 1.

8 CONCLUSIONS

This section presents the main conclusions and final considerations extracted after the research, computational tools and experiments were made. In addition, suggestions for future works are addressed here.

8.1 Main Conclusions, Contributions, and Final Considerations

In this work, the design, powder metallurgy, and sintering of Extremely Hard Multicomponent Metal Alloys (EHMMAs) were addressed due to their importance within the wear resistance (life span) concept. In the design branch, the multiparametric and multicriteria approach was formulated and applied in the design of these types of alloys. The theory of powder compaction to mathematically assure that all the particles were plasticized was applied in the compaction of the powders of the alloys reported in this work. The fundamentals of sintering analysis were studied to quantify sintering parameters and substantiate the decision-making process. Consequently, three softwares were created: (a) PComp, for powder compaction; (b) DIAMOY 1.0 (superseded by DIAMOY 2.0, an improvement of 1.0); and (c) SINT, software that involves sintering parameters. In addition, many experiments were conducted, such as melting metal alloy powders, compaction of metal alloy powder, powder blending, ball-milling comminution, sintering, hammering, weighing, hardness testing, scanning electron microscopy (SEM), among others.

Among the accomplished objectives, it is worthwhile to mention: (a) samples of these alloys were produced to be subjected to mechanical characterization; (b) Aluminum was used in place of tantalum in L4.1, L5.1, and L5.1Cu, L7, and FN22 alloys, which turned these alloys cheaper than those with tantalum (L4, L4Cu, L5, and L5Cu); (c) hardness tests were performed on some of the alloys. (d) composition, heat treatment, and processing of the alloys were also specified; (e) alloy elements were melted together aiming at reaching the most homogeneous ingot; (f) powder was extracted from the cast alloy ingots; (g) compaction and sintering processes of the alloy powders were studied to obtain the less bulky product as possible; (h) computational tools to compaction and design processes were developed to avoid unnecessary experiments and ease the involved processes; (i) the design framework to EHMMAs was created.

The main contributions of this research to the design of EHMMAs refer to:

- (a) gathering of parameters and criteria not yet used for the design of EHMMAs in a single computational tool, facilitating the evaluation of the design process;
- (b) establishing an EHMMMA project framework;
- (c) creation of computational tools for powder compaction, EHMMMA design and sintering for the Windows® platform;
- (d) creation of metallic alloys not yet reported;
- (e) carrying out experiments with some alloys that have a predicted potential to form stable solid solutions with high hardness;
- (f) establishing a baseline for future improvements.

8.2 Suggestion for Future Works

The following items may be studied as a complement, treated as an improvement, or even suggestions to start another research work. They are listed:

- (a) Create a software that aggregates “PComp”, “DIAMOY 2.0”, and “SINT” in a unique software solution.
- (b) Apply Design of Experiments (DOE) technique to organize and cover more possibilities of experiments.
- (c) Make a deep understanding about the two approaches not dealt herein: molecular dynamic (MD) simulations, and calculation phase diagrams (CALPHAD) in order to comprise a greater scope and compare the results with the multiparametric and multicriteria approach.

REFERENCES

- AKMCIOGLU, S.; GOKKAYA, H.; UYGUR, I. The effects of cryogenic-treated carbide tools on tool wear and surface roughness of turning of Hastelloy C22 based on Taguchi method. **International Journal of Advanced Manufacturing Technologies**, v.82, p.303-314, 2016, <http://dx.doi.org/10.1007/s00170-015-7356-z>.
- ANTONY, L. V. M.; REDDY, R. G. Processes for production of high-purity metal powders. **JOM**, p.14–18, 2003.
- ASHBY, M.; SHERCLIFF, H.; CEBON, D. **Materials: engineering, science, processing and design**. Oxford: Butterworth-Heinemann, 2019.
- BALDENEBO-LOPEZ, F. J.; HERRERA-RAMÍREZ, J. M.; ARREDONDO-REA, S. P.; GÓMEZ-ESPARZA, C. D.; MATÍNEZ-SÁNCHEZ, R. Simultaneous effect of mechanical alloying and arc-melting processes in the microstructure and hardness of an AlCoFeMoNiTi high-entropy alloy. **Journal of Alloys and Compounds**, v. 643, p. S250-S255, 2015, <http://dx.doi.org/10.1016/j.jallcom.2014.12.059>.
- BATT, G. M. **Investigation of the spectral properties of disordered alloys and superconductors**. 2008. PhD thesis. University of Bristol, Bristol, England, 2008. Available in: <http://www.bris.ac.uk/physics/media/theory-theses/batt-g-thesis.pdf>. Access in Jan 26th. 2022.
- BOCKSTIEGEL, G. **The porosity-pressure curve and its relation to the size distribution of pores in iron powder compacts**, *In*: International Powder Metallurgy Conference, I, 1965, New York, USA.
- BURAVLEV, I. Y.; SHICHALIN, O. O.; PAPYNOV, E. K.; GOLUB, A. V.; GRIDASOVA, E. A.; BURAVLEVA, A. A.; YAGOFAROV, V. Y.; DVORNIK, M. I.; FEDORETS, A. N.; REVA, V. P.; YUDAKOV, A. A.; SERGIENKO, V. I. WC-5TiC-10Co hard metal alloy fabrication via mechanochemical and SPS techniques. **International Journal of Refractory Metals & Hard Materials**, v. 94 105385, p. 1-11, 2021, <http://dx.doi.org/10.1016/j.ijrm.hm.2020.105385>.
- CALLEN, H. B. **Thermodynamics and an introduction to thermostatics**. 2nd. ed. New York: John Wiley and Sons, 1985.
- CHIAVERINI, V. **Metalurgia do pó, técnica e produtos**. 3rd. ed., São Paulo: Associação Brasileira de Metais, 1992.
- COORDENAÇÃO DE APERFEIÇOAMENTO DE PESSOAL DE NÍVEL SUPERIOR. CAPES. **Busca por assunto**. 2022. Available in: <<https://www-periodicos-capes-gov-br.ezl.periodicos.capes.gov.br/index.php?>>>. Access in: May 26th, 2022.

DANIEL, J.; SOUCEK, P.; BERNÁTOVÁ, K.; ZÁBRANSKÝ, L.; STUPAVSKÁ, M.; BURSÍKOVÁ, V.; VASINA, P. Investigation of the influence of Ni doping on the structure and hardness of Ti-Ni-C coatings. **Journal of Nanomaterials**, v.2017, p.1-13, 2017, <https://doi.org/10.1155/2017/6368927>.

DEAN, J. A. **Lange's handbook of chemistry**. 15th. ed., New York: McGraw-Hill, 1999.

DENNIS, D. H. **Properties and selection: irons, steels, and high-performance alloys** in ASM Handbook. Vol.1. Ohio: ASM International, 1993.

DOVALE-FARELO, V.; TAVADZE, P.; VERSTRAETE, M. J.; BAUTISTA-HERNÁNDEZ, A.; ROMERO, A. H. Exploring the elastic and electronic properties of chromium molybdenum diboride alloys. **Journal of Alloys and Compounds**, v. 866 158885, p. 1-11, 2021, <http://dx.doi.org/10.1016/j.jallcom.2021.158885>.

FANG, S.; XIAO, X.; XIA, L.; LI, W.; DONG, Y. Relationship between the widths of supercooled liquid regions and bond parameters of Mg-based bulk metallic glasses. **Journal of Non-crystalline Solids**, v.321, p.120-125. 2013. DOI: [https://doi.org/10.1016/S0022-3093\(03\)00155-8](https://doi.org/10.1016/S0022-3093(03)00155-8).

FANG, Z. Z. **Sintering of advanced materials: fundamentals and processes**. Cambridge: Woodhead Publishing, 2010.

FRITZE, S.; MALINOVSKIS, P.; RIEKEHR, L.; VON FIEANDT, L.; LEWIN, E.; JANSSON, U. Hard and crack resistant carbon supersaturated refractory nanostructured multicomponent coatings. **Scientific Reports**, v.8:14508, p.1-8, 2018, <https://doi.org/10.1038/s41598-018-32932-y>.

GAO, M. C.; ALMAN, D. E. Searching for next single-phase high-entropy alloy compositions. **Entropy**, v.15, p.4504-4519, 2013, <http://dx.doi.org/10.3390/e15104504>.

GILMAN, J. J. **Chemistry and physics of mechanical hardness**. 1st ed. New Jersey: John Wiley & Sons, 2009.

GUO, S.; NG, C.; LU, J.; LIU, C. T. Effect of valence electron concentration on stability of fcc or bcc phase in high entropy alloys. **J. Appl. Phys.**, v.109:103505, p.1-5, 2011.

GUTIERREZ-NODA, L.; CAO-MOREU, C. A.; PEREZ-ACOSTA, O.; LORENZO-BONET, P.; ZAMBRANO-ROBLEDÓ, P.; HERNANDES-RODRIGUEZ, M. A. L. The effect of a boride diffusion layer on the tribological properties of AISI M2 steel. **Wear**, v.426-427, p.1667-1671, 2019, <http://dx.doi.org/10.1016/j.wear.2019.01.089>.

HERRMANN, K. **Hardness testing: principles and applications**. 1st ed. Ohio: ASM International, 2011.

HÖGANÄS. **Handbook for sintered components**. Vol.1-3, Stocolm: Höganäs, 2013.

HOUDKOVÁ, S.; CESÁNEK, Z.; SMAZALOVÁ, E.; LUKÁČ, F. The high-temperature wear and oxidation behavior of CrC-based HVOF coatings. **Journal of Thermal Spray Technologies**, v.27, p.179-195, 2018, <https://doi.org/10.1007/s11666-017-0637-3>.

HUANG, S.; VITOS, L. High entropy alloys: elastic parameters and trends. **Encyclopedia of Materials: Metals and Alloys**, v.2, p.427-434. 2022. DOI: <https://doi.org/10.1016/b978-0-12-803581-8.11714-x>.

INAMUDDIN, R. B.; BODDULA, R.; AHAMED, M. I.; ASIRI, A. M. **Alloy materials and their allied applications**. Hoboken: John Wiley and Sons, 2020.

JAFFEE, R. I.; WILCOX, B. A. **Fundamental aspects of structural alloy design**. New York: Plenum Press, 1975.

KAZANTSEVA, N. V.; STEPANOVA, N. N.; RIGMANT, M. B. **Superalloys: analysis and control of failure process**. 1st ed. Boca Raton: CRC Press, 2019.

KLAUS, M. Z. **Properties and selection: nonferrous alloys and special-purpose materials** in ASM Handbook. Vol. 2, Ohio: ASM International, 1993.

KRASNOWSKI, M.; GIERLOTKA, S.; KULIK, T. Nanocrystalline Al₃Ni₂ alloy with high hardness produced by mechanical alloying and high-pressure hot-pressing consolidation. **Intermetallics**, v.42, p.35-40, 2013, <http://dx.doi.org/10.1016/j.intermet.2013.05.017>.

LI, A.; ZHANG, X. Thermodynamic analysis of the simple microstructure of AlCrFeNiCu high-entropy alloy with multi-principal elements, **Acta Metallurgica Sinica (English Letters)**, v.22, p.219-224, 2009, [http://dx.doi.org/10.1016/S1006-7191\(08\)60092-7](http://dx.doi.org/10.1016/S1006-7191(08)60092-7).

LI, C.; LI, J. C.; ZHAO, M.; JIANG, Q. Effect of alloying elements on microstructure and properties of multi-principal elements high-entropy alloys, **Journal of Alloys and Compounds**, v. 475, p.752-757, 2009, <http://dx.doi.org/10.1016/j.jallcom.2008.07.124>.

LIANG, Y. X.; WU, Z. M.; FU, E. G.; DU, J. L.; WANG, P. P.; ZHAO, Y. B.; QIU, Y. H.; HU, Z. Y. Refinement process and mechanisms of tungsten powder by high energy ball milling. **International Journal of Refractory Metals & Hard Materials**, v.67, p.1-8, 2017, <https://doi.org/10.1016/j.ijrmhm.2017.04.006>.

LONG, W. M. Radial pressure in powder compaction. **Powder Metal**, v. 6, p. 73–86, 1960.

LV, S.; ZU, Y.; CHEN, G.; ZHAO, B.; FU, X.; ZHOU, W. A multiple nonmetallic atoms co-doped CrMoNbWTi refractory high-entropy alloy with ultra-high strength and hardness. **Materials Science & Engineering A**, v.795, 140035, 2020, <https://doi.org/10.1016/j.msea.2020.140035>.

LYU, S.; LI, G.; HU, T.; ZHENG, R.; XIAO, W.; MA, C. A new cast Mg-Y-Sm-Zn-Zr alloy with high hardness. **Materials Letters**, v.217, p.79-82, 2018, <https://doi.org/10.1016/j.matlet.2018.01.041>.

NONATO, R. B. P.; FIGUEIRA, R.; FERREIRA, O. A.; PADOVANI, C.; BELCHIOR, A.; ARANHA, N.; RESTIVO, T. A. G. **Development of ultra-hard metal alloys**. In: Congresso Brasileiro de Aplicações de Vácuo na Indústria e na Ciência, XLIII, 2022, Sorocaba, Brazil.

NONATO, R. B. P.; RESTIVO, T. A. G. **A multiparametric and multicriteria software to evaluate the design of ultra-hard metal alloys**. In: RAMOS, J. (org.). **Open Science Research**. Guarujá: Editora Científica Digital, 2023, 1st ed., p. 1464-1483. Available in: <<https://downloads.editoracientifica.com.br/articles/230111860.pdf>>. Access in: 02/04/2023.

NONATO, R. B. P.; RESTIVO, T. A. G. **Desenvolvimento de programa de computador para compactação de pós de ligas metálicas**. In: Congresso Nacional Multidisciplinar em Ciência, I, 2022a, Brasília, Brazil.

NONATO, R. B. P.; RESTIVO, T. A. G. **Development of a software to design ultra-hard metal alloys**. In: Congresso Brasileiro de Aplicações de Vácuo na Indústria e na Ciência, XLIII, 2022b, Sorocaba, Brazil.

NONATO, R. B. P.; RESTIVO, T. A. G. Software creation for ultra-hard metal alloy design. In: ULHÔA, J. L. R.; SARAIVA-BONATTO, E. C.; BARBOSA, F. C.; GONTIJO, C. E. O.; PIRES, P. F. (org.). **Engenharia: A Máquina Que Constrói O Futuro ?** Piracanjuba: Editora Conhecimento Livre, 2022c, v. 9, p. 168-181. Available in: <<https://api.conhecimentolivre.org/ecl-api/storage/app/public/L.514-2022.pdf>>. Access in: 25/10/2022.

NONATO, R. B. P.; RESTIVO, T. A. G. **Software development for ultra-hard metallic alloy design**. In: Encontro Nacional de Modelagem Computacional and XII Encontro Nacional de Ciência dos Materiais, XXIV, 2021, Ilhéus, Brazil.

NONATO, R. B. P.; RESTIVO, T. A. G. **Software for compaction of powder metal alloys**. In: Encontro Nacional de Modelagem Computacional and XII Encontro Nacional de Ciência dos Materiais, XXIV, 2021, Ilhéus, Brazil.

NONATO, R. B. P.; RESTIVO, T. A. G. Software for densification calculation in sintering of flat cylinders. In: RAMOS, J. (org.). **Open Science Research**. Guarujá: Editora Científica Digital, 2023a, 1st ed., p. 1484-1496. Available in: <<https://downloads.editoracientifica.com.br/articles/230111718.pdf>>. Access in: 02/04/2023.

NONATO, R. B. P.; RESTIVO, T. A. G. Software solution for ultra-hard metal alloy design. In: GUIMARÃES, O. S. (org.). **Engenharia, gestão e inovação**. Belo Horizonte: Editora Poisson, 2022d, 1ed., v. 3, p. 179-187. Available in: <https://www.poisson.com.br/livros/engenharia/gestao_inovacao/volume3/>. Access in: 25/10/2022.

NONATO, R. B. P.; RESTIVO, T. A. G. **Uncertainty quantification in powder compaction of metal alloys**. In: *Encontro Internacional de Pós-graduação*, I, 2021b, Santos, Brazil.

PETRÍK, J.; PALFY, P. The influence of the load on the hardness. **Metrology and Measuring Systems**, n.2, p. 223-234, 2011.

PFEILER, W. **Alloy physics**. Weinheim: Wiley-VCH, 2007.

PRAKASH, M.; KUMAR, N. M.; PREMALATHA, B.; RAMEEZA, M. Experimental investigation and comparison of coated, uncoated and cryogenically treated HSS cutting tool. **Advances in Natural and Applied Sciences**, v.10, n.9, p. 267-276, 2016.

RAZUAN, R.; JANI, N. A.; HARUN, M. K.; TALARI, M. K. Microstructure and hardness properties investigation of Ti and Nb added FeNiAlCuCrTi_xNb_y high entropy alloys. **Transactions of the Indian Institute of Metals**, v.66, n.4, p.309-312, 2013, <https://doi.org/10.1007/s12666-013-0265-7>.

REN, B.; LIU, Z. X.; SHI, L.; CAI, B.; WANG, M. X. Structure and properties of (AlCrMnMoNiZrB_{0.1})_{Nx} coatings prepared by reactive DC sputtering. **Applied Surface Science**, v.257, p.7172-7178, 2011, <http://dx.doi.org/10.1016/j.apsusc.2011.03.083>.

RESTIVO, T. A. G.; CASTANHO, S. R. H. M.; TENORIO, J. A. S. TG/DTA-MS evaluation of methane cracking and coking on doped nickel-zirconia based cermets. **Journal of Thermal Analysis and Calorimetry**, v. 118, p. 75-81, 2014. <http://dx.doi.org/10.1007/s10973-014-4003-0>.

RESTIVO, T. A. G.; CASTANHO, S. R. H. M. Cu-Ni-YSZ anodes for solid oxide fuel cell by mechanical alloying processing. **International Journal of Materials Research**, v. 101, p. 128-132, 2010. <https://doi.org/10.3139/146.110248>.

RESTIVO, T. A. G.; NONATO, R. B. P.; FIGUEIRA, R. R.; FERREIRA, O. A.; PADOVANI, C.; ARANHA, N.; BALDO, D.; SILVA, C. G.; DURAZZO, M. Sintering of metallic diamond alloy powders. **Journal of Thermal Analysis and Calorimetry**, 2023. <https://doi.org/10.1007/s10973-023-12260-8>.

RESTIVO, T. A. G.; RESTIVO, G. M. G. Development of ultra-hard multicomponent alloys. **Journal of Materials Research**, p.1-12, 2021. <http://dx.doi.org/10.1557/s43578-021-00195-5>.

RIEDEL, R. **Handbook of ceramic hard materials**. 1st ed. Weinheim: Wiley-VCH, 2000.

RYU, S. H.; YU, J. A new equation for the Cr equivalent in 9 to 12 pct Cr steels. **Metallurgical and Materials Transactions A**, v.29A, p.1573-1578. 1998. DOI: <http://dx.doi.org/10.1007/s11661-998-0080-7>.

SADD, M. H. **Elasticity, theory, applications, and numerics**. 4th ed. London: Elsevier, 2020.

SAKETI, S.; SVEEN, S.; GUNNARSSON, S.; M'SAOUBI, R., OLSSON, M. Wear of a high cBN content PCBN cutting tool during hard milling of powder metallurgy cold work tool steels. **Wear**, v.332-333, p.752-761, 2015, <http://dx.doi.org/10.1016/j.wear.2015.01.073>.

SARAVANAN, R.; RANI, M. P. **Metal and alloy bonding: an experimental analysis**. London: Springer, 2012.

SINGH, K. A.; KUMAR, N.; DWIVEDI, A.; SUBRAMANIAM, A. A geometrical parameter for the formation of disordered solid solutions in multi-component alloys. **Intermetallics**, v.53, p.112-119, 2014, <http://dx.doi.org/10.1016/j.intermet.2014.04.019>.

SHALABY, M. A.; EL HAKIM, M. A.; ABDELHAMEED, M. M.; KRZANOWSKI, J. E.; VELDHUIS, S. C.; DOSBAEVA, G. K. Wear mechanisms of several cutting tool materials in hard turning of high carbon-chromium tool steel. **Tribology International**, v.70, p.148-154, 2014, <http://dx.doi.org/10.1016/j.triboint.2013.10.011>.

SHUN, T.-T.; CHANG, L.-Y.; SHIU, M.-H. Microstructures and mechanical properties of multiprincipal component CoCrFeNiTi_x alloys. **Materials Science & Engineering A**, v.556, p.170-174, 2012, <http://dx.doi.org/10.1016/j.msea.2012.06.075>.

SONG, R.; WEI, L.; YANG, C.; WU, S. Phase transformation and strengthening mechanisms in a dual-phase nanocrystalline CRMnFeVTi high-entropy alloy with ultrahigh hardness. **Journal of Alloys and Compounds**, v.744, p.552-560, 2018, <https://doi.org/10.1016/j.jallcom.2018.02.029>.

TABOR, D. **The hardness of metals**. Oxford: Clarendon Press, 1951.

TAKEUCHI, A.; INOUE, A. Calculations of amorphous-forming composition range for ternary alloy systems and analyses of stabilization of amorphous phase and amorphous-forming ability. **Materials Transactions**, v.7, p.1435-1444, 2001.

TAKEUCHI, A.; INOUE, A. Mixing enthalpy of liquid phase calculated by miedema's scheme and approximated with sub-regular solution model for assessing forming ability of amorphous and glassy alloys. **Intermetallics**, v.18, p.1779-1789, 2010.

TAZUDDIN, A.; BISWAS, K.; GURAO, N.P. Deciphering micro-mechanisms of plastic deformation in a novel single phase fcc-based MnFeCoNiCu high entropy alloy using crystallographic texture. **Materials Science & Engineering A**, v.657, p.224-233, 2016. <http://dx.doi.org/10.1016/j.msea.2016.01.065>.

TAZUDDIN, A.; GURAO, N.P.; BISWAS, K. In the quest of single-phase multi-component multiprincipal high entropy alloys. **Journal of Alloys and Compounds**, v.697, p.434-442, 2017.

THÜMMLER, F.; OBERACKER, R. **An introduction to powder metallurgy**. London: The institute of materials, 1993.

UL-HAMID, A. **A beginner's guide to scanning electron microscopy**. Cham: Springer, 2018.

VIRTUAL LABS. "Vickers Hardness Test", 2022. Available in: <<https://sm-nitk.vlabs.ac.in/exp/vickers-hardness-test/procedure.html>>. Access in: Sep 19th, 2022.

WANG, X.-R.; WANG, Z.-Q.; HE, P.; LIN, T.-S.; SHI, Y. Microstructure and wear properties of CuNiSiTiZr high-entropy alloy coatings on TC11 titanium alloy produced by electrospark – computer numerical control deposition process. **Surface & Coatings Technology**, v.283, p.156-161, 2015, <http://dx.doi.org/10.1016/j.surfcoat.2015.10.013>.

WANG, Z.; HUANG, Y.; LIU, C.T.; LI, J.; WANG, J. Atomic packing and size effect on the Hume-Rothery rule. **Intermetallics**, v.109, p.139-144. 2019. DOI: <http://dx.doi.org/10.1016/j.intermet.2019.04.001>.

WOLFENDEN, A.; WEILER, W. W. Dynamic loading a new microhardness test method. **Journal of Testing and Evaluation**, v.18, p.229-239. 1990.

WU, Y.; WANG, H.; CHENG, Y.; LIU, X.; HUI, X.; NIEH, T.; WANG, Y.; LU, Z. Inherent structure length in metallic glasses: simplicity behind complexity. **Scientific Reports**, v. 5:12137, p. 1-10. 2015. DOI: <http://dx.doi.org/10.1038/srep12137>.

XIE, L.; BRAULT, P.; THOMANN, A.-L.; BAUCHIRE, J.-M. AlCoCrCuFeNi high-entropy alloy cluster growth and annealing on silicon: A classical molecular dynamics simulation study. **Applied Surface Science**, v.285P, p.810-816, 2013, <https://doi.org/10.1016/j.apsusc.2013.08.133>.

YANG, X.; ZHANG, Y. Prediction of high-entropy stabilized solid-solution in multi-component alloys. **Mater Chem. Phys.**, v.132, p.233–238, 2012.

YOUSSEF, K. M.; WANG, Y. B.; LIAO, X. Z.; MATHAUDHU, S. N.; KECSKÉS, L. J.; ZHU, Y. T.; KOCH, C. C. High hardness in a nanocrystalline Mg₉₇Y₂Zn₁ alloy. **Materials Science and Engineering A**, v.528, p.7494-7499, 2011, <http://dx.doi.org/10.1016/j.msea.2011.06.017>.

ZHANG, C.; ZHANG, F.; CHEN, S.; CAO, W. Computational thermodynamics aided high-entropy alloy design. **JOM**, v.64, n.7, p. 839-845, 2012, <http://dx.doi.org/10.1007/s11837-012-0365-6>.

ZHANG, F.; ZHANG, C.; CHEN, S. L.; ZHU, J.; CAO, W. S.; KATTNER, U. R. An understanding of high entropy alloys from phase diagram calculations. **CALPHAD: Computer Coupling of Phase Diagrams and Thermochemistry**, v.45, p.1-10, 2014, <http://dx.doi.org/10.1016/j.calphad.2013.10.00>.